Customized Arrays of Silica Nanochannels

Dissertation

zur

Erlangung der naturwissenschaftlichen Doktorwürde
(Dr. sc. nat.)

vorgelegt der

Mathematisch-naturwissenschaftlichen Fakultät

der

Universität Zürich

von

Nicola Zucchetto

aus

Italien

Promotionskommission

PD Dr. Dominik Brühwiler

Prof. Dr. Greta Patzke

Prof. Dr. David Tilley

Zürich, 2018

Customized Arrays of Silica Nanochannels

Dissertation

zur

Erlangung der naturwissenschaftlichen Doktorwürde
(Dr. sc. nat.)

vorgelegt der

Mathematisch-naturwissenschaftlichen Fakultät

der

Universität Zürich

von

Nicola Zucchetto

aus

Italien

Promotionskommission

PD Dr. Dominik Brühwiler

Prof. Dr. Greta Patzke

Prof. Dr. David Tilley

Zürich, 2018

ABSTRACT

Research on the properties of mesoporous silica particles is a fundamental step before the application in different fields can be realized. For this reason particle customization plays a key role. The aim of this thesis is the synthesis and the study of a particular type of mesoporous particles, namely arrays of silica nanochannels (ASNCs). The main characteristic of ASNCs is that the nanochannels run along the particle length and their regular disposition leads to the formation of hexagonal prismatic particles. Inspired by the results achieved for analogous microporous materials, such as zeolite L, we conducted experiments for tailoring the shape, for functionalizing selectively the surface and for improving the catalytic activity. Furthermore, experiments to graft silica particles on a polymeric substrate and pseudomorphic transformation studies are discussed.

The ASNCs growth is influenced by several parameters. Changes in the structure directing agent's counter-ion strongly affect the regular morphology of the particles. The addition of salts, in particular KCl and $CaCl_2$, prevents these modifications. Furthermore, the co-ions are responsible for pore diameter enlargement and consequently influence the particle aspect ratio. The silane/surfactant ratio is another factor that strongly influences the particle formation. The end-on growth is favored by increasing the amount of the silica source. The length of the particles, and therefore the length of the nanochannels, can be controlled by adjusting the relative rate of end-on growth.

The functionalization of ASNCs is generally achieved with post-synthetic treatments. The co-condensation process, made with functional silanes, influences the characteristic morphology. By combining these classical processes, a new method called post-condensation was developed in order to obtain functionalized ASNCs in a one-pot reaction. The delayed addition of functional silanes preserves the hexagonal prismatic shape. Sterical hindrance combined with end-on growth led to particles with the functional groups accumulated at the pore entrances. A tandem post-condensation method was developed to explore the possibility of obtaining bifunctional particles.

Due to the large surface area (up to 1000 m^2/g) mesoporous silica is often used as a support for catalysts. Co-condensation, post-grafting and post-condensation methods were used for the synthesis of silica-titania ASNCs-type particles. The porous properties and the

crystallinity of the materials were studied. The photoactivity of the particles was tested with photodegradation experiments.

Mesoporous silica particles supported on a polymeric substrate can be used in catalysis, drug delivery and sensor technology. The grafting process has to be simple and yield a monolayer. In order to achieve these results, different methods were explored using poly(methyl methacrylate) as a support for amino functionalized silica.

The pseudomorphic transformation of silica particles is a process composed of two steps, namely dissolution and re-precipitation. This method is used to modify the particle framework from macroporous to mesoporous without altering the morphology. Bimodal mesoporous materials were prepared with pseudomorphic transformation, starting from large pore mesoporous particles. The framework changes were studied with gas sorption and SAXS.

KURZFASSUNG

Das Erforschen der Eigenschaften mesoporöser Silicapartikel ist ein fundamentaler Schritt bevor ihre Verwendung in den unterschiedlichsten Bereichen realisiert werden kann. Die Schlüsselrolle spielen dabei die Kontrolle der Form und die chemische Modifikation der Partikel. Das Ziel dieser Arbeit ist die Synthese und Charakterisierung eines bestimmten Typs mesoporöser Partikel, sogenannte Arrays of Silica Nanochannels (ASNCs). Die Haupteigenschaften der ASNCs liegen darin, dass ihre Nanokanäle entlang der Hauptachse der Partikel verlaufen und die Partikel eine definierte hexagonal prismatische Morphologie aufweisen. Inspiriert durch die Resultate zu analogen mikroporösen Materialien wie etwa Zeolith L, haben wir Experimente durchgeführt, um die Form, die selektive Funktionalisierung der Oberfläche, sowie die katalytische Aktivität gezielt zu beeinflussen. Ausserdem werden in dieser Dissertation Experimente zur Auftragung von Silicapartikeln auf Polymersubstrate und Studien über pseudomorphe Transformationen diskutiert.

Das Wachstum der ASNCs wird durch eine Reihe von Parametern beeinflusst. Änderungen der Gegenionen der strukturdirigierenden Spezies beeinträchtigen die reguläre Morphologie der Partikel stark. Das Zufügen von Salzen, insbesondere KCl und $CaCl_2$, verhindert diesen unerwünschten Effekt. Die Co-Ionen sind ausserdem verantwortlich für die Vergrösserung der Porendurchmesser und beeinflussen deshalb auch das Aspektverhältnis der Partikel. Das Mischungsverhältnis zwischen Silan und Tensid ist ein weiterer Faktor, der die Bildung der Partikel beeinflusst. Das Wachstum an den Basisflächen der Partikel nimmt mit steigendem Silangehalt zu. Die Länge der Partikel, und dadurch die Länge der Nanokanäle, kann durch Anpassung dieses Basisflächenwachstums kontrolliert werden.

Das Funktionalisieren der ASNCs wird in der Regel durch Behandlungen nach der Synthese erreicht (postsynthetische Modifikationen). Der Prozess der Co-Kondensation, durchgeführt mit funktionalisierten Silanen, beeinflusst die charakteristische Morphologie der Partikel. Durch die Kombination dieser klassischen Prozesse wurde eine neue Methode entwickelt (Post-Kondensation), um funktionalisierte ASNCs in einer Eintopfreaktion zu erhalten. Die spätere Zugabe der funktionalisierten Silane bewahrt die hexagonal prismatische Partikelform. Sterische Hinderung in Verbindung mit Wachstum an den Basisflächen führte zu Partikeln, bei welchen sich die funktionellen Gruppen an den Poreneingängen

ansammelten. Eine Tandem-Post-Kondensationsmethode wurde entwickelt um die Synthese von bifunktionellen Partikeln zu ermöglichen.

Aufgrund der grossen Oberfläche (bis zu 1000 m^2/g) wird mesoporöses Silica oft als Träger für Katalysatoren verwendet. Co-Kondensations-, Post-Grafting- und Post-Kondensationsmethoden wurden für die Synthese von Silica-Titan ASNCs verwendet. Die Poreneigenschaften, die Kristallinität und die Photoaktivität der Materialien wurden untersucht.

Mesoporöse Silicapartikel auf einem Polymersubstrat können für Katalyse, Wirkstofffreisetzung und Sensortechnologien verwendet werden. Der Auftragungsprozess sollte einfach sein und eine Monolage ergeben. Um das zu erreichen, wurden verschiedene Methoden mit Polymethylmethacrylat als Trägermaterial für aminofunktionalisiertes Silica untersucht.

Die pseudomorphe Transformation von Silicapartikeln ist ein Prozess bestehend aus zwei Schritten, nämlich Auflösung und erneutes Ausfällen. Diese Methode wird verwendet um das Porensystem der Partikel von makroporös zu mesoporös umzuwandeln ohne die Morphologie zu verändern. Bimodale mesoporöse Materialien wurden durch pseudomorphe Transformationen hergestellt, ausgehend von grossporigen mesoporösen Partikeln. Die Transformation des Porensystems wurden mittels Gassorption und SAXS untersucht

.

ABBREVIATIONS

AEAPTMS: [3-(2-aminoethylamino)propyl]trimethoxysilane

AFI: aluminophosphate with sequence number five

APDIPES: 3-aminopropyldiisopropylethoxysilane

APTMEES: 3-aminopropyltris-(methoxyethoxyethoxy)silane

APTMS: 3-aminopropyltrimethoxysilane

ASNCs: arrays of silica nanochannels

BET: Brunauer-Emmett-Teller

BJH: Barrett-Joyner-Halenda

BTESPA: bis(triethoxysilylpropyl)amine

CAN: acetonitrile

CLSM: confocal laser scanning microscopy

CTAB: hexadecyltrimethylammonium bromide or cetyltrimethylammonium bromide

CTAC: hexadecyltrimethylammonium chloride or cetyltrimethylammonium chloride

DBDMS: diisobutyldimethoxysilane

DMSO: dimethyl sulfoxide

Dye-silane: pre-coupled aminosilane with a dye

F127: pluronic F127 ($PEO_{100}PPO_{65}PEO_{100}$)

FITC: fluorescein isothiocyanate

FITC-silane: FITC-coupled aminosilane

FRET: Förster resonance energy transfer

GCMC: grand canonical Monte-Carlo simulations

GLYMO: 3-glycidyloxypropyl trimethoxysilane

IUPAC: international union of pure and applied chemistry

LSCs: luminescent solar concentrators

LTL: linde type L

MB: methylene blue

MCM-41: Mobil composition of matter 41

MCM-48: Mobil composition of matter 48

MCM-50: Mobil composition of matter 50

NH-silane: amino-functional alkoxysilane

NLDFT: non-local density functional theory

P123: pluronic P123 ($PEO_{20}PPO_{70}PEO_{20}$)

PMMA: poly(methyl methacrylate)

PSD: pore size distribution

PZC: point of zero charge

RhITC: rhodamine isothiocyanate

RhITC-silane: RhITC-coupled aminosilane

R-silane: functional alkoxysilane

SAXS: small angle X-ray scattering

SBA-15: Santa Barbara amorphous material 15

SBA-16: Santa Barbara amorphous material 16

SDA: structure directing agent

SDS: sodium dodecyl sulfate

SEM: scanning electron microscopy

SLC: silicatropic liquid crystal

SN_2: second-order nucleophilic substitution

TEOS: tetraethyl orthosilicate

Ti-ASNCs: modified ASNCs containing titanium atoms

TMB: 1,3,5-trimethylbenzene or mesitylene

TMMS: methoxytrimethylsilane

TMPTA: N1-(3-trimethoxysilylpropyl)diethylenetriamine

TR: Texas red (sulforhodamine 101 acid chloride)

TTIP: titanium tetraisopropoxide

WDXRF: wavelength dispersive X-ray fluorescence

XRD: X-ray diffraction

CONTENTS

1. INTRODUCTION

Since the first report in 1992 by the Mobil Company,[1] mesoporous silica materials have been used in countless research projects. These materials have received increasing attention in the fields of catalysis,[2-4] sensors,[5] drug delivery,[6] and adsorption[7] due to the large variety of customization options in terms of pore size, pore system dimensionality, particle size, particle morphology, and surface functional groups. An example of well-defined particles with highly ordered mesostructure are the so called arrays of silica nanochannels (ASNCs). ASNCs are a MCM-41 type material featuring well-defined hexagonal prismatic particles with the channel (pore) entrances located on the base surfaces,[8-12] as schematically shown in Figure 1.1.

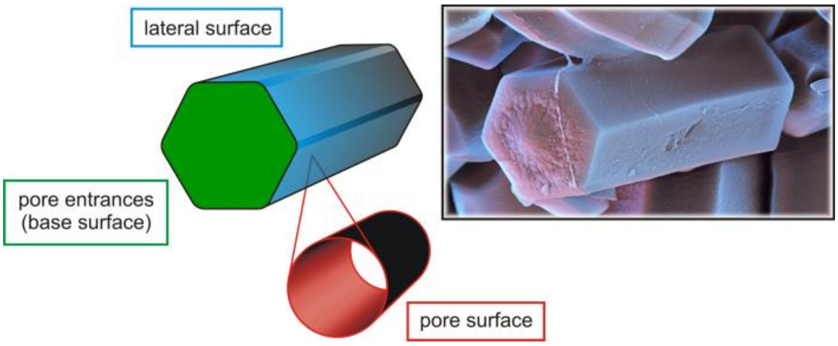

Figure 1.1 Illustration of the different surface regions of ASNCs. The particle shown in the scanning electron microscopy image has a length of approximately 5 µm. The average pore (nanochannel) diameter is typically in the range of 2.5 to 4 nm.[13]

1.1 Tuning the aspect ratio of arrays of silica nanochannels

The morphogenesis of mesoporous silica fibers was first proposed by Ozin and co-workers.[14] Liquid-crystal embryos with hexagonal cross-section start to grow after the addition of silane. The final shape of the particles depends on the reaction conditions. It has been observed that pH, dielectric constant, and ionic strength influence the starting shape and the subsequent growth. Classical ASNCs, as originally reported by Kievsky and Sokolov,[9] are a few micrometers long with a large aspect ratio (length/diameter). The synthesis is conducted at low pH with hexadecyltrimethylammonium chloride (CTAC) as structure-directing agent. Control of the length, diameter, and aspect ratio of ASNCs is desirable, as it would open possibilities for tailor-made host materials, *e.g.* with adaptable nanochannel length. The first part of the work was to identify parameters in the synthesis of ASNCs that influence the aspect ratio of ASNCs, while retaining a narrow pore size distribution and a well-defined hexagonal prismatic particle shape (Figure 1.2).

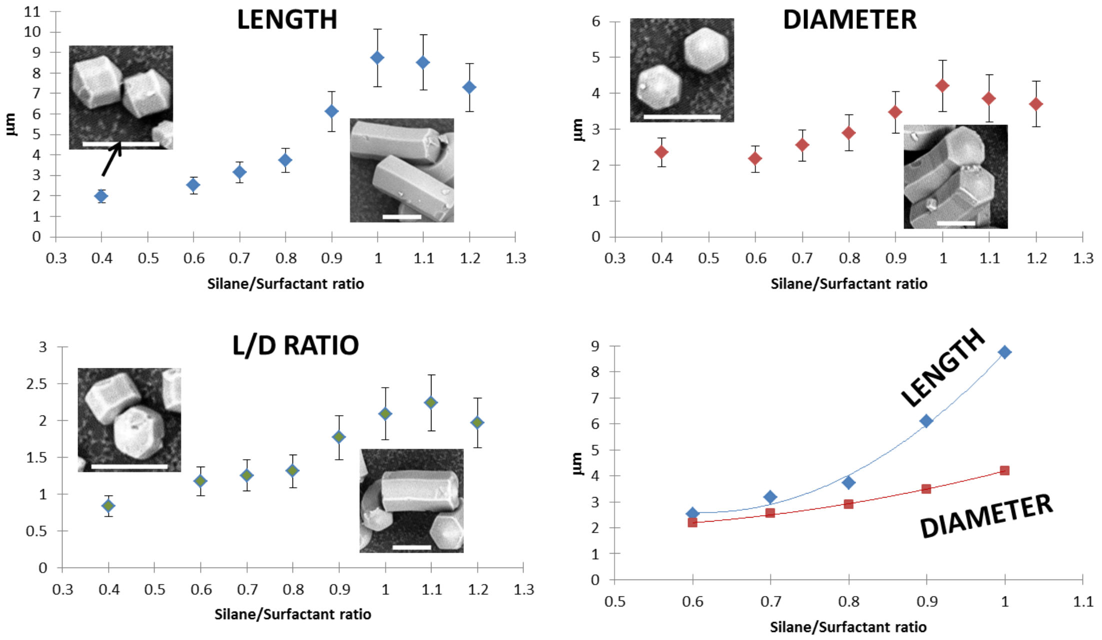

Figure 1.2 Graphs of ASNCs length, diameter and aspect ratio synthesized with different silane/surfactant ratios. The SEM pictures correspond to samples prepared with a silane/surfactant ratio of 0.4 and 1.0. The scale bars are 5 μm.

1.2 Functionalization of arrays of silica nanochannels by post-condensation

The introduction of functional groups into the mesoporous silica framework is usually achieved by postsynthetic treatment (grafting) or by co-condensation.[15] Advantages and disadvantages of these methods have been studied extensively. Postsynthetic functionalization introduces the functional groups after the formation of the mesoporous silica particles. The particle size and shape are preserved. While this method is not ideal for achieving uniform distributions of functional groups, distinctively non-uniform distributions, such as a selective functionalization of the external particle surface, are possible.[8,16-18] Co-condensation is the method of choice when a uniform distribution of the functional groups is desired. Functional groups are incorporated into the silica framework, typically via the respective alkoxysilanes, during the formation of the mesoporous structure. Contrary to postsynthetic functionalization, which often uses an organic solvent for the functionalization step, this convenient one-pot method relies solely on reactions in aqueous phase. The presence of functional alkoxysilanes in the reaction mixture can affect the outcome of the synthesis in terms of particle size, particle morphology, and degree of ordering.[19-25] High levels of functionalization generally result in a loss of ordering and in increasingly broad pore size distributions. The functionalization of ASNCs has so far only been achieved by postsynthetic treatment,[8, 11, 26] as the particle morphology is very sensitive to the conditions during the condensation of the silica framework. In order to allow for a one-pot reaction, we have developed a method that combines postsynthetic treatment with co-condensation. In this so-called post-condensation pathway, the functional alkoxysilanes are introduced into the ASNCs formation process after stabilization of the particle morphology (Chapter 2.2, Figure 1.3).

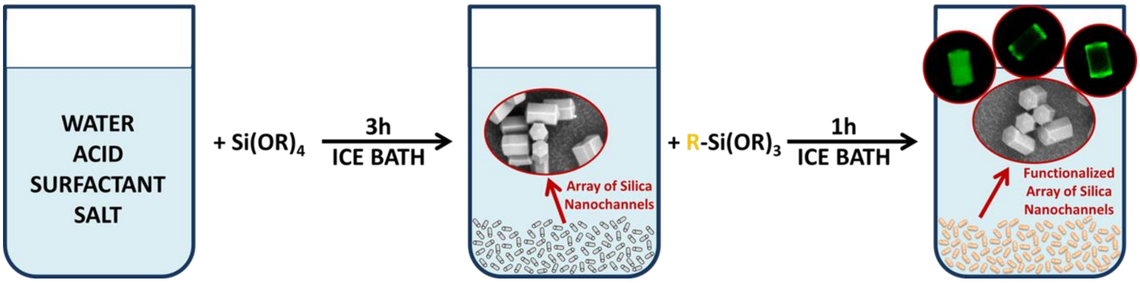

Figure 1.3 Scheme of post-condensation reaction of ASNCs. The condensation of the functionalized silane starts when the particles reach the desired shape.

1.3 Synthesis and characterization of ordered mesoporous silica-titania particles

Air and water pollution increased the attention on fundamental and applied research of environmental remediation.[27-29] Considering the high chemical stability, the low cost and the convenient synthesis of the different species, titanium dioxide (titania or TiO_2) is the perfect starting point to achieve good results for photochemical pollutant degradation. TiO_2 is generally supported on amorphous silica to prevent problems such as leaching in aqueous media and to facilitate the recovery processes.[30,31] The nature of the support and the preparation method determines the photoactivity by affecting the crystallinity of TiO_2 and the adsorption of the organic pollutant. Porous silicates such as zeolites and mesoporous silica have been used as supports.[31,32] A mixed porous framework composed of silica and titania is another possibility to achieve good results in terms of photodegradation. Using the ASNCs growth process and co-condensation, impregnation (post-grafting) and post-condensation methods, we prepared mesoporous particles composed of a mixture of silica and titania and tested the photocatalytic activity.

1.4 Mesoporous silica monolayers

ASNCs can be considered as the mesoporous analogue to hexagonal zeolites such as zeolite L (LTL framework)[33-35] or $AlPO_4$-5 (AFI framework).[36-38] Interesting results were obtained in the organization of micrometer-sized zeolite crystals achieving a perpendicular alignment of the channels to the substrate (Figure 1.4). Physical adsorption and covalent bonds between particles and substrate are the methods to realize an oriented monolayer of particles.[39-43]

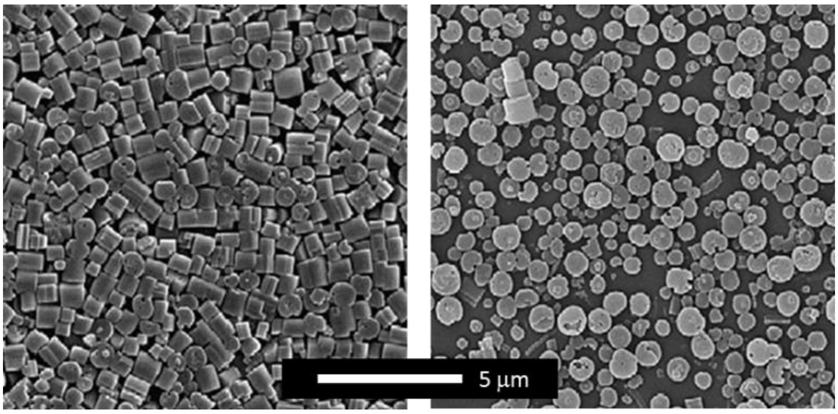

Figure 1.4 SEM images of a zeolite L monolayer (left) and the corresponding oriented zeolite L monolayer (right).[39]

The selective surface functionalization of the particles is a fundamental step before the grafting process. The presence of reactive groups on the base surface (pore entrances) increases the probability of achieving the correct disposition of the particles by creating specific bonds with the substrate surface. Preliminary grafting experiments were performed with functionalized particles and poly(methyl methacrylate).

1.5 Pseudomorphic transformation of SBA-15 and SBA-16

An elegant way to alter the pore size of a mesoporous material without affecting its particle size and shape was proposed by Martin et al. [44] This so-called pseudomorphic transformation pathway uses a structure-directing agent (SDA) to rearrange the pore system of a preformed macroporous material. Functional groups can be introduced during the transformation and the pore size can be adjusted to a certain degree by using differently sized SDAs (Figure 1.5).[45]

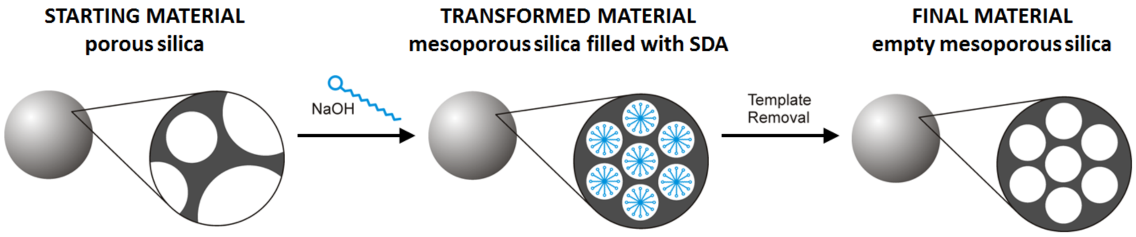

Figure 1.5 Schematic of pseudomorphic transformation.[45]

MCM-41 type silica tubes[46] and monodisperse magnetic mesoporous silica microspheres[47] have been prepared by pseudomorphic transformation of silica shells deposited onto hard templates. Pseudomorphic transformation can also be applied to millimeter-sized silica spheres[48] or to an ordered mesoporous material such as SBA-15, thus converting its pore system into a MCM-41 type structure.[49] Bimodal mesoporous materials with two well-defined pore size regimes have been prepared by carefully balancing the degree of pseudomorphic transformation. Partial pseudomorphic transformation was shown to alter the structure of the porous starting material from the outside to the inside, thus virtually creating a shell with a reduced pore size. The pH thereby governs the equilibrium between dissolution and reprecipitation of the silica matrix.[49] Based on these previous results we can make the general conclusion that the partial pseudomorphic transformation of SBA-15 in the presence of hexadecyltrimethylammonium bromide (CTAB) yields a material consisting of two types of pore size domains, one originating from the SBA-15 starting material, and the other being formed by a rearrangement of the original pore structure in the presence of the SDA. The question remains whether this newly introduced pore structure can in fact be considered as a true MCM-41 type structure, i.e., a hexagonal arrangement of one-dimensional pores. Furthermore, the role of the original pore structure in determining the structure of the newly introduced domains is unclear. We have therefore investigated the partial pseudomorphic transformation of SBA-15 (one-dimensional pore structure, space group (*P6mm*) and of SBA-16 (three-dimensional pore structure, space group $Im\bar{3}m$) in the presence of CTAB.

1.6 References

1. J. S. Beck, J. C. Vartuli, W. J. Roth, M. E. Leonowicz, C. T. Kresge, K. D. Schmitt, C. T.-W. Chu, D. H. Olson, E. W. Sheppard, S. B. McCullen, J. B. Higgins and J. L. Schlenker, J. Am. Chem. Soc., 1992, 114, 10834-10843.
2. L.-B. Sun, X.-Q. Liu and H.-C. Zhou, Chem. Soc. Rev., 2015, 44, 5092-5147.
3. S. Rostamnia and E. Doustkhah, RSC Adv., 2014, 4, 28238-28248.
4. X. Qian, K. Fuku, Y. Kuwahara, T. Kamegawa, K. Mori and H. Yamashita, ChemSusChem, 2014, 7, 1528-1536.
5. F. Sancenón, L. Pascual, M. Oroval, E. Aznar and R. Martinez-Máñez, ChemistryOpen, 2015, 4, 418-437.
6. S. Alberti, G. J. A. A. Soler-Illia and O. Azzaroni, Chem. Commun., 2015, 51, 6050-6075.
7. A. Walcarius and L. Mercier, J. Mater. Chem., 2010, 20, 4478-4511.
8. N. Gartmann and D. Brühwiler, Angew. Chem., Int. Ed., 2009, 48, 6354-6356.
9. Y. Kievsky and I. Sokolov, IEEE Trans. Nanotechnol., 2005, 4, 490-494.
10. D. O. Volkov, J. Benson, Y. Y. Kievsky and I. Sokolov, Phys. Chem. Chem. Phys., 2010, 12, 341-344.
11. N. Gartmann, C. Schütze, H. Ritter and D. Brühwiler, J. Phys. Chem. Lett., 2010, 1, 379-382.
12. N. Zucchetto and D. Brühwiler, RSC Adv., 2015, 5, 74638-74644.
13. N. Zucchetto and D. Brühwiler, Dalton Trans., 2016, 45, 14363-14369.
14. H. Yang, N. Coombs and G. A. Ozin, Nature, 1997, 386, 692-695.
15. F. Hoffmann, M. Cornelius, J. Morell and M. Fröba, Angew. Chem. Int. Ed., 2006, 45, 3216-3251.
16. D. S. Shephard, W. Zhou, T. Maschmeyer, J. M. Matters, C. L. Roper, S. Parsons, B. F. G. Johnson and M. J. Duer, Angew. Chem. Int. Ed., 1998, 37, 2719-2723.
17. K. Cheng and C. C. Landry, J. Am. Chem. Soc., 2007, 129, 9674-9685.

18. Y. Huang, S. Xu and V. S.-Y. Lin, Angew. Chem. Int. Ed., 2011, 50, 661-664.
19. S. Huh, J. W. Wiench, J.-C. Yoo, M. Pruski and V. S.-Y. Lin, Chem. Mater., 2003, 15, 4247-4256.
20. S. Sadasivan, D. Khushalani and S. Mann, J. Mater. Chem., 2003, 13, 1023-1029.
21. J. L. Blin, C. Gérardin, L. Rodehüser, C. Selve and M. J. Stébé, Chem. Mater., 2004, 16, 5071-5080.
22. C. Yang, Y. Wang, B. Zibrowius and F. Schüth, Phys. Chem. Chem. Phys., 2004, 6, 2461-2467.
23. R. P. Hodgkins, A. E. Garcia-Bennett and P. A. Wright, Microporous Mesoporous Mater., 2005, 79, 241-252.
24. K. Möller, J. Kobler and T. Bein, J. Mater. Chem., 2007, 17, 624-631.
25. F. O. M. Gaslain, C. Delacôte, A. Walcarius and B. Lebeau, J. Sol-Gel Sci. Technol., 2009, 49, 112-124.
26. N. Gartmann and D. Brühwiler, Materials, 2011, 4, 1096-1103.
27. A. Mills, H. R. Davies and D. Worsley, Chem. Soc. Rev., 1993, 22, 417-425.
28. D. M. Tobaldi, R. C. Pullar, C. Piccirillo, P. M. L. Castro, M. M. Pintado, M. P. Seabra and J. A. Labrincha, Handbook of Functional Nanomaterials, 2014, 4, 69-91.
29. C. M. The and A. M. Rahman, Journal of Alloys and Compounds, 2011, 509, 1648-1660.
30. Z. Luan, E. M. Maes, P. A. W. van der Heide, D. Zhao, R. S. Czernuszewicz and L. Kevan, Chem. Mater., 1999, 11, 3680-3686.
31. X. Quin, K. Fuku, Y. Kuwahara, T. Kamegawa, K. Mori and H. Yamashita, Chem. Sus. Chem., 2014, 7, 1528-1536.
32. F. Zhang, Y. Zheng, Y. Cao, C. Chen, Y. Zhan, X. Lin, Q. Zheng, K. Wie and J. Zhu, J. Mater. Chem., 2009, 19, 2771-2777.
33. A. Zabala Ruiz, D. Brühwiler, T. Ban and G. Calzaferri, Monatsh. Chem., 2005, 136, 77-89.
34. A. G. Gomez, G. de Silveira, H. Doan and C.-H. Cheng, Chem. Commun., 2011, 47, 5876-5878.
35. A. I. Lupulescu, M. Kumar and J. D. Rimer, J. Am. Chem. Soc., 2013, 135, 6608-6617.
36. T. Kodaira, K. Miyazawa, T. Ikeda and Y. Kiyozumi, Microporous Mesoporous Mater., 1999, 29, 329-337.
37. F. Y. Jiang, Z. K. Tang, J. P. Zhai, J. T. Ye and J. R. Han, Microporous Mesoporous Mater., 2006, 92, 129-133.

38. Z. Liu, T. Wakihara, D. Nishioka, K. Oshima, T. Takewaki and T. Okubo, Chem. Mater., 2014, 26, 2327-2331.
39. A. Zabala Ruiz, H. Li and G. Calzaferri, Angew. Chem., Int. Ed., 2006, 45, 5282-5287.
40. J. S. Lee, H. Lim, K. Ha, H. Cheong and K. B. Yoon, Angew. Chem., Int. Ed., 2006, 45, 5288-5292.
41. K. Ha, Y.-J. Lee, H. J. Lee and K. B. Yoon, Adv. Mater., 2000, 12, 1114-1117.
42. J. S. Lee, K. Ha, Y.-J. Lee and K. B. Yoon, Adv. Mater., 2005, 17, 837-841.
43. Y. Wang, H. Li, B. Liu, Q. Gan, Q. Dong, G. Calzaferri and Z. Sun, J. Solid State Chem., 2008, 181, 2469-2472.
44. T. Martin, A. Galarneau, F. Di Renzo, F. Fajula and D. Plee, Angew. Chem., Int. Ed., 2002, 41, 2590-2592.
45. M. J. Reber and D. Brühwiler, Part. Part. Syst. Charact., 2015, 32, 243-250.
46. J. Patzsch and J. J. Schneider, Dalton Trans., 2013, 42, 1451-1460.
47. G.-T. Zhu, X.-S. Li, Q. Gao, N.-W. Zhao, B.-F. Yuan and Y.-Q. Feng, J. Chromatogr. A, 2012, 1224, 11-18.
48. X. Li, D. Wu, J. Wang, W. Zhu, Y. Luo, C. Han, W. Ma and S. He, Microporous Mesoporous Mater., 2016, 226, 309-315.
49. M. J. Reber and D. Brühwiler, Dalton Trans. 2015, 44, 17960-17967.

2. GENERAL THEORY

2.1 Sol-gel chemistry

The process that governs the formation of the silica particles is the sol-gel process. This method is generally used to produce metal oxides of silicon and titanium starting from the respective alkoxides. The particle production is only one of many applications of sol-gel chemistry. In fact the colloidal solution (sol) can be adapted and processed to produce a uniform polymeric network (gel)[1-2] for the preparation of thin films, coatings, dense ceramics, aerogels and fibers (Figure 2.1).[3]

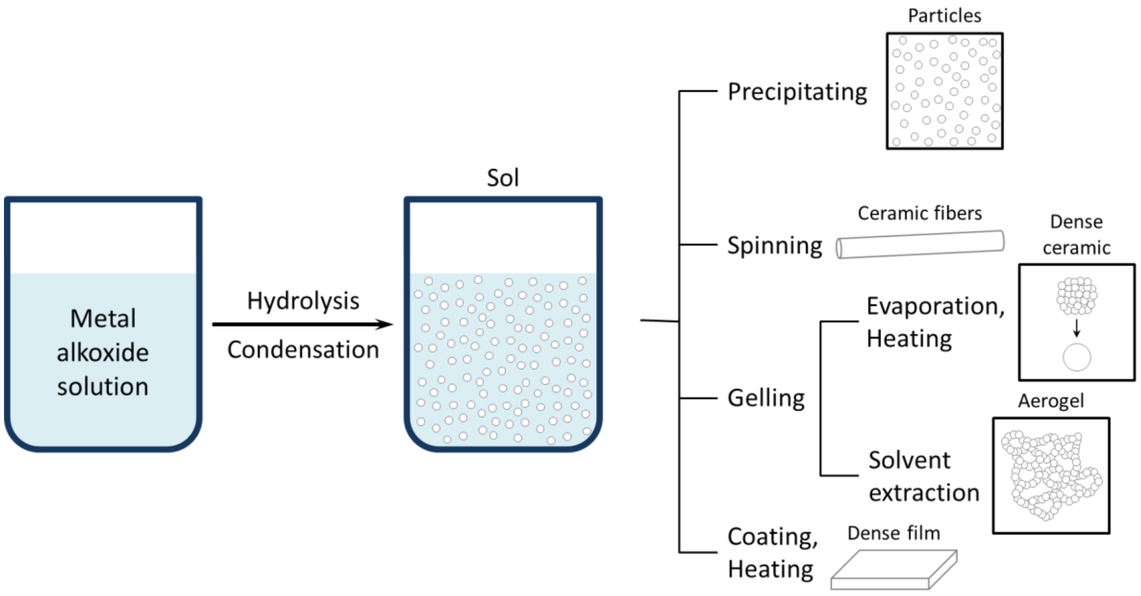

Figure 2.1 Sol-gel applications.

The particles obtained with the process shown in Figure 2.1 are generally non-porous or microporous and are known as Stöber particles.[4] ASNCs and the other types of mesoporous materials are synthesized using silicon alkoxides as a silica source and surfactants as structure directing agents. In both cases the particles obtained are considered gel-phase materials or polymeric networks with a connected liquid phase.

2.1.1 General process

The sol-gel process begins with the formation of the sol from the precursors. Subsequently, the sol-gel transition occurs and the inorganic framework grows. Hydrolysis and condensation are the reactions that govern this transformation. In the case of silicon alkoxide, the hydrolysis reaction is:

$$Si(OR)_4 + H_2O \rightarrow (RO)_3SiOH + ROH \qquad (2.1)$$

The oxygen of water is the nucleophile that attacks the silicon atom.[5] This reaction should generate a silanol group Si−OH (Eq. 2.1), however, the reaction rate is very slow, thus requiring a catalyst. Co-solvents play an important role during this step. The presence of these homogenizing agents (alcohols, dioxane, THF, acetone etc.) improves the hydrolysis, facilitating the process especially for bulky alkoxysilanes.[5] With the formation of the silanol groups the condensation reactions start. The −Si−O−Si− units are obtained by:

$$\equiv Si{-}OH + \equiv Si{-}OH \rightarrow \equiv Si{-}O{-}Si\equiv + H_2O \qquad (2.2)$$

$$\equiv Si{-}OH + \equiv Si{-}OR \rightarrow \equiv Si{-}O{-}Si\equiv + ROH \qquad (2.3)$$

The condensation step releases water (Eq. 2.2) or alcohol (Eq. 2.3) molecules. The polycondensation reactions form an extended silica network whose structure and growth depend on a set of synthesis parameters.

2.1.2 Hydrolysis

A catalyst is required to start the hydrolysis reaction. The gel structure and the sol-gel transition largely depend on the choice of catalyst.[6] The common routes to have a complete and rapid hydrolysis are performed in acidic and basic conditions. In acidic solutions protonation of the alkoxy group occurs, thereby increasing the electrophilicity of the silicon atom (Figure 2.2). The mechanism reported in Figure 2.2 shows a S_N2-type reaction.

Different authors have discussed the inversion of the silicon tetrahedron (typical of S_N2 reactions) because this mechanism is not always correct.[5]

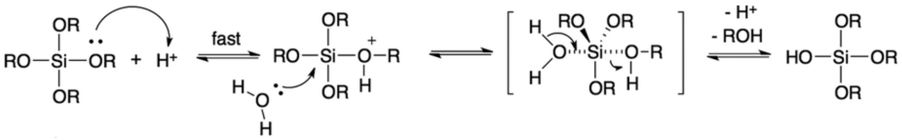

Figure 2.2 Mechanism of alkoxysilane hydrolysis in acidic conditions.[7]

With good leaving groups (such as Cl^- or $RCOO^-$) the inversion takes place (S_N2 reaction), while for poor leaving groups (such as H^- or RO^-) the solvent polarity regulates the inversion. In fact, the inversion is facilitated in polar protic solvents.[5] Furthermore, the alkyl chain length has an effect on the hydrolysis rate. The rate is lower when the alkoxy groups are more branched. In basic solutions the nucleophilicity of the hydroxyl ions (OH^-) is strong enough to attack directly the silicon atom (Figure 2.3) following a S_N2 mechanism.[5]

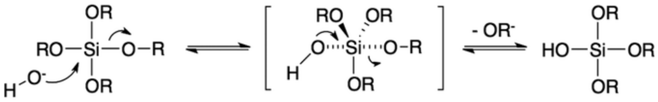

Figure 2.3 Mechanism of alkoxysilane hydrolysis in basic conditions.[7]

This process is influenced by inductive and steric effects. Substituents such as −OH or −OSi (electron withdrawing) stabilize the negative charge on silicon and enhance the hydrolysis rate.

2.1.3 Condensation

The condensation reaction forms siloxane bonds releasing water or alcohol molecules (Eq. 2.2 and Eq. 2.3).The catalyst used to hydrolyze the starting precursor modifies the electronic density of the silicon atom.

The mechanism of condensation with acid catalysts is reported in Figure 2.4.

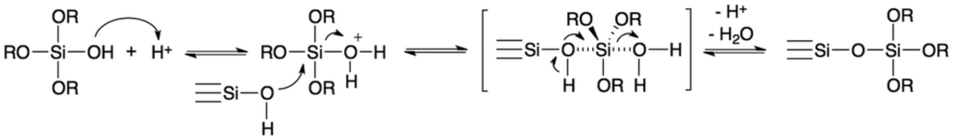

Figure 2.4 Mechanism of condensation in acidic conditions.[7]

The silicon atom is more electrophilic after the silanol protonation and therefore more susceptible to nucleophilic attack. The silanols contained in monomers or slightly branched oligomers are readily protonated because they are the most basic silanol species. Consequently, the condesation reactions occur between these protonated silanols (located on monomers or at the end of the oligomer chains) and the neutral species (R−Si(OH)$_3$).[5] The high reactivity of the electrophilic silicon atom favours the formation of chain-like structures as shown in Figure 2.5.

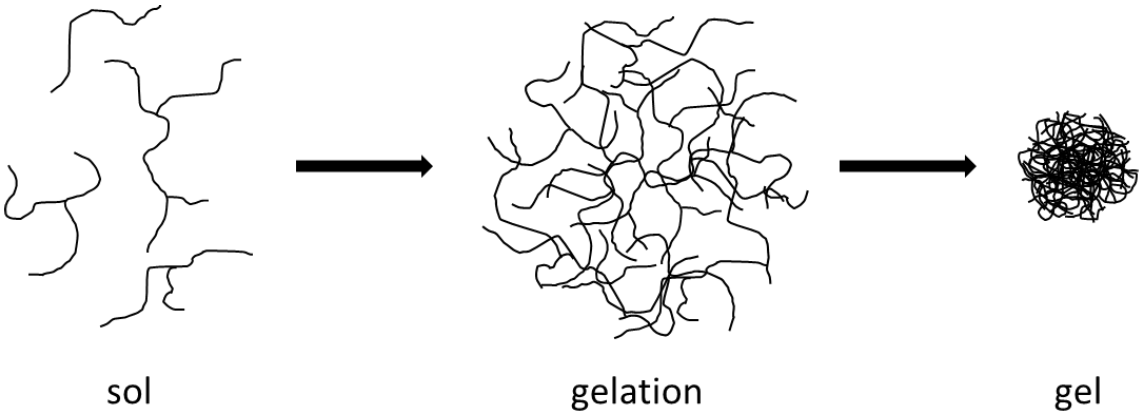

Figure 2.5 Scheme of gel formation in an acid catalyzed sol-gel reaction.

Differently from the acidic pathway, under basic conditions the deprotonated silanols (≡Si−O$^-$) are better nucleophiles than water and silanol species.

The condensation involves deprotonated silanols (preferentially a highly condensed species) and the hydrolyzed silanes (preferentially a weakly branched species) with the formation of a pentacoordinate intermediate as shown in Figure 2.6.

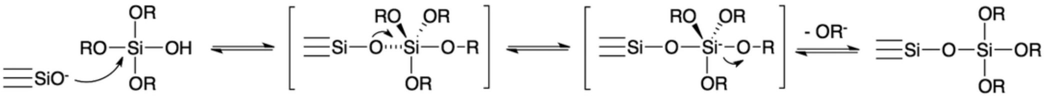

Figure 2.6 Mechanism of condensation in basic conditions.[7]

The reduced electron density on the silicon atom increases the acidity of the silanol when −OH or −OR groups are replaced with ≡Si−O$^-$ groups. The result of basic catalysis is an aggregation (monomer-cluster) that leads to more compact highly branched silica networks (Figure 2.7).

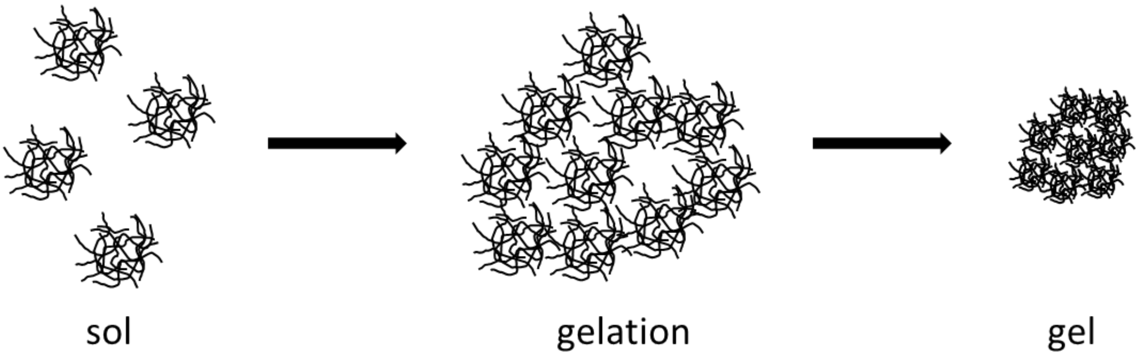

Figure 2.7 Scheme of gel formation in a basic catalyzed sol-gel reaction.

For the silicon alkoxides the reaction rates of hydrolysis and condensation are strongly pH dependent. This dependency is schematized in Figure 2.8. As explained previously, the hydrolysis is slow without catalyst in aqueous solution (pH≈7), while the rate increases in acid or basic conditions. The pH dependence of the condensation process is more complicated because different factors influence the reaction rate. The superficial electrical charges modify the reactivity, in fact around the point of zero charge (PZC, the electrical charge density on a surface is zero) at pH between 1.8 and 4.2 (for silica containing silanol groups) the sol is stable and the condensation rate is very slow.[8] Below and above the PZC, the rate increases, reaching the upper limit at pH around 10. The depolymerization process is favored at higher pH leading to a decrease of the reaction rate.[5]

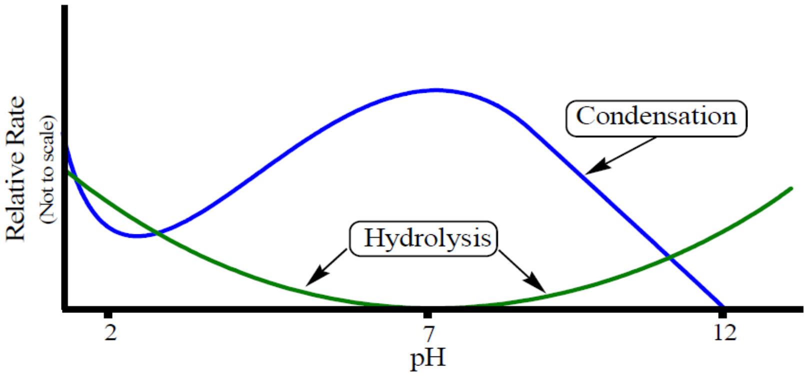

Figure 2.8 Relative hydrolysis and condensation rates as a function of pH for a silicon alkoxide.[9]

2.2 Mesoporous silica materials

The wide range of applications of porous materials has led the scientific community to focus on their synthesis, characterization and functionalization, in particular materials based on MCM-41 (Mobil Composition of the Matter) and similar silicates prepared by hydrothermal synthesis with a structure directing agent (SDA) as a framework template.[10]

2.2.1 Classification

The IUPAC nomenclature divides porous materials into three different categories: microporous materials (pore diameter < 2 nm), mesoporous materials (pore diameter between 2 nm and 50 nm) and macroporous materials (pore diameter > 50 nm).[11] The most prominent examples of microporous substances are zeolites, aluminosilicate minerals with a defined pore size and with crystalline pore walls. The macroporous region is composed by gels and glasses with broad pore size distributions. Ordered mesoporous materials with a narrow pore size distribution were prepared using lyotropic liquid crystals as SDAs.[10,12] Particles with large surface area and pores in the range from 2 to 50 nm extend the possibility to use guest molecules that are larger than the pore size covered by zeolites.

2.2.2 Synthesis

The assembly of organic (SDA) and inorganic (silica source) species is determined by forces such as hydrogen bonding, van der Waals forces, and ionic interactions between the surfactant molecules and the inorganic silica species. The cooperative self-assembly of the surfactants and the silica species results in the mesostructured composites.[13]

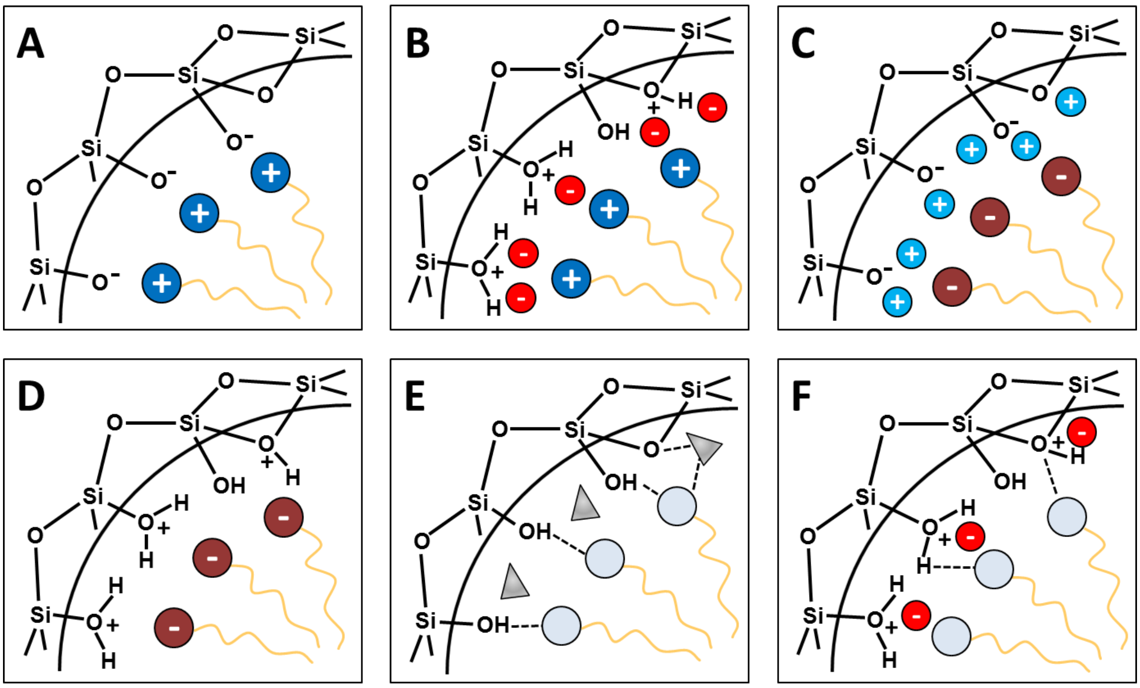

Figure 2.9 Interactions between SDA heads and silica precursors during condensation: direct electrostatic interaction S^+I^- (A) and S^-I^+ (D); mediated electrostatic interaction $S^+X^-I^+$ (B) and $S^-M^+I^-$ (C); neutral interaction S^0I^0/N^0I^0 (E) and mixed neutral-electrostatic interaction $S^0(XI)^0$ (F).

The mechanisms for the electrostatic templating routes of mesoporous materials were proposed in 1994 by Stucky et al.[13] and are illustrated in Figure 2.9. The solution pH influences the charge of the silicate species and consequently the interactions with the surfactant. Depending on the pH, the inorganic source I is protonated (I^+, acidic pH), neutral (I^0, neutral pH) or deprotonated (I^-, basic pH). The surfactant S can be cationic (S^+), anionic (S^-) or neutral (S^0) and the interactions with the silica are generally mediated by counter-ions (M^+ for cation and X^- for anion) or neutral species (N^0). The growth of ASNCs is driven by the formation of mesoporous intermediates of the type $S^+X^-I^+$ (Figure 2.9, panel B) containing the cationic surfactant (S^+, hexadecyltrimethylammonium CTA^+), the counter-ion (X^-, Cl^-) and protonated silicate species (I^+). The cooperative templating mechanisms only describe a part of the formation of the mesoporous framework. Figure 2.10 shows the cooperative organization of silicate-surfactant mesophases.[14]

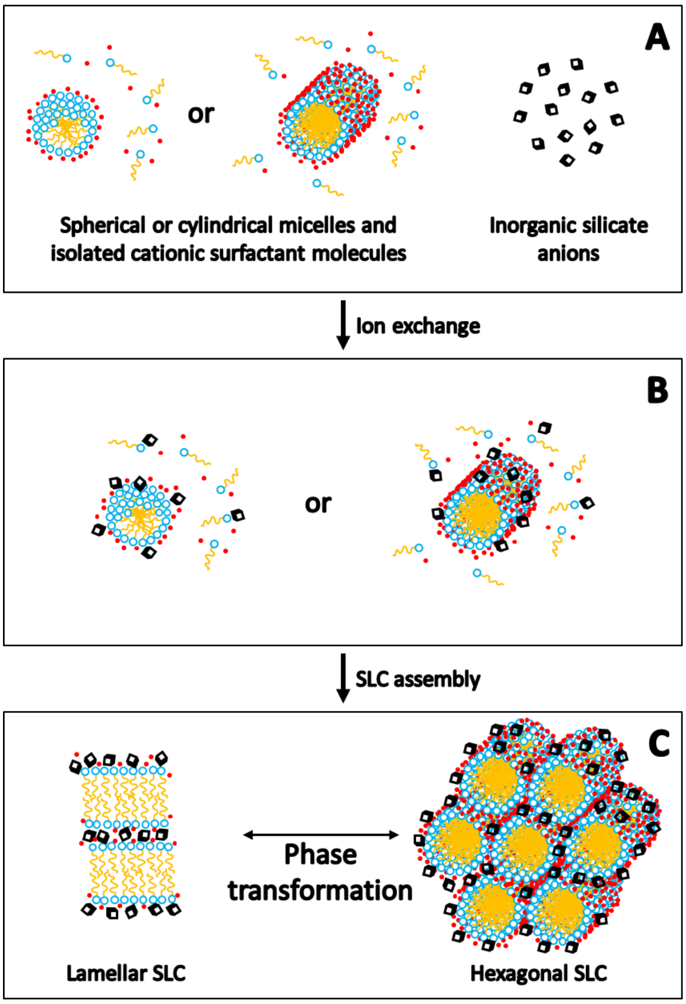

Figure 2.10 Schematic diagram of the cooperative organization of silicate-surfactant mesophases.

The process is composed by three steps: (A) the surfactant forms micelles in solution; (B) an ion exchange occurs upon mixing the surfactant solution with the silicate anions; (C) after a self-organization process the silicatropic liquid crystals (SLC or lyotropic liquid crystal) are formed and the condensation of the silica precursors takes place. The template is required for the framework formation but must be removed to obtain an open porous structure. The well-known methods to detach the surfactant are calcination and solvent extraction. During calcination, the as-synthesized materials are heated in air and the organics are burned. This heating treatment leads to framework condensation affecting the mesoscopic order[15,16] and modifying the wettability. An alternative method for surfactant removal is based on the extraction of the organic template. This can be achieved by solvent extraction or acid treatment.[17-20] Generally for MCM-41 materials, an acidic alcoholic solution is used. The extraction is based on an ion exchange and the efficiency is increased when using strong acid or small cations.[19] This suggests that the size and the mobility of the ions play a fundamental role during extraction. This method provides an alternative to calcination especially in the case of non-siliceous mesophases with low thermal stability.

2.2.3 Framework

The utilization of different SDAs leads to materials whose structure, composition, and pore size can be tailored during the synthesis. The pore geometries are manifold and various X-ray diffraction (XRD) patterns are obtained.[21] MCM-41 and SBA-15 have hexagonal geometry, MCM-50 laminar and MCM-48 and SBA-16 cubic (Figure 2.11). XRD is used to determine the ordering of the channels in the mesoporous silica phase.[10,21]

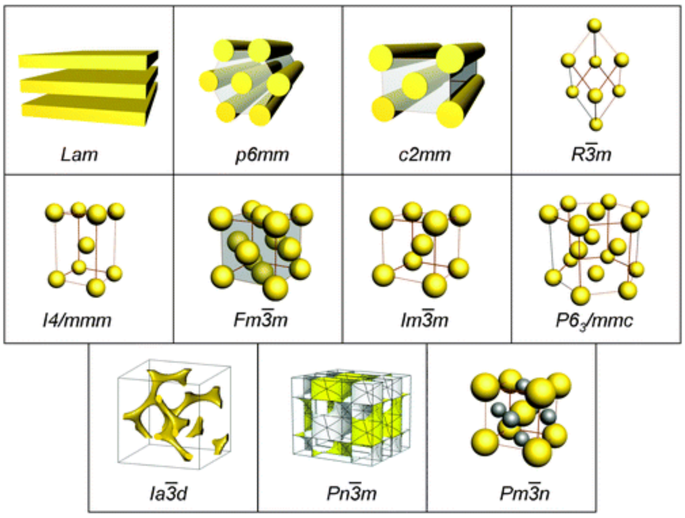

Figure 2.11 Mesoporous silica pore and framework geometries.[22]

2.2.4 Functionalization

The selective functionalization of the different surface regions of ASNCs (Figure 1.1) is a challenge. The external surface (base and lateral surfaces) has been functionalized by a postsynthetic reaction with a sterically hindered amino-functional trialkoxysilane in a nonpolar solvent.[19] In the post-condensation method, the functional alkoxysilanes (R-silanes) are introduced into the reaction after stabilization of the ASNCs particle morphology. The end-on growth and the hindrance of the R-silanes play a key role for the positioning of the functional groups at the pore entrances. Furthermore, this process was developed to work as one-pot reaction in aqueous medium avoiding organic solvents. The schemes of the functionalization methods post-grafting, co-condensation and post-condensation are reported in Figure 2.12.

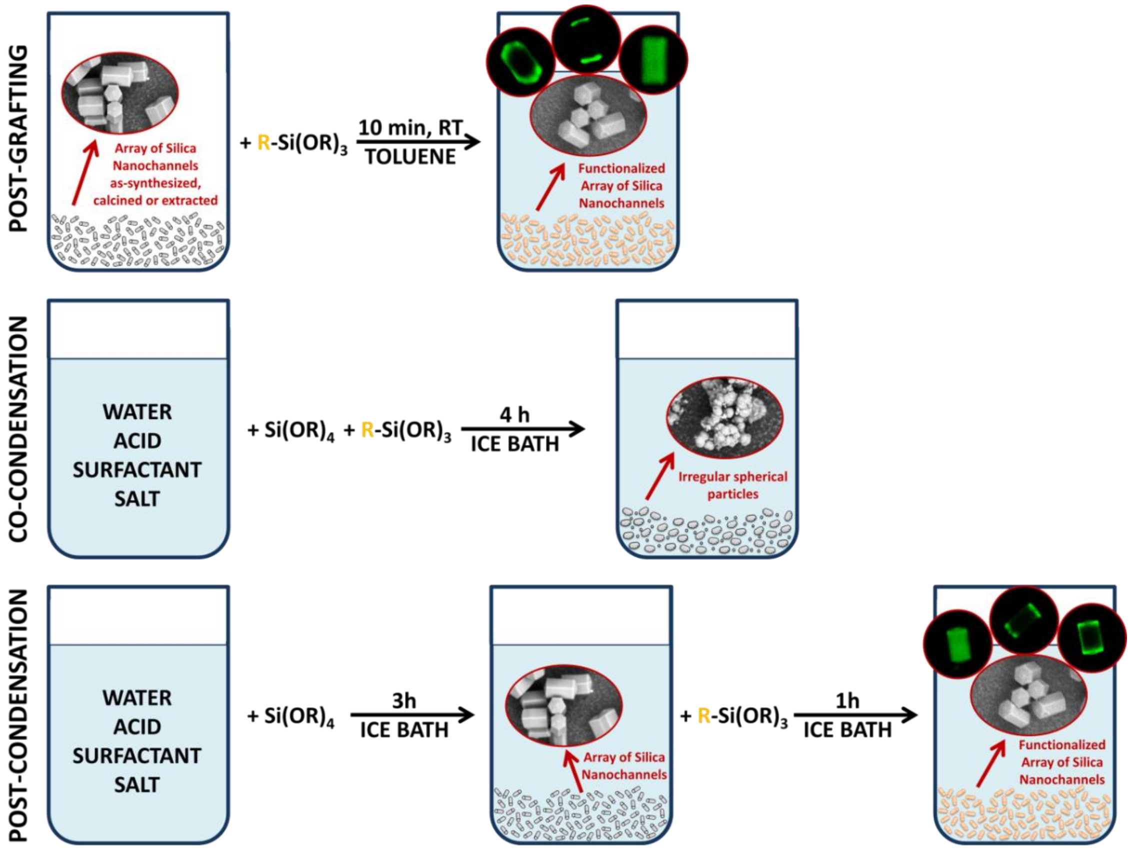

Figure 2.12 Schemes of ASNCs functionalization. Top: postsynthetic treatment.[19] *CLSM pictures (right) show the results obtained with as-synthesized, calcined and extracted particles (from left to right) functionalized with [3-(2-aminoethylamino)propyl]trimethoxysilane (AEAPTMS). Middle: co-condensation with the ASNCs synthesis condition. Bottom: post-condensation reaction. The condensation of the functionalized silane starts when the particles reach the desired shape. CLSM pictures (right) show the results obtained with different aminosilanes,*[38] *complete functionalization with 3-aminopropyltrimethoxysilane (APTMS), pore entrance functionalization with N1-(3-trimethoxysilylpropyl)diethylenetriamine (TMPTA) and external functionalization with bis(triethoxysilylpropyl)amine (BTESPA) (from left to right).*

2.2.5 Arrays of silica nanochannels

The peculiarity of these short hexagonal rods (Figure 2.13) is that the nanochannels run along the long axis and the entrances are located on the base surface. ASNCs can thus be considered as the mesoporous analogue to hexagonal zeolites with one-dimensional channel systems.[38] A very important difference between these particles is the pore size. ASNCs are mesoporous, whereas zeolites are microporous.

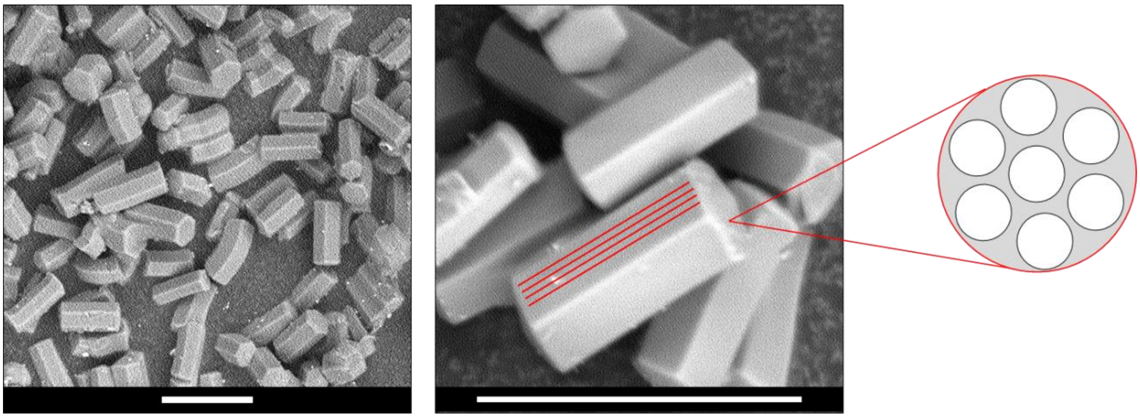

Figure 2.13 SEM images of ASNCs showing the regular hexagonal prismatic shape. The red lines represent the channel disposition along the particle length. The scale bars are 10 µm.

Ozin and co-workers explained the relation between synthesis composition and shape.[39] These studies revealed that low pH and large electrical double layer repulsions favor end-on growth (homeotropic anchoring) leading to fiber-based morphologies.[40] Furthermore, less acidic conditions facilitate side-on growth (planar anchoring) with the formation of discoids or spheres as shown in Figure 2.14.

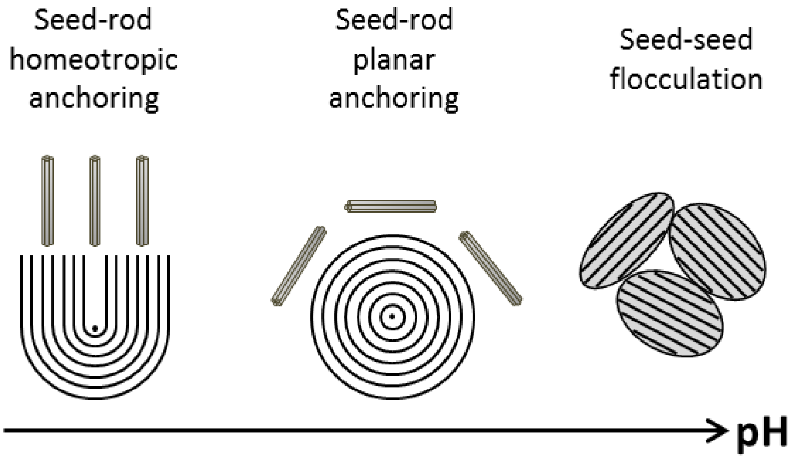

Figure 2.14 Defect and director field patterns and growth of silicate liquid crystal seeds in the synthesis of mesoporous silica with different curved shapes.[39]

The synthesis of ASNCs is generally conducted at low pH with hexadecyltrimethylammonium chloride (CTAC) as structure-direct agent and at low temperature to stabilize the growth of silicate liquid crystals. As explained in Chapter 2.2.2, the growth of the ASNCs is driven by the formation of mesoporous intermediates of the type $S^+X^-I^+$, containing the cationic surfactant (S^+), the counter-ion (X^-; Cl^- in the case of CTAC), and the protonated silicate species (I^+). Time and temperature play an essential role in the synthesis of ASNCs. Further parameters to be considered are the composition and the surfactant-solution interactions.

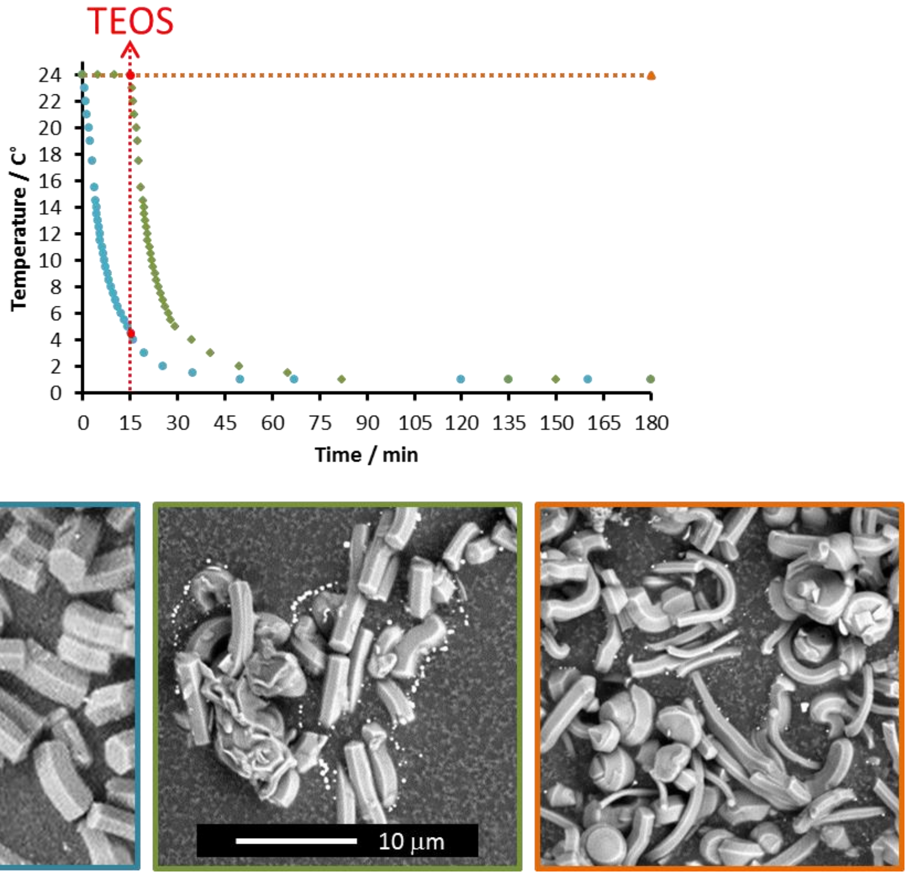

Figure 2.15 Top: temperature-time diagram of the ASNCs synthesis. The red arrow indicates the addition of TEOS to the low pH SDA solution. Bottom: SEM images of mesoporous silica fibers prepared at different temperatures. From left to right: normal synthesis (blue dots), room temperature aging synthesis (green dots) and room temperature synthesis (orange dots).

While the surfactant is dissolving, before the addition of TEOS, the formation of micelles is observed, leading to the appearance of long micellar rods. The quiescent period at low temperature is a fundamental step, as the system energy decreases and micellar interactions are established. Upon addition of TEOS, silica growth from seeds to rods starts, driven by the formation of mesoporous intermediates $S^+X^-I^+$. In the classical synthesis of ASNCs using

CTAC, only Cl^- is present as counter-ion and the yield in terms of a regular hexagonal prismatic shape is high. Upon varying the temperature of the system (room temperature) before and during the TEOS addition, a large variety of deformed fibers with different sizes was obtained (Figure 2.15).

2.3 Characterization

Ordered mesoporous silica materials are generally characterized by microscopy, gas sorption and X-ray diffraction (XRD). Particle morphology, shape and size, are evaluated using scanning or transmission electron microscopy while the textural properties are studied by using gas sorption (pore size, pore volume, surface area, etc.), as well as XRD (framework structure and pore to pore distance).

2.3.1 Gas sorption

Mesoporous materials are characterized by high pore volume, high surface area and a pore size in the range from 2 to 50 nm (Chapter 2.2.1). Gas sorption analysis is used to evaluate these parameters. This technique is based on the physisorption of a gas on a solid surface at constant temperature. The process consists of two general steps, namely adsorption and desorption. During the adsorption the gas condenses on a solid surface forming a monolayer and subsequently multilayers. Capillary condensation occurs, filling the free spaces in the pores when the film reaches the critical thickness. Desorption is the reverse process and represents the gas evaporation. The data obtained are expressed with an isotherm. The adsorption isotherm describes quantitatively the adsorption of a gas by a porous material at a fixed temperature in function of the partial pressure. Nitrogen at 77 K and argon at 87 K are the most commonly used adsorptive gases for mesoporous materials. [41,42] Porosity and the interactions between material (adsorbent), gas (adsorptive) and the liquid like state after adsorption (adsorbate) give different characteristic isotherms that have been classified by IUPAC as shown in Figure 2.16. There are six types of isotherms that describe microporous materials (type I(a) and type I(b)), non-porous or macroporous materials (type II), materials with weak adsorbent/adsorbate interaction (type III and type V), mesoporous materials (type IV(a) and type IV (b)) and layer-by-layer adsorption (type VI).

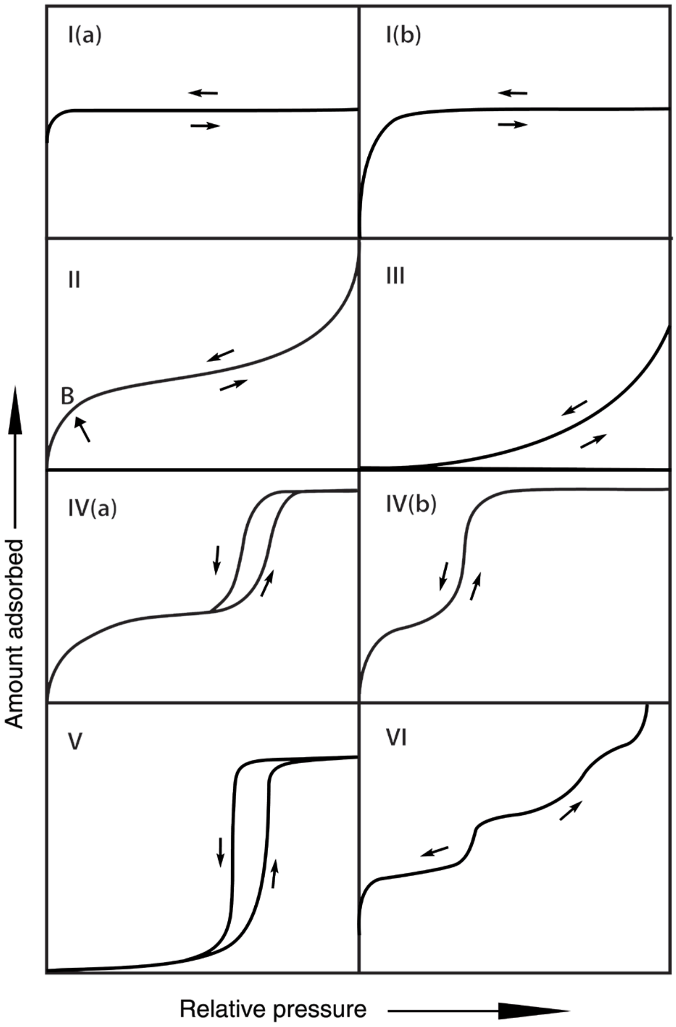

Figure 2.16 IUPAC classification of physisorption isotherms.[43]

ASNCs show generally type IV(b) isotherms (Figure 2.17, panel A) but increasing the pore size (extracted samples) or changing the adsorptive gas from nitrogen to argon, type IV(a) isotherms are also obtained (Figure 2.17, panel B).

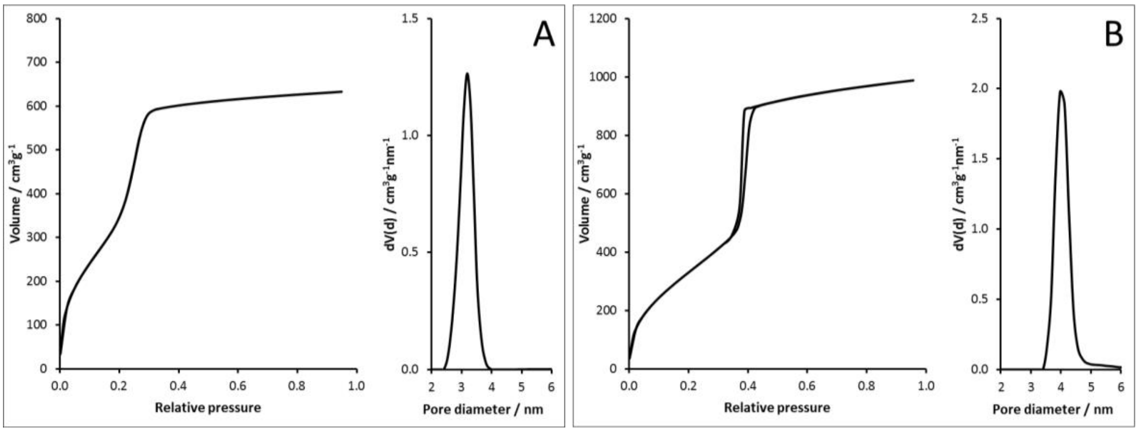

Figure 2.17 Argon sorption isotherms and respective pore size distributions of ASNCs: calcined (panel A) and extracted (panel B).

The loop between adsorption and desorption isotherm provides information about pore size distribution, pore geometry and pore connectivity.[44,45] Figure 2.18 shows the IUPAC classification of the hysteresis loops.

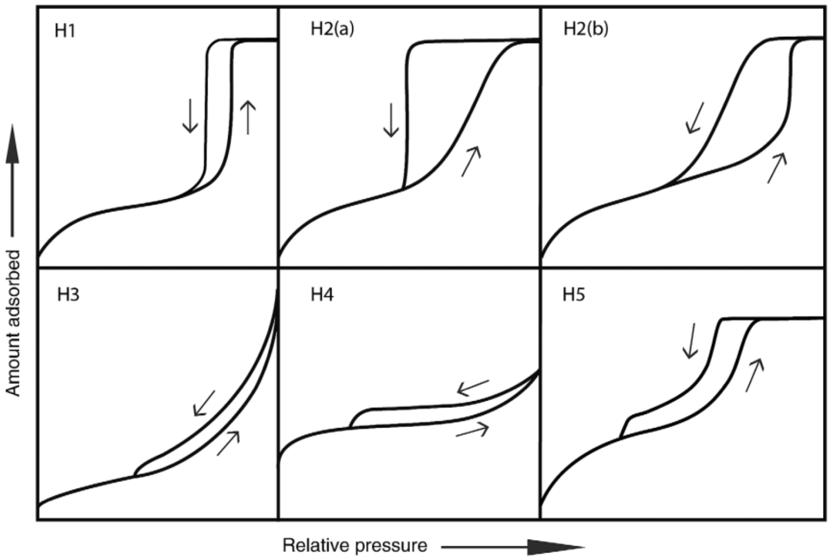

Figure 2.18 IUPAC classification of hysteresis loops.[43]

Hysteresis type H1 describes systems with narrow cylindrical pore channels such as ASNCs with large pores or SBA-15 samples. H2 hysteresis loops are characteristic for materials without a well-defined distribution of the pore size or with a bottleneck pore shape (SBA-16 samples). The interconnections between pores with different sizes cause bottleneck constrictions. Cavitation (type H2(a)) occurs when the neck size is below a critical diameter.

Pore blocking takes place when the pore neck size is above a critical diameter. The critical diameter depends on the adsorptive, temperature and pore structure. Materials that give H3 and H4 hysteresis have slit-shaped pores. H5 hysteresis is an unusual combination of H1 and H2 loops. The physical properties are obtained from the isotherm. Specific mathematical approaches give information about pore size distribution (PSD), pore volume (V_{tot}), surface area (S_a), external surface area (S_{ext}) and meso- micropore volume (V_m). With the method proposed by Brunauer-Emmett-Teller (BET) it is possible to calculate the surface area in the range of partial pressure from 0.05 to 0.3 (using nitrogen sorption). The total pore volume is generally measured at a partial pressure at or above 0.95 and represents the total amount of liquid volume that has been adsorbed and confined in the pores. To determine the PSD, various methods are available. Generally the BJH (Barrett, Joyner and Halenda) method works well with large mesopores but not with small pore size materials.[46,47] BJH does not consider the true statistical thickness, the adsorption potential and the surface tension of the adsorbed films. Two different methods were proposed addressing these problems: non-local density functional theory (NLDFT) and Grand Canonical Monte-Carlo simulations (GCMC). NLDFT considers a combination of material, gas and pore shape at a specific temperature. The pore size distribution of ASNCs is calculated from the adsorption isotherm using the NLDFT kennel for silica with cylindrical pores.

2.3.2 X-ray diffraction

X-ray diffraction (XRD) is used to determine the framework structure of ordered mesoporous materials.[10] As described in Chapter 2.2.3, there are different types of geometries and the diffractogram provides information about the constructive interferences showing peaks centered at specific angles.

By measuring these angles and applying Bragg's law (Eq. 2.4) the diffraction grating can be determined:

$$2d\cdot\sin\theta = n\cdot\lambda \qquad (2.4)$$

The wavelength λ depends on the source (Cu $K\alpha_1$ = 0.154056 nm), n represents the order of diffraction (in our case n is equal to 1), θ is the glancing angle and d (or *d-spacing*) is the repeating distance between reflecting planes. The lattice planes are labelled by assigning three integer numbers *h*, *k* and *l* (known as Miller indices) and indicated as d_{hkl}. The relation between *d* and the indices depends on the crystal system as reported in Figure 2.19.

$$\text{Cubic:} \qquad \frac{1}{d_{hkl}^2} = \frac{\left(h^2 + k^2 + l^2\right)}{a^2}$$

$$\text{Tetragonal:} \qquad \frac{1}{d_{hkl}^2} = \frac{\left(h^2 + k^2\right)}{a^2} + \frac{l^2}{c^2}$$

$$\text{Orthorombic:} \qquad \frac{1}{d_{hkl}^2} = \frac{h^2}{a^2} + \frac{k^2}{b^2} + \frac{l^2}{c^2}$$

$$\text{Hexagonal:} \qquad \frac{1}{d_{hkl}^2} = \frac{4}{3}\frac{h^2 + hk + k^2}{a^2} + \frac{l^2}{c^2}$$

Figure 2.19 Formula to calculate the interplanar spacings (d_{hkl}) for a family of planes with Miller indices hkl in a unit cell of parameters a, b, c.

The position of the reflections is defined by the symmetry and the unit cell parameter of the investigated material. Furthermore, information about the size and symmetry of the lattice can be obtained from the diffractogram. In analogy with liquid crystal phases, mesostructured materials exhibit hexagonal, lamellar, or cubic phases.

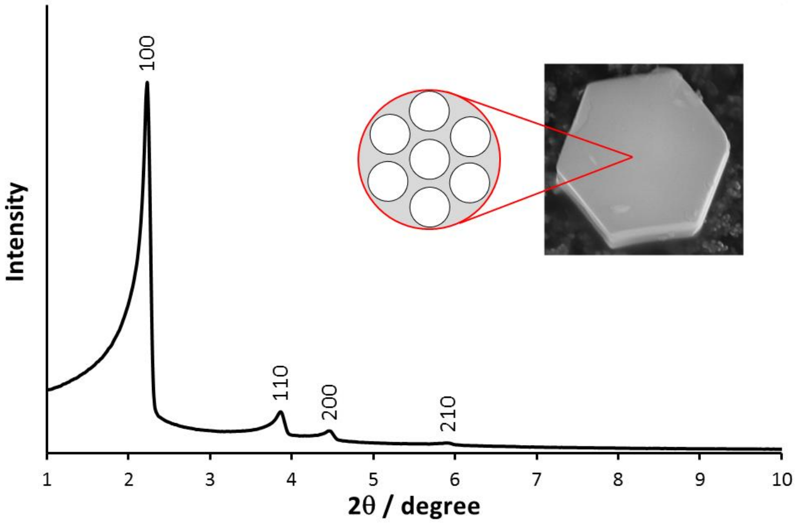

Figure 2.20 Typical X-ray diffraction pattern of ASNCs particles (space group P6mm).

Well-ordered ASNCs and MCM-41 type materials, show 4 or 5 reflections that are indexed as (100), (110), (200), (210) and (300).[10,37] These reflections correspond to the hexagonal space group *P6mm* (Figure 2.20). In the hexagonal lattice, the repeat distance a_0 (pore to pore distance) is calculated from the d_{100} value according to equation 2.5.

$$a_0 = 2 * d_{100} / \sqrt{3} \tag{2.5}$$

This parameter gives an estimation of the mesoporous framework wall thickness by subtracting from a_0 the pore diameter obtained by gas sorption. The characteristic peaks of the material are often in the range of the primary beam making the interpretation of the diffractogram difficult. The 2θ angle decreases when the distance between the planes increases (Eq.2.4). Mesoporous materials with large pore diameters or thick pore walls, such as SBA-15 and SBA-16, therefore give signals at low angles.[48] Small-angle X-ray scattering (SAXS) is used to obtain a clear pattern for samples with large plane distances (Figure 2.21)

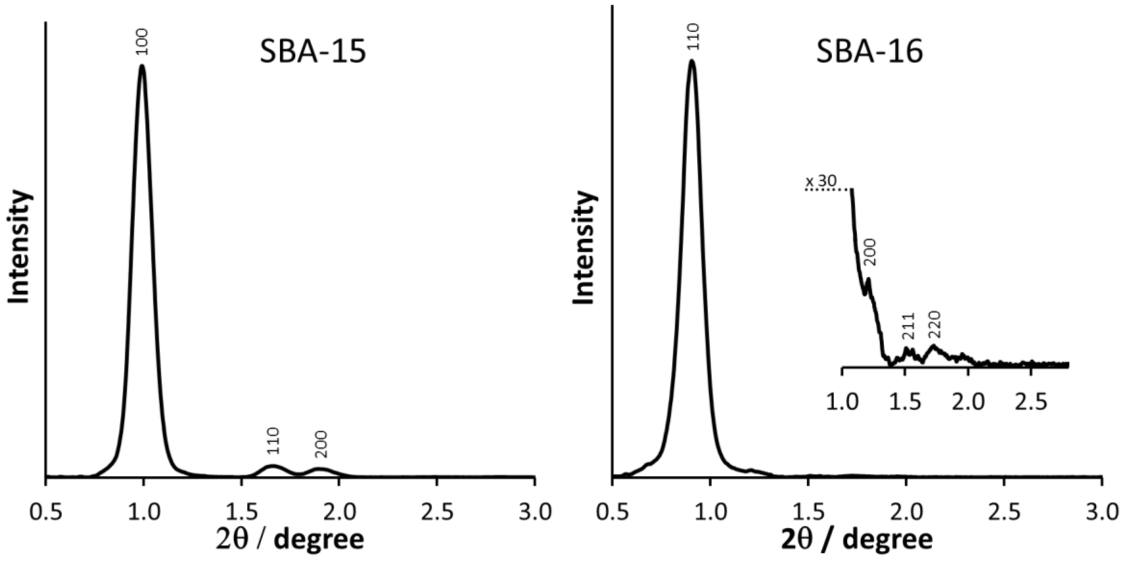

Figure 2.21 SAXS of SBA-15 (space group P6mm) and of SBA-16 (space group Im$\bar{3}$m).

2.4 References

1. L. C. Klein and G. J. Garvey, J. Non-Cryst. Solids, 1980, 38, 45-50.
2. C. J. Brinker, K. D. Keefer, D.W. Shaefer, R. A. Assink, B.D. Kay and C. S. Ashley, J. Non-Cryst. Solids, 1984, 63, 45-59.
3. D.A.H. Hanaor, I. Chironi,I. Karatchevtseva, G. Triani and C. C. Sorrell, Adv. Appl. Ceram., 2012, 111, 149-158.
4. W. Stöber, A. Fink and E. Bohn, J. Colloid Interface Sci., 1968,26, 62-69.
5. C. J. Brinker, J. Non-Cryst. Solids, 1988, 100, 31-50.
6. E. J. A. Pope and J. D. Mackanzie, J. Non-Cryst. Solids, 1986, 87, 185-198.
7. J. E. Lofgreen and G. A. Ozin, Chem. Soc. Rev., 2014, 43, 911-933.
8. P. Innocenzi, *The Sol Gel Transition*, ed. SpringerBriefs in Materials, Springer, 2016.
9. Z. A. Alothman, Materials, 2012, 5, 2874-2902.
10. J.S. Beck, J.C. Vartuli, W.J. Roth, M.E. Leonowicz, C.T. Kresge, K.D. Schmitt, C.T.-W. Chu, D.H. Olson, E.W. Sheppard, S.B. McCullen, J.B. Higgins and J.L. Schlenker, J. Am. Chem. Soc., 1992, 114, 10834-10843.
11. K. S. W. Sing, D.H. Everett, R.A.W. Haul, L. Mouscou, R.A. Pierotti, J. Rouquerol and T. Siemieniewska, Pure & Appl. Chem., 1985, 57, 603-619.
12. C.T. Kresge, M.E. Leonowicz, W.J. Roth, J.C. Vartuli and J.S. Beck, Nature, 1992, 359, 710-712.
13. Q. S. Huo, D. I. Margolese, U. Cielsa and G.D. Stucky, Nature, 1994, 368, 317-321.
14. A. Firouzi, D. Kumar, L.M. Bull, T. Besier, P. Sieger, Q. Huo, S.A. Walker, J.A. Zasadzinski, C. Glinka, J. Nicol, D. Margolese, G.D. Stucky and B.F. Chmelka, Science, 1995, 267, 1138-1143.
15. F. Schüth, U. Ciesla, S. Schacht, M. Thieme, Q. Huo and G. Stucky, Mater. Res. Bull., 1999, 34, 483-494
16. J. Blanchard, P. Trens, M. Hudson and F. Schüth, Microporous Mesoporous Mater., 2000, 39, 163-170.
17. P.T. Tanev and T.J. Pinnavaia, Science, 1995, 267, 865-867.
18. C.-Y. Chen, H.-X. Li and M.E. Davis, Microporous Mater., 1993, 2, 17-26.
19. S. Hitz and R. Prins, J. Catal., 1997, 168, 194-206.
20. F. Marlow, D. Demuth, G. Stucky and F. Schueth, J. Phys. Chem., 1995, 99, 1306-1310.

21. F. Hoffmann, M. Cornelius, J. Morell and M. Fröba, Angew. Chem., Int. Ed., 2006, 45, 3216-3251.
22. P. Innocenzi, L. Malfatti, T. Kidchob and P. Falcaro, Chem. Mater., 2009, 21, 2555-2564.
23. D. S. Shephard, W. Zhou, T. Maschmeyer, J. M. Matters, C. L. Roper, S. Parsons, B. F. G. Johnson and M. J. Duer, Angew. Chem., Int. Ed., 1998, 37, 2719-2723.
24. K. Cheng and C. C. Landry, J. Am. Chem. Soc., 2007, 129, 9674-9685.
25. N. Gartmann and D. Brühwiler, Angew. Chem., Int. Ed., 2009, 48, 6354-6356.
26. Y. Huang, S. Xu and V. S.-Y. Lin, Angew. Chem., Int. Ed., 2011, 50, 661-664.
27. J. D. Webb, T. Seki, J. F. Goldston, M. Pruski and C. M. Crudden, Microporous Mesoporous Mater., 2015, 203, 123-131.
28. S. Huh, J. W. Wiench, J.-C. Yoo, M. Pruski and V. S.-Y. Lin, Chem. Mater., 2003, 15, 4247-4256.
29. S. Sadasivan, D. Khushalani and S. Mann, J. Mater. Chem., 2003, 13, 1023-1029.
30. J. L. Blin, C. Gérardin, L. Rodehüser, C. Selve and M. J. Stébé, Chem. Mater., 2004, 16, 5071-5080.
31. C. Yang, Y. Wang, B. Zibrowius and F. Schüth, Phys. Chem. Chem. Phys., 2004, 6, 2461-2467.
32. R. P. Hodgkins, A. E. Garcia-Bennett and P. A. Wright, Microporous Mesoporous Mater., 2005, 79, 241-252.
33. K. Möller, J. Kobler and T. Bein, J. Mater. Chem., 2007, 17, 624-631.
34. F. O. M. Gaslain, C. Delacôte, A. Walcarius and B. Lebeau, J. Sol–Gel Sci. Technol., 2009, 49, 112-124.
35. N. Gartmann, C. Schütze, H. Ritter and D. Brühwiler, J. Phys. Chem. Lett., 2010, 1, 379-382.
36. N. Gartmann and D. Brühwiler, Materials, 2011, 4, 1096-1103.
37. N. Zucchetto and D. Brühwiler, Dalton Trans., 2016, 45, 14363-14369.
38. A. Devaux, G. Calzaferri, P. Belser, P. Cao, D. Brühwiler and A. Kunzmann, Chem. Mater., 2014, 26, 6878-6885.
39. G. A. Ozin, C. T. Kresge and H. Yang, Stud. Surf. Sci. Catal., 1998, 117, 119-127.
40. H. Yang, N. Coombs and G. A. Ozin, Nature, 1997, 386, 692-695.
41. Y. Grillet, J. M. Cases, M. Francois and J. Rouquerol, Clays Clay Miner., 1988, 36, 233-242.

42. D. A. Payne, K. S. W. Sing and D. H. Turk, J. Colloid Interface Sci., 1973, 43, 287-293.
43. M. Thommes, K. Kaneko, A. V. Neimark, J. P. Olivier, F. Rodriguez-Reinoso, J. Rouquerol and K. S. W. Sing, Pure Appl. Chem., 2015, 87 , 1051-1069.
44. P. A. Monson, Langmuir, 2008, 24, 12295-12302.
45. M. Thommes, B. Smarsly, M. Groenewolt, P. I. Ravikovitch, and A. V. Neimark, Langmuir, 2006, 22, 756-764.
46. D. P. Serrano, J. Aguado, G. Morales, J. M. Rodriguez, A. Peral, M. Thommes, J. D. Epping and B. F. Chmelka, Chem. Mater., 2009, 21, 641-654.
47. A. V. Neimark and P. I. Ravikovitch, Microporous Mesoporous Mater., 2001, 44, 697-707.
48. G. Ferreira Andrade, D. C. Ferreira Soares, R. K. De Sousa Almeida and E. M. Barros Sousa, J. Nanomat., 2012, 2012, 1-10.

3. TUNING THE ASPECT RATIO OF ARRAYS OF SILICA NANOCHANNELS

The hexagonal prismatic shape of ASNCs reflects the ordered growth of the framework. As described in Chapter 2.2.5, the mesochannel disposition is along the length of the particles creating a characteristic one-dimensional channel system, where the channel entrances are located on the hexagonal faces. The original synthesis was conducted at low pH (hydrochloric acid) and with CTAC as templating agent. The reaction conditions influence dramatically the particle shape; when changing the synthesis parameters, the particles lose their characteristic morphology. Experiments were conducted in order to improve the reproducibility and to obtain particles with different aspect ratio.[1]

3.1 Alternative synthesis

3.1.1 Effect of CTAB

When the surfactant (CTAC) is replaced with the more common CTAB, Br^- is introduced as an additional counter-ion. This has a noticeable effect on the particle size and morphology as shown in Figure 3.1. The synthesis is conducted in hydrochloric acid and the concentration of Cl^- anions is around 50 times higher than the concentration of Br^-. The observation of an apparently strong interaction between Br^- and micelles is in agreement with previous studies that showed that Cl^- is inefficient at replacing Br^- from CTAB micelles.[2]

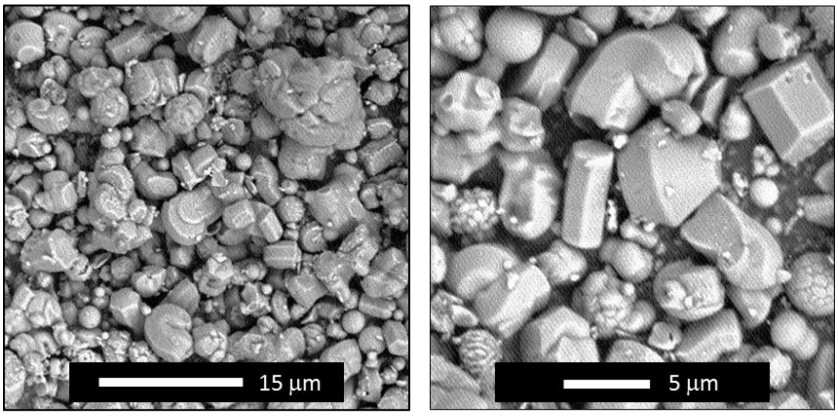

Figure 3.1 SEM image of ASNCs prepared with CTAB instead of CTAC. The presence of Br^- ions led to deformed hexagonal rods.

The synthesis with CTAB yields a large fraction of deformed hexagonal particles. Considering the placement of Cl^- and Br^- in the anionic lyotropic series observed for CTAB,[3] we can expect that Br^- is more effective at reducing the micellar charge, thus causing the formation of long rod-shaped micelles. Ultimately this leads to the generation of fiber-shaped silica particles.[4] The complete substitution of Cl^- anions with Br^- anions (HBr instead of HCl) does not yield ASNCs.

3.1.2 Salt effects

The micellar charge is modified by the counter-ion. The lyotropic crystal formation and the subsequent silica growth are therefore influenced by the anion used. Potassium salts were used during the ASNCs synthesis with CTAB to verify the influence of anions on the particle shape (Figure 3.2). It is interesting to note that when increasing the concentration of Br^- or adding NO_3^- (both anions have strong interactions with micelles),[3] the final product results to be without a specific shape.

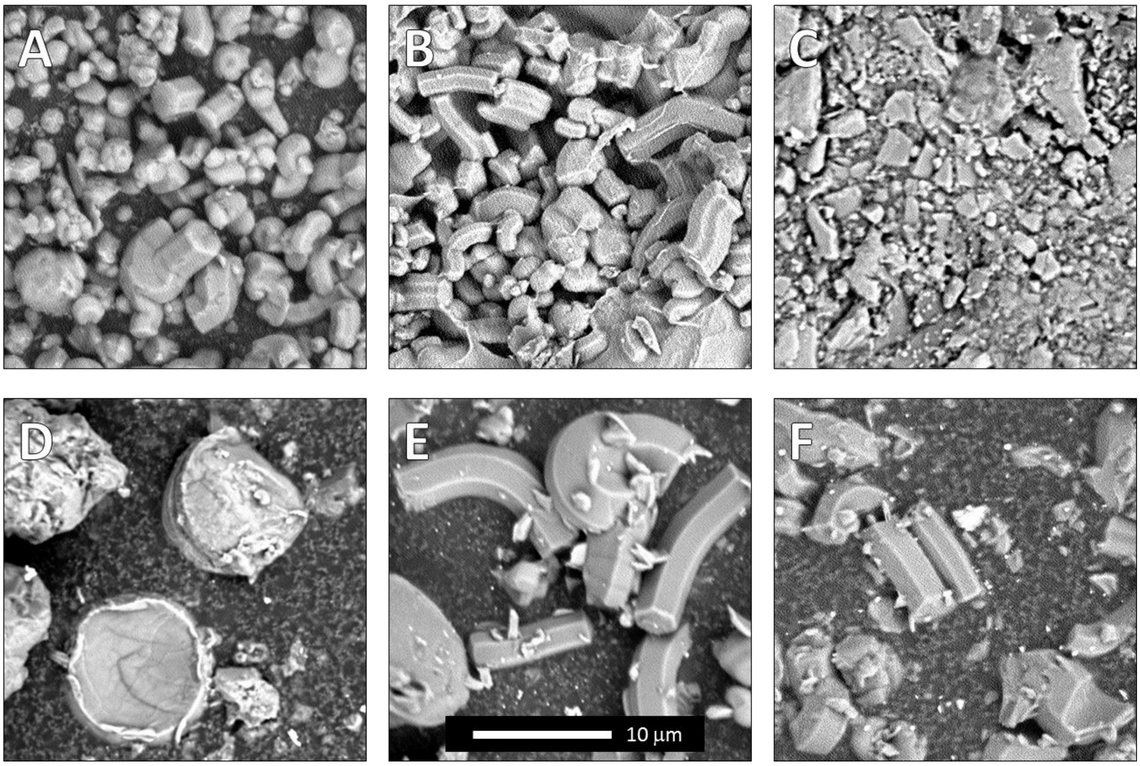

Figure 3.2 SEM images illustrating the counter-ion effect on the particle shape. The synthesis was performed without salt (panel A) and with the addition of KCl (panel B), KBr (panel C), KNO_3 (panel D), K_2SO_4 (panel E) and K_2HPO_4 (panel F). Rod-like shape was obtained with KCl, K_2SO_4, K_2HPO_4 and without salt. Instead, irregular and discoidal particles were obtained with KBr and with KNO_3, respectively.

The rod-like particles obtained by adding KCl have been the starting point for the alternative syntheses with CTAB. Focusing on the concentration of salt and SDA, ASNCs with regular hexagonal prismatic shape were obtained (Figure 3.3).

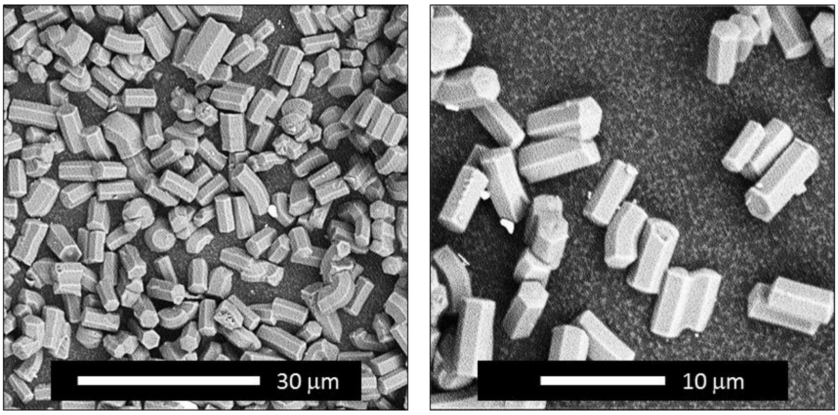

Figure 3.3 ASNCs synthesized with CTAB and KCl.

The product quality of the CTAB templated synthesis in terms of uniform particle size and shape can be considerably improved by the addition of KCl, achieving an aspect ratio of 1.8 (length/diameter). As in the first synthesis with CTAB without salt (Figure 3.1), the mixture contains only two counter-ions and the concentration of Cl^- is still higher than Br^-. Apparently the K^+ cations play an important role during the synthesis. In order to obtain more information, further syntheses with different salts were conducted and the SEM images are reported in Figure 3.4. The addition of chloride salts (KCl, NaCl and LiCl) improves the yield in terms of a regular rod-like shape. Bromide and nitrate salts led to shapeless particles, confirming the strong effect of these two anions.

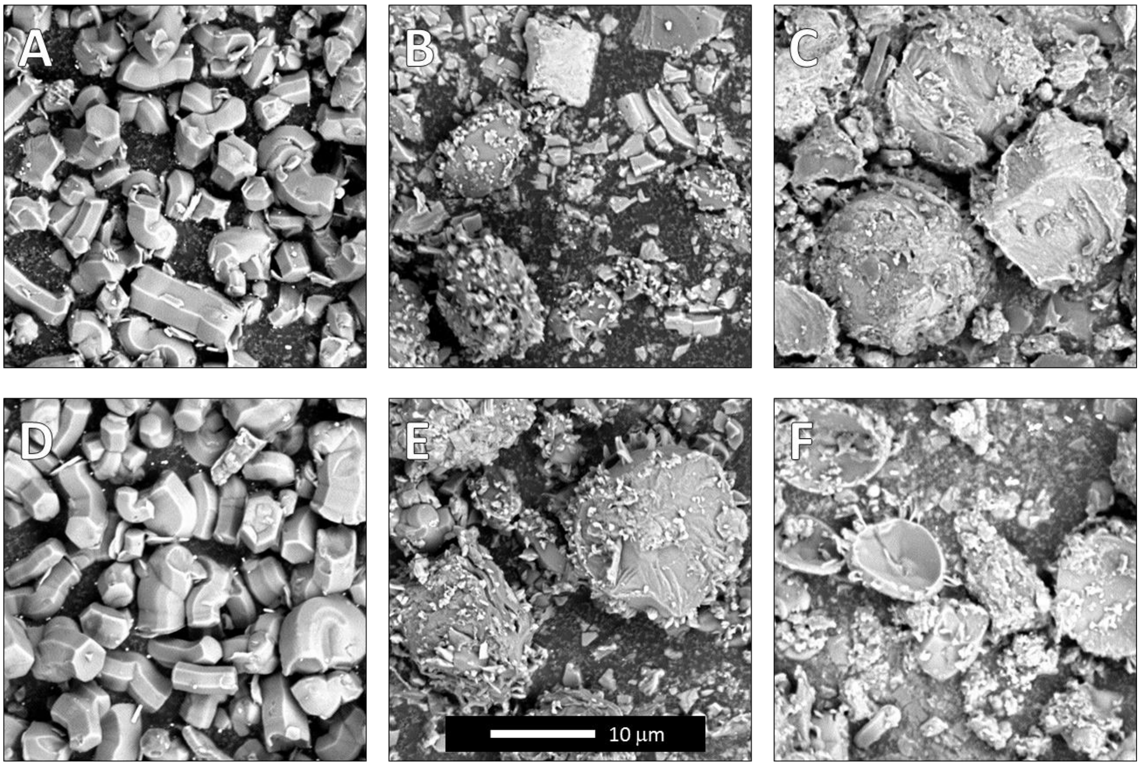

Figure 3.4 SEM images illustrating the co-ion effect. The synthesis was performed with NaCl (panel A), NaBr (panel B), $NaNO_3$ (panel C), LiCl (panel D), LiBr (panel E) and $LiNO_3$ (panel F). A rod-like shape was obtained for chlorides while irregular particles and discoids were obtained with bromide and nitrate salts, respectively.

These results show clearly the effects of the counter-ions but they are not sufficient to explain the co-ion effect. Interesting results were obtained using calcium chloride as shown in Figure 3.5.

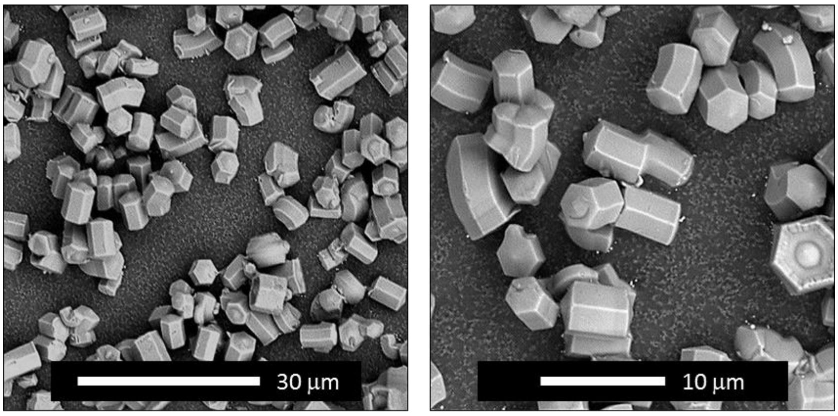

Figure 3.5 ASNCs synthesized with CTAB and $CaCl_2$.

The particles obtained after optimizing the synthesis parameters (CTAB and $CaCl_2$ concentration) show a regular hexagonal prismatic shape with an aspect ratio of 1.4.

3.1.3 Comparison between syntheses with KCl and $CaCl_2$

Unlike the counter-ions, co-ions have the same charge as the surfactant molecules. The effect of co-ions on the micelles is therefore expected to be less pronounced. However, we observed a distinct influence of the co-ions on the ASNCs particle size and porosity. The addition of KCl and $CaCl_2$ improves the uniformity of the particle size and shape. In these syntheses, the Cl^-/Br^- ratio is only slightly increased compared to the pathway without salt addition.

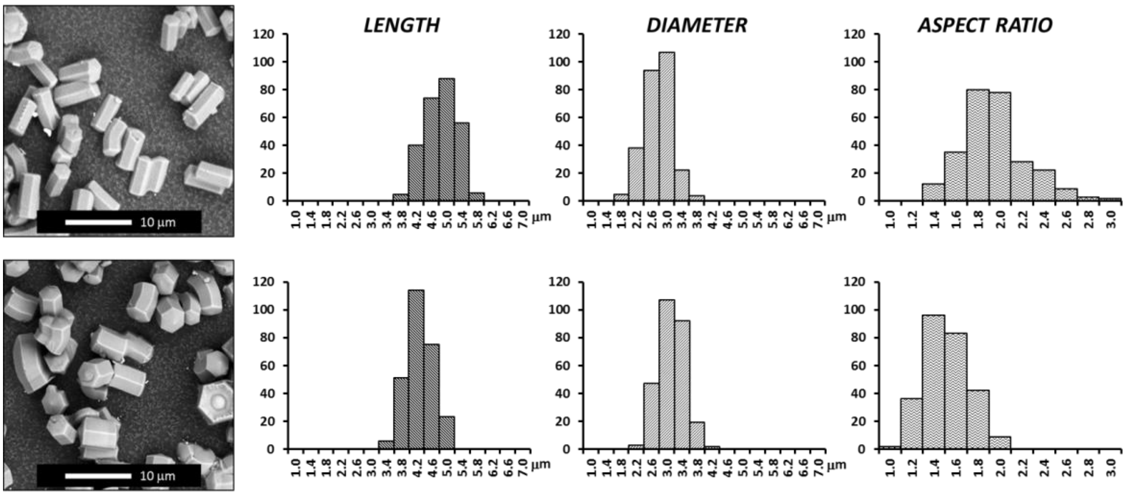

Figure 3.6 SEM images of ASNCs prepared with CTAB/KCl (top) and CTAB/$CaCl_2$ (bottom) and respective distributions of the particle lengths, diameters and aspect ratios.

ASNCs prepared with CTAB/KCl are characterized by an average length similar to the particles obtained with the classical CTAC synthesis (4.7 and 4.8 nm, respectively). Shorter particles are obtained when using CTAB/$CaCl_2$ (4.1 nm). In both cases, CTAB/KCl and CTAB/$CaCl_2$, particles with increased diameter (2.6 and 2.9 nm, respectively) are obtained compared to the classical CTAC pathway (2.0 nm). As a consequence, the aspect ratio decreases from 2.4 (CTAC) to 1.8 (CTAB/KCl) and 1.4 (CTAB/$CaCl_2$). The particle dimensions are summarized in Table 3.1 and representative SEM images and dimension distributions are shown in Figure 3.6.

Table 3.1. ASNCs particle dimensions.

	Length / µm	Diameter / µm	Aspect ratio
CTAC	4.8 ± 0.5	2.0 ± 0.3	2.4 ± 0.4
CTAB/KCl	4.7 ± 0.4	2.6 ± 0.4	1.8 ± 0.3
CTAB/CaCl$_2$	4.1 ± 0.4	2.9 ± 0.4	1.4 ± 0.3

Nitrogen sorption data, the isotherms and the corresponding pore size distributions of ASNCs synthesized with CTAB, CTAB/KCl or CTAB/CaCl$_2$ are presented in Table 3.2 and Figure 3.7.

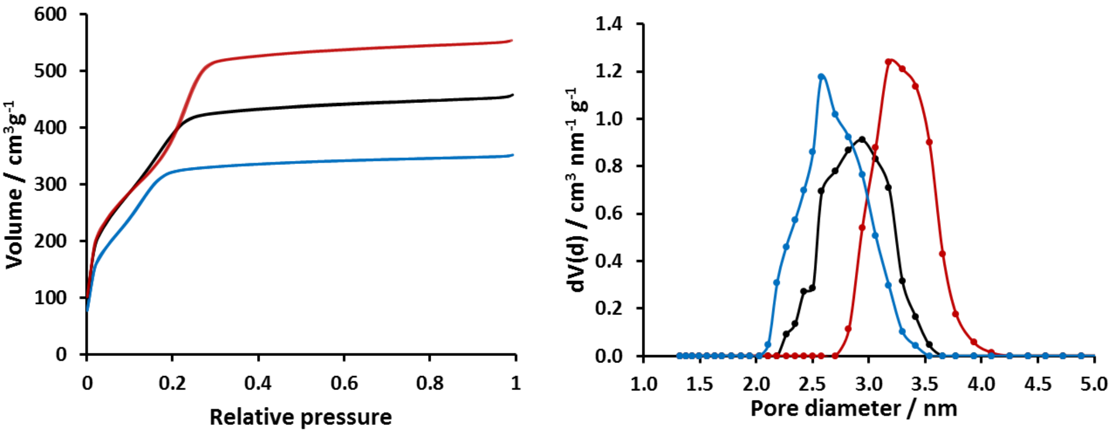

Figure 3.7 Left: nitrogen sorption isotherms of ASNCs synthesized with CTAB (black), CTAB/KCl (blue) and CTAB/CaCl$_2$ (red). Right: respective pore size distributions.

The presence of K$^+$ in the synthesis mixture leads to a reduced pore diameter (d$_{DFT}$) when compared to the samples prepared with CTAC or CTAB only, whereas Ca^{2+} has the opposite effect.

Table 3.2. Nitrogen adsorption data.

	V$_{tot}$ / cm^{3}g^{-1}	V$_p$ / cm^{3}g^{-1}	d$_{DFT}$ / nm
CTAC	0.60	0.56	2.94
CTAB	0.71	0.64	2.94
CTAB/KCl	0.54	0.52	2.58
CTAB/CaCl$_2$	0.86	0.78	3.18

While the influence of the counter-ion on the aggregation behavior of surfactants is generally well understood and can be interpreted in terms of polarizability and hydration, the role of co-ions is less clear.[2,3] Previous studies indicate that co-ions have only a minor effect on the sphere-rod transition, but that the sizes of rod-like micelles can differ considerably depending on the type of co-ion. A comparison between the CTAB/KCl and the CTAB/NaCl systems revealed that K^+ has a more pronounced effect on the micelles, which was attributed to the larger extent of penetration of K^+ into the micellar corona (Figure 3.8).[5]

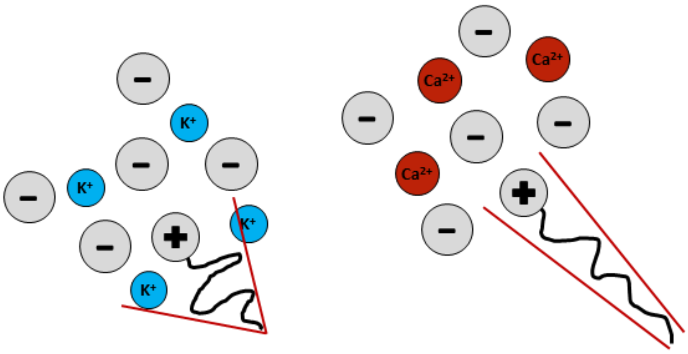

Figure 3.8 Different effects on the micelle. K^+ shows a larger extent of penetration compared to Ca^{2+}.

In the lyotropic series observed for cations with CTAB, Ca^{2+} is placed much higher than K^+, as expected from the charge and hydrated radius.[3] The investigation of the effect of co-ions on sodium dodecyl sulfate (SDS) micelles showed that the molecular mass of the rod-like micelles changes according to the lyotropic series of the co-ions. The difference in micelle size was attributed to the effect of co-ions on the hydrophobic interaction in the micelle formation and to the alteration of the hydrogen-bonded structure of water. We can therefore expect an increase of micelle size when using Ca^{2+} instead of K^+ in combination with CTAB. Powder XRD patterns of ASNCs prepared with CTAB/KCl and CTAB/$CaCl_2$ are reported in Figure 3.9.

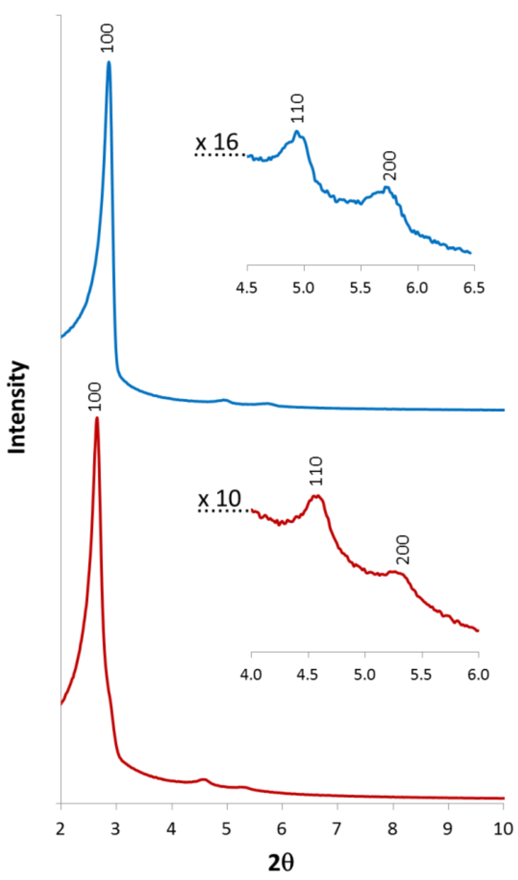

Figure 3.9 XRD patterns of CTAB/KCl (top) and CTAB/$CaCl_2$ (bottom) samples. The samples are offset for clarity.

The samples show three peaks that can be assigned to the (100), (110), and (200) reflexes of the 2D hexagonal space group *P6mm* (Figure 3.9). This is a feature that is considered typical for well-ordered MCM-41 type materials. Assuming hexagonal base surfaces with an average diameter D obtained from the SEM images, the number of channels per particle N_C can be estimated by applying equation 3.1.

$$N_C = 0.75 * (D / a_0)^2 \tag{3.1}$$

The repeat distance a_0 was calculated from the d_{100} value (according to equation 2.5, Chapter 2.3.2). The results of the calculations are summarized in Table 3.3. The larger particle diameter of the ASNCs synthesized with CTAB/$CaCl_2$ can be interpreted as a direct consequence of the larger pore size, considering the comparable number of nanochannels per particle.

Table 3.3. Structural parameters obtained from XRD.

	a_0 / nm	d_{100} / nm	N_C
CTAB/KCl	3.57	3.09	397’806
CTAB/CaCl$_2$	3.85	3.33	425’536

3.2 Tuning of the aspect ratio

The preparation of ASNCs with CTAB/$CaCl_2$ yields particles with slightly shorter nanochannels, compared to the products of the classical synthesis pathway using CTAC. The aspect ratio of the particles is reduced from 2.4 to 1.4. The ability to adjust the length of well-defined nanochannels is considered relevant for the investigation of transport processes in nanoscale geometries.[6] Adjustment of the silane/surfactant ratio allows for tuning of the aspect ratio and of the nanochannel length over a wide range.

3.2.1 Silane/surfactant ratio

By varying the TEOS/CTAB (silane/surfactant) ratio, the nanochannel length (corresponding to the particle length) and the aspect ratio can be adjusted over a wide range, as shown in Figure 3.10.

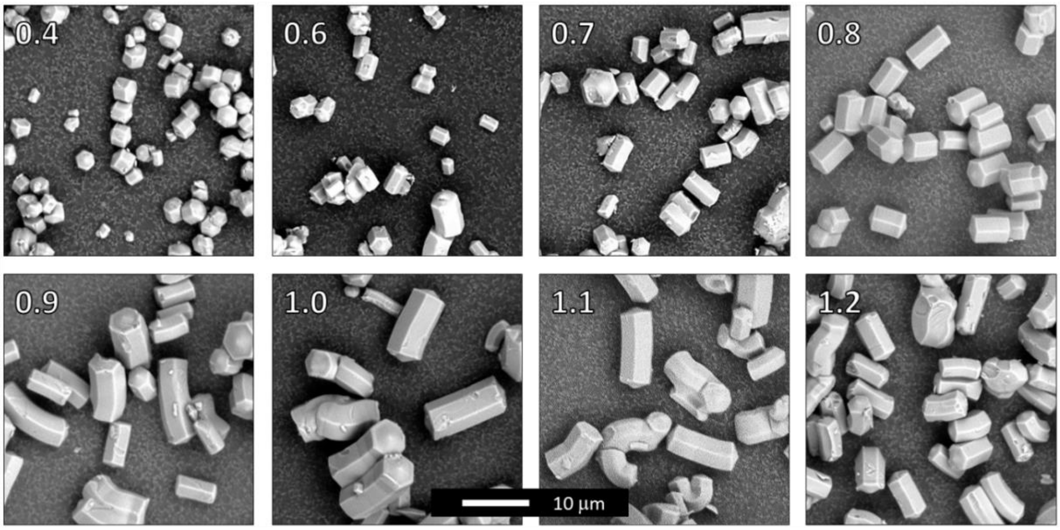

Figure 3.10 SEM images of ASNCs synthesized with CTAB/$CaCl_2$ and various TEOS/CTAB ratios (indicated by the number on the top left of each image).

The overall particle size (length and diameter) gradually increased with larger amount of TEOS. As can be seen from Figure 3.11, the amount of TEOS has a more pronounced effect on the particle length, indicating preferential end-on growth.

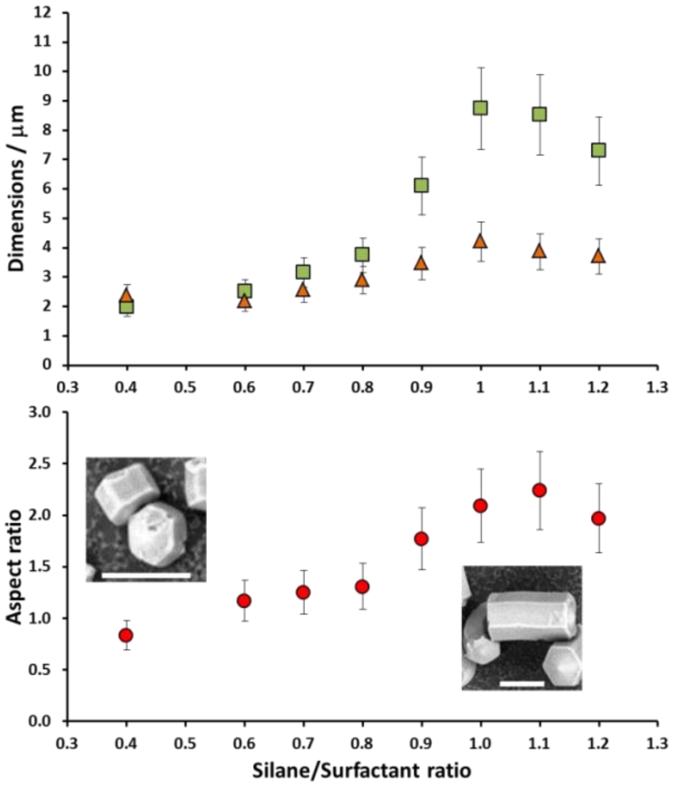

Figure 3.11 Top: length (green squares) and diameter (orange triangles) of ASNCs synthesized with CTAB/CaCl$_2$ in function of the silane/surfactant (TEOS/CTAB) ratio. Bottom: respective aspect ratios. The SEM images correspond to samples prepared with a silane/surfactant ratio of 0.4 (left image) and 1.0 (right image). The scale bars are 5 μm.

No further length or diameter increase was observed at TEOS/CTAB > 1. For small amounts of TEOS, the particle length decreased until it was short than the diameter, resulting in an aspect ratio of 0.8. Within the investigated TEOS/CTAB ratio range, no significant effect of the TEOS/CTAB ratio on the pore diameter of the resulting ASNCs was observed. This allows us to control the nanochannel length without affecting the nanochannel diameter. Further reduction of the amount of TEOS (leading to a TEOS/CTAB ratio below 0.4) produced particles with partial hexagonal platelet-type shape but an overall irregular morphology (Figure 3.12).

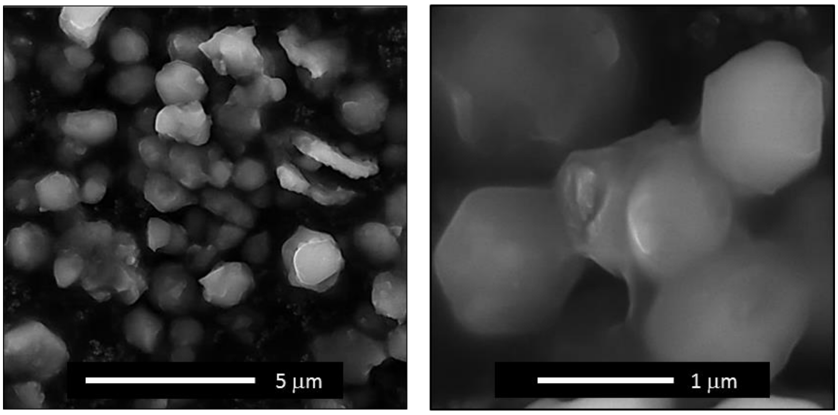

Figure 3.12 ASNCs particles synthesized with a silane/surfactant ratio of 0.2.

It was generally observed that increasing the TEOS/CTAB ratio produces a larger amount of curved ASNCs. This effect becomes noticeable only at silane/surfactant ratios larger than 0.8.

3.3 Pore size enlargement

The pore size adjustment is an attractive challenge, since it allows for adapting the properties of the host/support material according to the requirements of the application. The possibility to use surfactants with different chain lengths or swelling agents provides the basis for achieving this goal, as shown in Figure 3.13.[7]

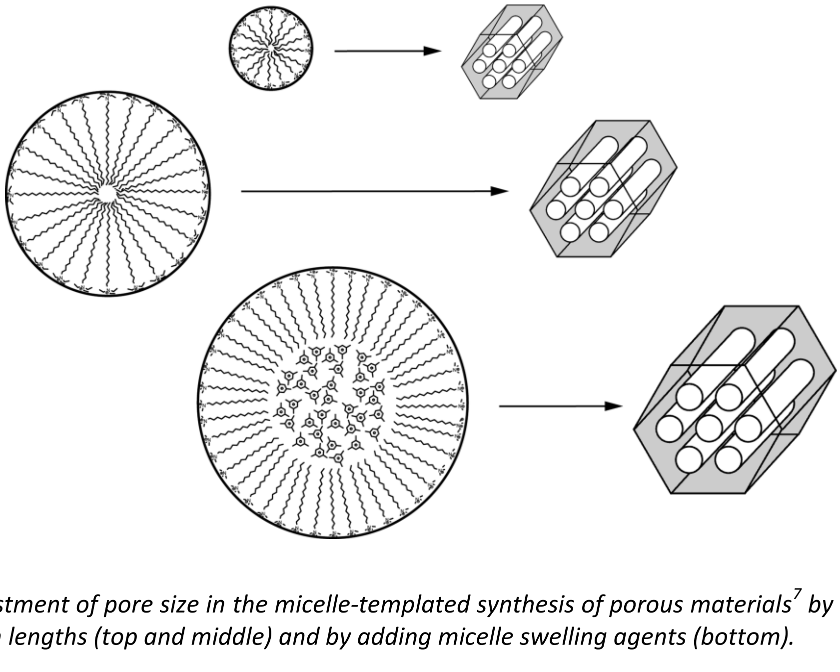

Figure 3.13 Adjustment of pore size in the micelle-templated synthesis of porous materials[7] by using surfactants of different chain lengths (top and middle) and by adding micelle swelling agents (bottom).

A variety of compounds was shown to act as micelle expanders, including benzene and its alkyl-substituted derivatives (most notably mesitylene or TMB), linear hydrocarbons, cyclic hydrocarbons and long-chain amines.[7] While micelle expanders increase the mesopore size and the volume of micelle-templated materials, their action typically results in a decrease of structural ordering or in the change of the structure type. Interesting results were obtained by adding TMB to the ASNCs synthesis. As expected, the particle shape changed from short rods to fibers and discoids when the quantity of swelling agents was increased (Figure 3.14).

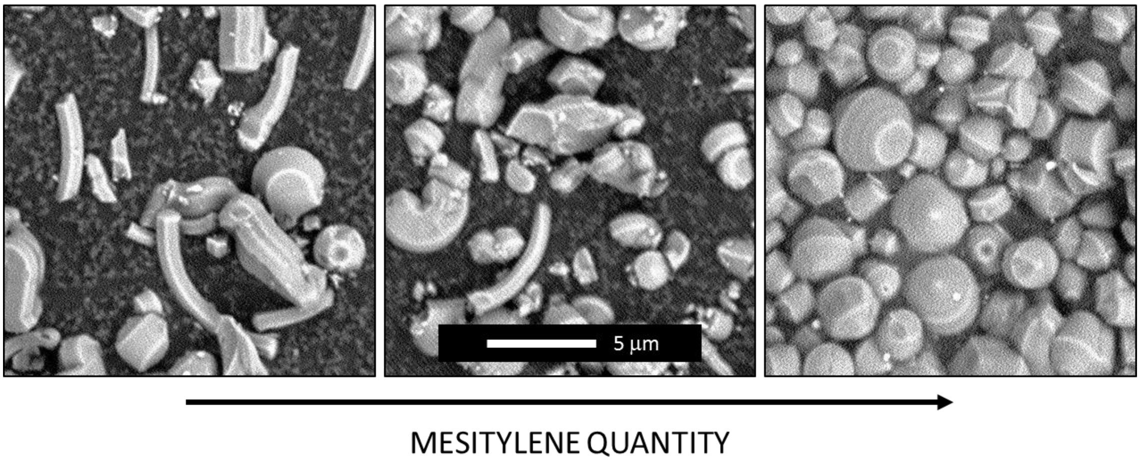

Figure 3.14. SEM images of ASNCs prepared with CTAB/mesitylene. By increasing the amount of swelling agent the shape changes from fibers to discoids.

The nitrogen adsorption analysis is reported in Figure 3.15. The pore size distribution shifts from 2.9 nm (CTAB) to 2.3 nm (CTAB/mesitylene) but broad peaks appear at 5 nm.

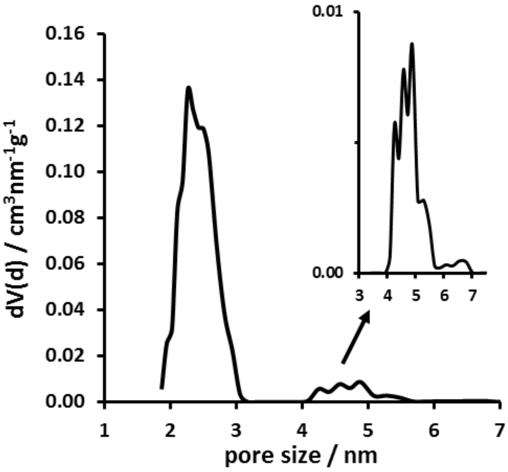

Figure 3.15 Pore size distribution (nitrogen sorption) of mesoporous silica prepared with CTAB/mesitylene.

3.5 Conclusion

The use of CTAB/KCl or CTAB/$CaCl_2$ in the synthesis of ASNCs yields products that are comparable in terms of porosity and particle morphology to the products obtained by the classical pathway with CTAC as structure-directing agent. The combination of co-ions with CTAB thereby improves the yield of regular hexagonal prismatic particles. Interestingly, the co-ions also affect the pore diameter. Compared to the pathway without salt addition, the presence of KCl in the synthesis mixture leads to a reduced pore diameter, whereas $CaCl_2$ has the opposite effect. Adjusting the TEOS/CTAB ratio in the CTAB/$CaCl_2$ synthesis allows control of the length of the ASNCs and therefore of the nanochannel length. As the effect of the TEOS/CTAB ratio on the particle diameter is less pronounced, ASNCs of various aspect ratios can be prepared, with a minimum value of 0.8. The swelling agents partially modify the pore size distribution, but they affect dramatically the particle morphology. The option to prepare ASNCs with various channel lengths will open new possibilities for the investigation of transport processes in porous media.

3.4 Experimental

3.4.1 Materials

Hexadecyltrimethylammonium bromide (CTAB, BioUltra, ≥99.0%), KCl (≥99.0%), $CaCl_2$ (≥97.0%), concentrated hydrochloric acid (puriss. p.a., ≥32%), and tetraethoxysilane (TEOS, 99.999%) were obtained from Sigma-Aldrich. Hexadecyltrimethylammonium chloride (CTAC, 99%) was obtained from Acros. All chemicals were used as received.

3.4.2 Synthesis of ASNCs

ASNCs were synthesized by the classical route (with CTAC) following a previously published procedure.[8] For a typical alternative synthesis with CTAB instead of CTAC, CTAB (4.0 g, 11 mmol) was dissolved in a mixture of doubly distilled H_2O (76 mL, 4.2 mol) and concentrated hydrochloric acid (≥32%, 60 mL, 0.62 mol) by stirring for 15 min in a polypropylene beaker. The solution was subsequently cooled to 0 °C in an ice bath for

15 min under quiescent conditions, followed by the slow addition of cold TEOS (4 °C, 2.0 mL, 9 mmol) and further stirring for 30 s. The resulting mixture was kept at 0 °C under quiescent conditions for 4 h. The product was collected by filtration and washed with H_2O (250 mL). Additional syntheses were conducted with the addition of KCl and $CaCl_2$. An amount of 3.36 g (45 mmol) of KCl or 1.50 g (13.5 mmol) of $CaCl_2$ was found to give the best products in terms of regular hexagonal prismatic particle morphology.

Syntheses with different salts (KBr, KNO_3, K_2SO_4, K_2HPO_4, NaCl, NaBr, $NaNO_3$, LiCl, LiBr and $LiNO_3$) were performed using an amount in grams corresponding to 45 mmol.

Syntheses with different TEOS/CTAB ratios were performed by the above procedure using a constant amount of CTAB and changing the amount of TEOS. After the dissolution of CTAB and $CaCl_2$ (stirring for 15 min), the solution was cooled in an ice bath for 30 min under quiescent conditions and the respective amount of cold TEOS was added under stirring (for 30 s). The mixture was left at 0 °C for at least 90 min under quiescent conditions.

For all materials, the structure-directing agent was removed by first heating at 300 °C for 2 h and subsequent calcination in air at 550 °C for 12 h. Heating rates of 2 °C min^{-1} were applied.

3.4.3 Characterization

Scanning electron microscopy (SEM) images were obtained with a FEI PHENOM-Pro. Particle size distributions were determined from the SEM images with ImageJ (version 1.48s, National Institutes of Health, USA). For each sample, 90 particles from three different syntheses were measured (270 particles in total) to obtain length, diameter, and aspect ratio (length/diameter). Powder X-ray diffraction (XRD) patterns were recorded on a STOE STADI P diffractometer in transmission mode (Ge monochromator) with $CuK\alpha_1$ radiation. Nitrogen sorption isotherms were measured at 77 K with a Quantachrome Autosorb iQ MP. Pore size distributions and average pore diameters (d_{DFT}) were determined by a nonlocal density functional theory (NLDFT) model developed for silica exhibiting cylindrical pore geometry.[9] Total pore volumes (V_{tot}) were calculated at a relative pressure p/p_0 of 0.95. Primary mesopore volumes (V_p) were determined from the respective α_S-plots.[10] Adsorption isotherms were used for all calculations.[11]

3.6 References

1. N. Zucchetto and D. Brühwiler, RSC Adv., 2015, 5, 74638-74644.
2. L. K. Patterson and E. Vieil, J. Phys. Chem., 1973, 77, 1191-1192.
3. J. W. Larsen and L. J. Magid, J. Am. Chem. Soc., 1974, 96, 5774-5782.
4. H. P. Lin, C. P. Kao, C. Y. Mou and S. B. Liu, J. Phys. Chem. B, 2000, 104, 7885-7894.
5. S. Ikeda, S. Hayashi and T. Imae, J. Phys. Chem., 1981, 85, 106-112.
6. G. Calzaferri, R. Méallet-Renault, D. Brühwiler, R. Pansu, I. Dolamic, T. Dienel, P. Adler, H. Li and A. Kunzmann, Chem. Phys. Chem., 2011, 12, 580-594.
7. M. Kruk, Acc. Chem. Res., 2012, 45, 1678-1684.
8. N. Gartmann and D. Brühwiler, Angew. Chem., Int. Ed., 2009,48, 6354-6356.
9. J. Landers, G. Y. Gor and A. V. Neimark, Colloids Surf., A, 2013, 437, 3-32.
10. M. Kruk, M. Jaroniec, R. Ryoo and J. M. Kim, Microporous Mater., 1997, 12, 93-106.
11. P. I. Ravikovitch and A. V. Neimark, Colloids Surf., A, 2001, 187, 11-21.

4. FUNCTIONALIZATION OF ARRAYS OF SILICA NANOCHANNELS BY POST-CONDENSATION

The ASNCs morphology is influenced by the relative amounts of silica source and SDA. In particular, the end-on growth is favored when the TEOS/CTAB ratio increases.[1] In fact, the particle aspect ratio increases due to the faster growth of the length (Chapter 3, Figure 3.10). Assuming that the delayed addition of a new silica source during the reaction modifies further the aspect ratio, we proposed a novel functionalization process. The innovation of this method, called post-condensation, is the introduction of functional alkoxysilanes (R-silanes) after stabilization of the ASNCs particle morphology.[2]

4.1 Post-condensation with aminosilanes

Primary and secondary amino-functional alkoxysilanes (NH-silanes) were chosen as model substances, as they allow convenient coupling to fluorescent labels for imaging by confocal laser scanning microscopy (CLSM). The investigated amino-functional alkoxysilanes are shown in Figure 4.1.

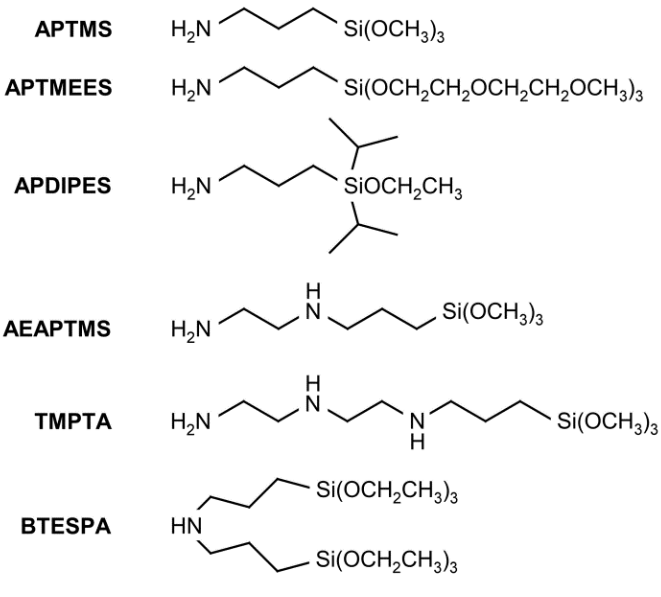

Figure 4.1 Structures and abbreviations of amino-functional alkoxysilanes (NH-silanes).

4.1.1 Morphology

A conventional co-condensation approach with TEOS and NH-silanes under the synthesis conditions for ASNCs led to the formation of agglomerated spheres and irregular particles (Figure 4.2, panel A). Under the strongly acidic conditions, the interactions of protonated silica species (I^+), counter-ion (X^-), and surfactant (S^+) are perturbed by the protonated amines, leading to defects and the formation of an irregular particle morphology. This is in agreement with the previous observation that slight changes in the co-ion and counter-ion composition of the reaction mixture can have a significant effect on the morphology of the ASNCs.[3] The addition of further TEOS after 3 h of reaction time produced a small amount of short hexagonal prismatic particles in addition to the ASNCs obtained in a conventional synthesis (Figure 4.2, panel C), indicating that free surfactant in the reaction mixture is available for establishing $S^+X^-I^+$ interactions.

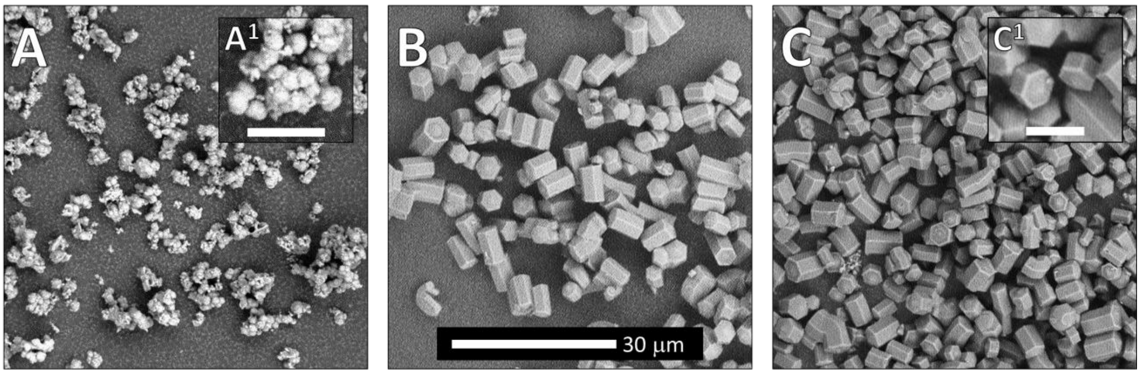

Figure 4.2 SEM images of particles obtained by a co-condensation approach (APTMS/TEOS) under the conditions of the ASNCs synthesis (A). For comparison, ASNCs obtained by the conventional synthesis (without the addition of APTMS) are shown (B). Post-condensation of TEOS leads to the formation of some small ASNCs, but otherwise has no significant effect on the particle morphology (C). The scale bars in A1 and C1 are 5 µm.

The addition of NH-silanes after 3 h of reaction time did not affect the morphology of the ASNCs when the NH-silane/TEOS ratio was kept below 0.3 (Figure 4.3). The variation of the aspect ratio of amino-functionalized ASNCs prepared with different NH-silanes was in this case within the standard deviation range. At a NH-silane/TEOS ratio above 0.3, an increase of the length of the particles was observed, accompanied by the appearance of particles with irregular morphology.

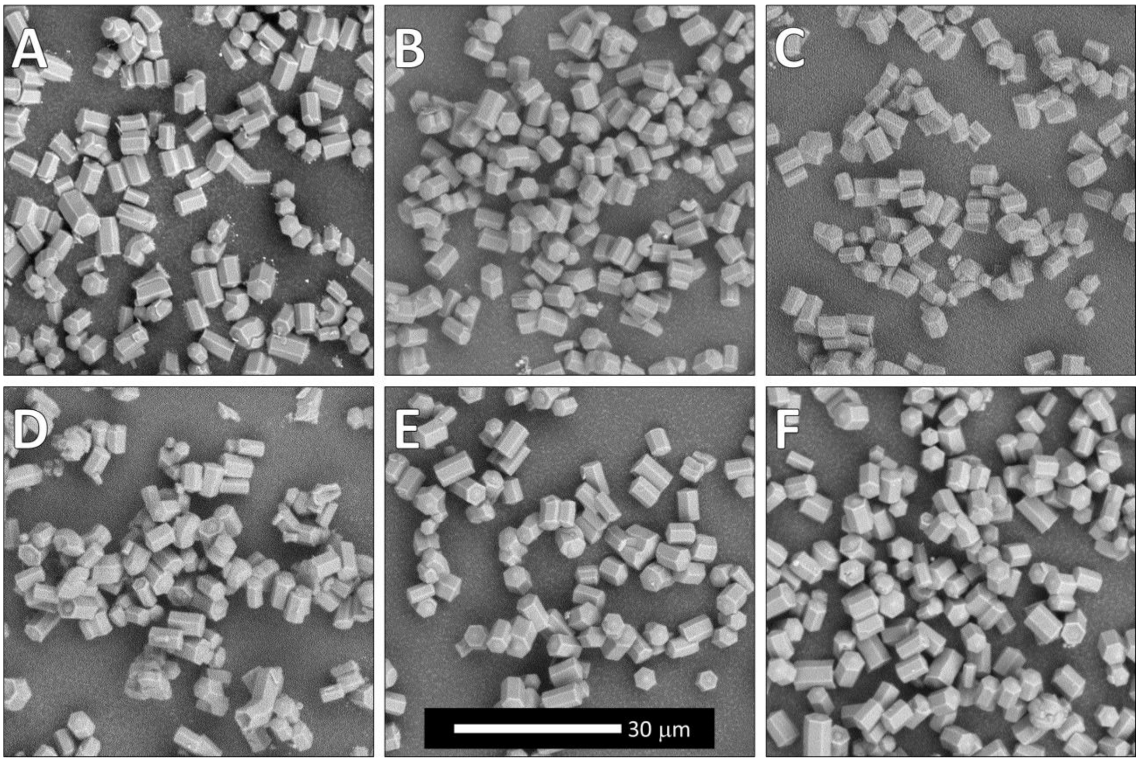

Figure 4.3 SEM images of ASNCs synthesized by post-condensation with different NH-silanes (NH-silane/TEOS = 0.1): APTMS (A), AEAPTMS (B), TMPTA (C), APDIPES (D), BTESPA (E), APTMEES (F).

The post-condensation approach ensures a regular hexagonal prismatic morphology. The following processes might occur upon post-condensation: (i) Condensation of the NH-silane with the existing ASNCs particles, (ii) condensation of NH-silanes (auto-condensation) or (iii) condensation of NH-silanes and free TEOS (co-condensation). The latter two reactions would lead to the formation of small irregular particles that might subsequently condense with the ASNCs. However, for NH-silane/TEOS ratios below 0.3, the first process seems to be predominant. Figure 4.4 shows the three possible processes. In highly acidic solutions, it has been observed that liquid crystal embryos with hexagonal cross-sections develop into mesoporous silica fibers, leading to the conclusion that end-on growth plays a key role in the formation of the mesoporous silica framework under these conditions. Recent studies on the factors influencing the aspect ratio of ASNCs point to the importance of end-on growth in the formation of ASNCs.[1] In the post-condensation of NH-silanes, we can therefore expect that end-on growth directs the NH-silanes towards the hexagonal base surfaces of the ASNCs.

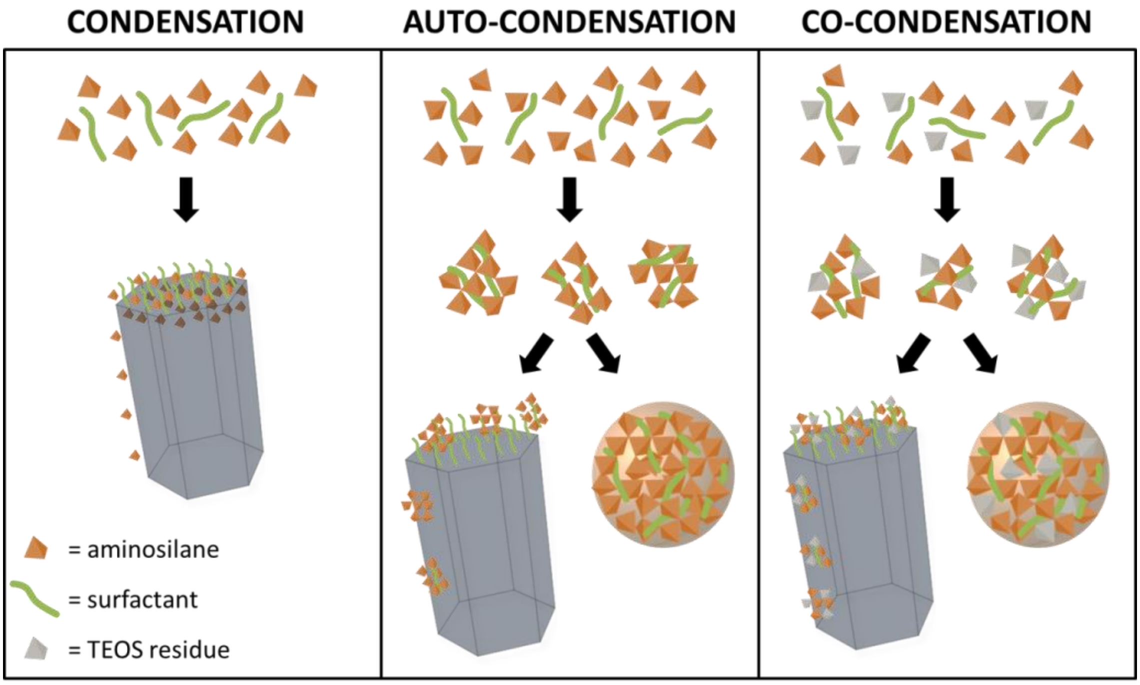

Figure 4.4 Schemes of post-condensation processes: NH-silane condensation on the particle, NH-silane auto-condensation with subsequent condensation on the particle or subsequent new particle formation, NH-silane and free TEOS co-condensation with subsequent condensation on the particle or subsequent new particle formation.

4.1.2 Pore structure

In order to preserve the amino groups in the ASNCs, the SDA needs to be removed under mild conditions. For MCM-41 type materials, efficient removal of alkyltrimethylammonium SDAs has been achieved by extraction with an ethanolic solution of ammonium nitrate.[4]

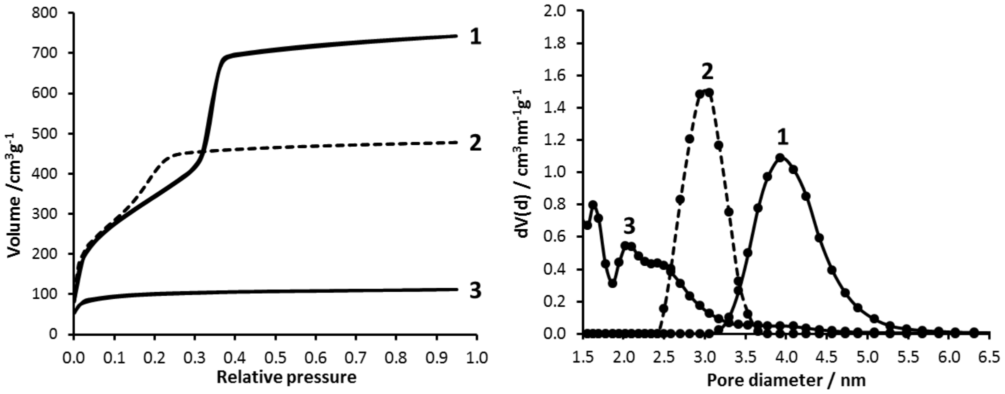

Figure 4.5 Left: Nitrogen sorption isotherms of ASNCs after extraction with thermal pretreatment (1), calcination (2), and extraction without thermal pretreatment (3). Right: respective pore size distributions.

Experiments with pristine ASNCs (prepared without post-condensation of NH-silanes) revealed that applying this established procedure for the extraction of alkyltrimethylammonium SDAs led to a collapse of the ASNCs. As a consequence, a type I isotherm and broad pore size distribution was obtained (Figure 4.5, sample 3). To increase the stability of the silica framework prior to extraction, as-synthesized samples were treated at 150 °C for 10 h. This thermal pretreatment yielded a material featuring the expected reversible type IVb isotherm[5] and a narrow pore size distribution centered at 3.9 nm (Figure 4.5, sample 1). The need for a thermal treatment before extraction is a consequence of the low temperature synthesis of ASNCs, which produces a silica framework with a low degree of cross-linking. A significant decrease of the pore size is therefore observed upon calcination (Figure 4.5, sample 2).

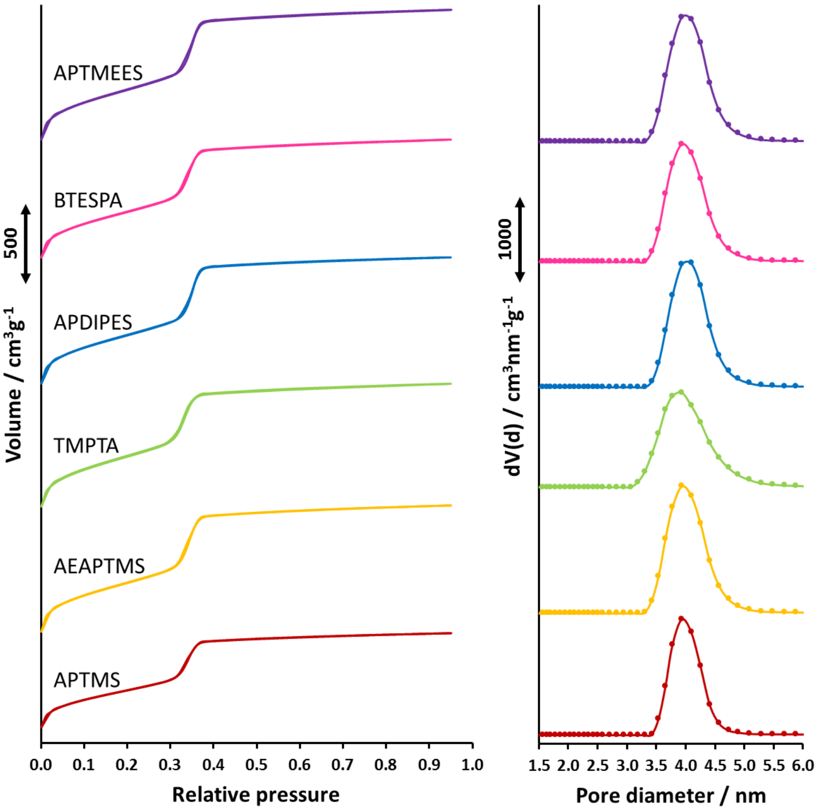

Figure 4.6 Left: nitrogen sorption isotherms. Right: corresponding pore size distributions of amino-functionalized ASNCs prepared by post-condensation and subsequent extraction of the SDA. The abbreviations indicate the respective NH-silane used in the post-condensation (NH-silane/TEOS = 0.1).

Nitrogen sorption isotherms and pore size distributions of samples synthesized by post-condensation with NH-silanes are shown in Figure 4.6 (NH-silane/TEOS = 0.1). The structural properties are summarized in Table 4.1. Comparison with the pristine extracted sample reveals that the NH-silane post-condensation does not cause a significant change in the porosity. All samples feature a reversible type IVb isotherm.

Table 4.1. Structural data of pristine and amino-functionalized ASNCs (NH-silane/TEOS = 0.1). Values in parentheses are the repeat distances of the as-synthesized samples (before extraction).

NH-silane	V_{tot} / cm^3g^{-1}	d_{DFT} / nm	S_{BET} / m^2g^{-1}	a_0 / nm
Pristine (calcined)	0.7	3.1	1406	3.72 (4.71)
Pristine	1.1	3.9	1325	4.57 (4.71)
APTMS	0.9	3.9	1087	4.45 (4.71)
APTMEES	1.2	4.1	1162	4.54 (4.70)
APDIPES	1.2	4.1	1123	4.51 (4.71)
AEAPTMS	1.2	3.9	1421	4.48 (4.70)
TMPTA	1.1	3.9	1349	4.48 (4.68)
BTESPA	1.1	3.9	1057	4.54 (4.67)

The similarity of the pristine and the amino-functionalized samples in terms of porosity is a consequence of post-condensation, i.e., formation of the ordered mesoporous structure prior to the addition of the NH-silane. XRD patterns of the control samples (pristine ASNCs) are shown in Figure 4.7.

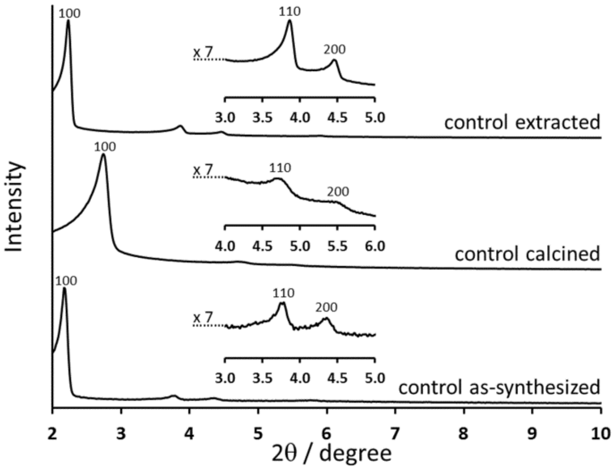

Figure 4.7 XRD patterns of pristine ASNCs. The extracted sample was pretreated at 150 °C before extraction.

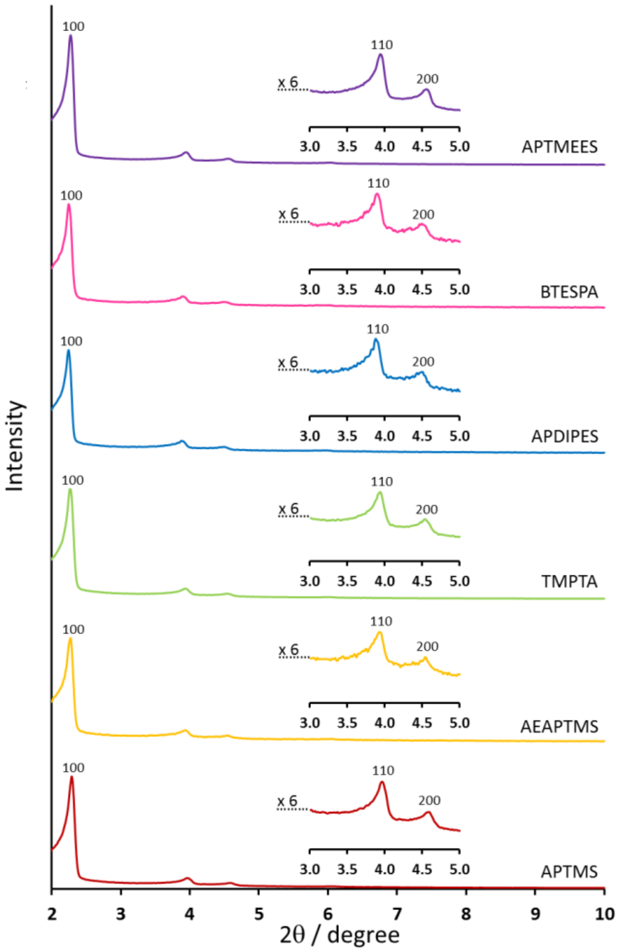

Figure 4.8 XRD patterns of amino-functionalized ASNCs prepared by post-condensation and subsequent extraction of the SDA. The abbreviations indicate the respective NH-silane used in the post-condensation (NH-silane/TEOS = 0.1).

Representative patterns of the amino-functionalized samples are shown in Figure 4.8. All samples feature the typical (100), (110), and (200) reflexes of the 2D hexagonal space group *P6mm*. In agreement with the reduced pore diameter, calcination leads to a decreased repeat distance a_0, indicating a contraction of the silica framework due to further condensation. Thermal treatment of the pristine as-synthesized sample before extraction causes framework stabilization by condensation, which manifests itself in a slightly decreased repeat distance. This effect is also observed when comparing the as-synthesized and extracted amino-functionalized samples (Table 4.1).

4.1.3 Distribution of amino groups

The spatial distribution of the amino groups was determined by CLSM after FITC coupling (Figure 4.9). FITC coupling was conducted before (as-synthesized samples) or after (extracted samples) removal of the SDA.

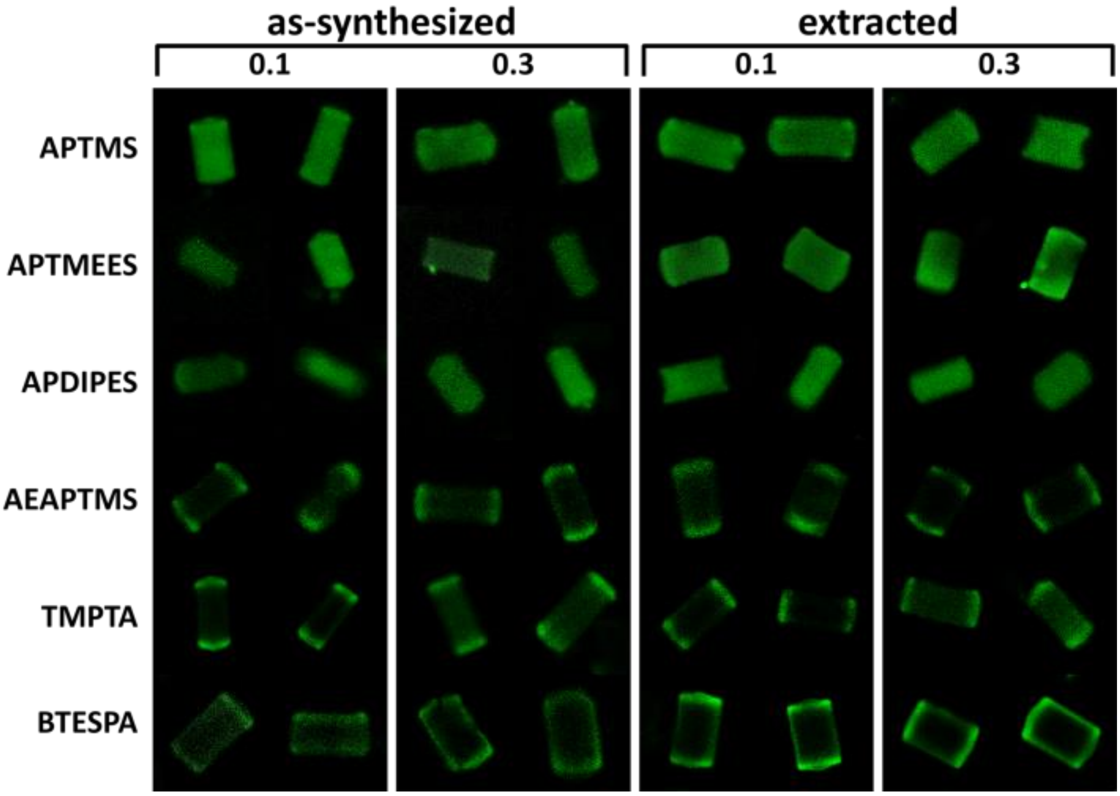

Figure 4.9 CLSM images of FITC-labeled amino-functionalized ASNCs prepared by post-condensation. The columns contain images for as-synthesized and extracted samples produced with NH-silane/TEOS ratios of 0.1 and 0.3. The respective NH-silane is indicated on the left. Optical slices in the center of the particles were selected (excitation at 488 nm).

Comparison of the as-synthesized and extracted samples shows that the presence of the SDA does not affect the distribution of the fluorescein moieties after FITC coupling. However, the CLSM images of the extracted samples appeared brighter. This is most likely due to a better FITC coupling yield in the case of the extracted samples. It has been shown that steric hindrance plays an important role in the postsynthetic functionalization of ASNCs with NH-silanes.[6] Post-condensation is fundamentally different from postsynthetic functionalization. Introduction of the NH-silane into the low pH reaction mixture leads to a fast hydrolysis of the alkoxysilane and protonation of the amino groups. We can therefore expect that in post-condensation, the size of the alkoxy groups does not influence the final distribution of the amino groups on the ASNCs and that the protonated NH-silanes can exchange the SDA in the ASNCs. This is best seen in the comparison of APTMS and APTMEES, which both lead to a relatively uniform distribution of FITC-labeled amino groups despite differently sized alkoxy moieties (Figure 4.9). In the case of APDIPES, a favorable interaction of the isopropyl moieties with the hydrophobic tail of the SDA might further support a uniform distribution. These results are in contrast to postsynthetic functionalization, where APTMEES can be used to generate a selective functionalization of the external surface.[6] Unlike classical co-condensation, post-condensation can lead to non-uniform distributions of functional groups. In the case of AEAPTMS, TMPTA, and BTESPA, fluorescence was mainly observed at the base surfaces of the ASNCs, indicating a significant degree of pore entrance functionalization (Figure 4.9). The accumulation of FITC-labeled amino groups at the pore entrances is particularly evident for samples synthesized with AEAPTMS and TMPTA. The comparatively large size of these molecules in combination with end-on (axial) growth[7,8] is most likely responsible for the pore entrance accumulation. The selective functionalization of the channel entrances is of interest for establishing concepts of controlled release, e.g. via the grafting of molecular gates.[9] Methods for the selective functionalization of pore entrances are only useful if the pores remain accessible.

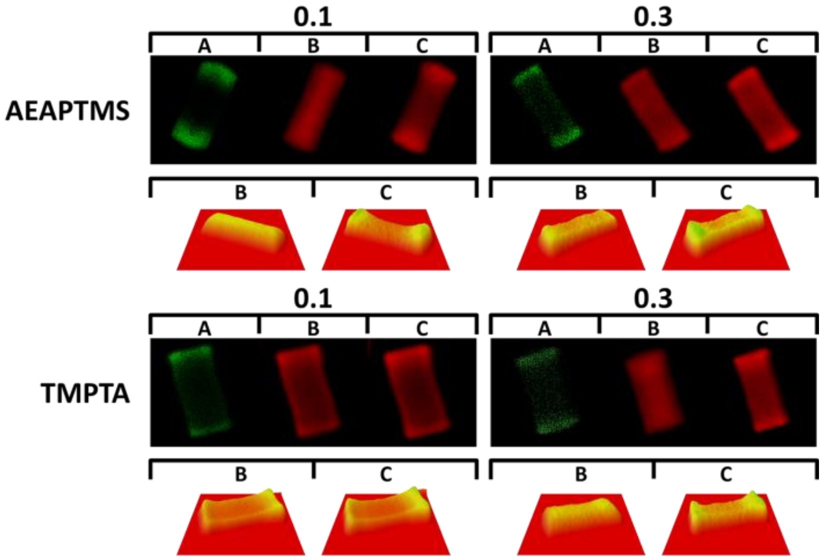

Figure 4.10 CLSM images of FITC-labeled amino-functionalized ASNCs prepared by post-condensation (NH-silane/TEOS ratio 0.1 or 0.3) and subsequent postsynthetic modification with APTMS and TR-labeling. A) Excitation at 488 nm and observation of FITC fluorescence. B) Excitation at 543.5 nm and observation of TR fluorescence. C) Excitation at 488 nm and observation of TR fluorescence. The distribution of the fluorescence intensity in the images B and C is also given by the corresponding intensity profiles (red: low intensity, yellow: intermediate intensity, green: high intensity). Optical slices in the center of the particles were selected.

To test the accessibility of pore entrance functionalized samples, we have conducted FITC coupling, followed by postsynthetic functionalization with APTMS and labeling with Texas Red (TR). The corresponding CLSM images indicate that the TR labels have entered the nanochannels, despite the presence of the fluorescein labels at the pore entrances (Figure 4.10). This indicates that the pores are accessible for pore surface functionalization. An interesting effect is observed in the FITC/TR-labeled samples. For samples prepared with AEAPTMS, the TR labels are distributed rather uniformly throughout the material. This is best seen in the images B of Figure 4.10, which were acquired by excitation at 543.5 nm, where the absorption of the fluorescein labels is negligible, and observation of the TR fluorescence. However, excitation at 488 nm and observation of the TR fluorescence reveals an increased intensity at the channel entrances (images C, Figure 4.10). As the absorption of TR is negligible at 488 nm, the increased TR fluorescence is most likely caused by energy transfer from the fluorescein labels located at the channel entrances. A similar effect is observed for the samples prepared with TMPTA. When inspecting several of the FITC/TR-labeled particles, we noticed instances of non-uniform TR distributions, as shown in the lower left panel of Figure 4.10. Selective observation of the TR labels indicates an accumulation of TR at the pore entrances, which could be the result of pores partially blocked by the large TMPTA-FITC conjugates.

4.2 Post-condensation with alkylsilanes

Alkylsilanes are generally used to adjust the dispersibility and the interaction of the particles with nonpolar molecules. This process leads to capping of the surface silanol groups and is therefore often termed “passivation”.

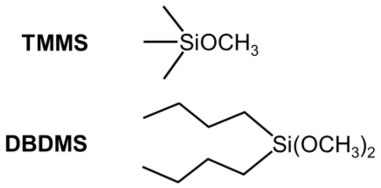

Figure 4.11 Structures and abbreviations of alkyl-functional alkoxysilanes.

The passivated surface is composed of alkyl moieties that are less reactive than the silanol groups. In order to obtain more information about the reactivity of these silanes during the post condensation process, two alkylsilanes were used (Figure 4.11).

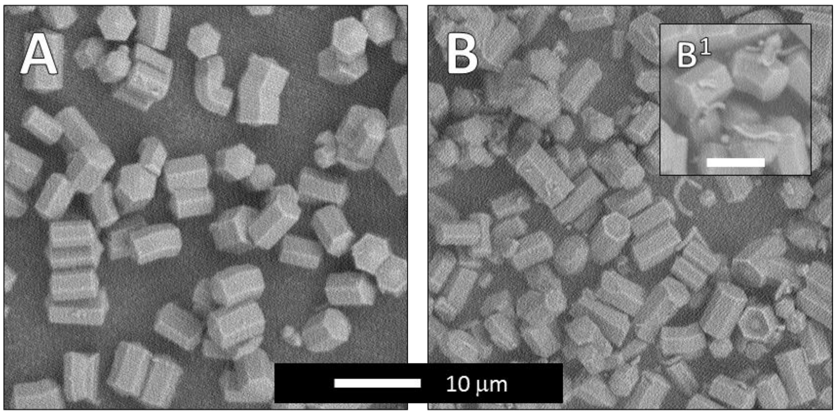

Figure 4.12 SEM images of ASNCs synthesized by post-condensation with different alkylsilanes (alkylsilane/TEOS = 0.1): TMMS (A) and DBDMS (B). The white scale bar in panel B^1 represents 5 µm.

As confirmed previously, the particle shape is regular, not influenced by the post-condensation process for alkylsilane/TEOS ratios less than 0.3 (Figure 4.12). Irregular byproducts appeared when the alkyl chain length was increased as shown in Figure 4.12, panel B^1. It is noticeable that the amount of these irregular particles increases when high alkylsilane/TEOS ratios are used.

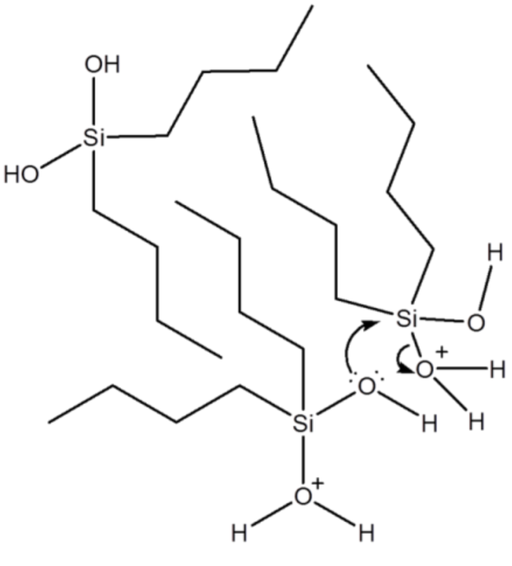

Figure 4.13 Schematic representation of interactions between the alkyl chains and subsequent condensation of the silanol groups.

The auto-condensation process (Figure 4.4) explained for the NH-silane post-condensation might also occur for the alkylsilane addition. During the condensation the aqueous medium promotes the interactions between apolar chains of the alkylsilanes. When an alkylsilane is added to the ASNCs reaction three steps might occur: (i) fast hydrolysis of the alkoxy groups, (ii) interactions between the apolar chains and (iii) condensation of the adjacent silanols (Figure 4.13). The presence of the irregular byproducts suggests that the auto-condensation process is favored for the post-condensation reaction with DBDMS. A postsynthetic method with an accessible aminosilane (APTMS) is used to study the passivation degree. APTMS reacts with free silanol groups, therefore the distribution of the added amino groups can help to explain if the passivation is complete or partial. CLSM images were collected after the coupling with FITC in two different solvents: polar (ethanol) and apolar (toluene) as shown in Figure 4.14.

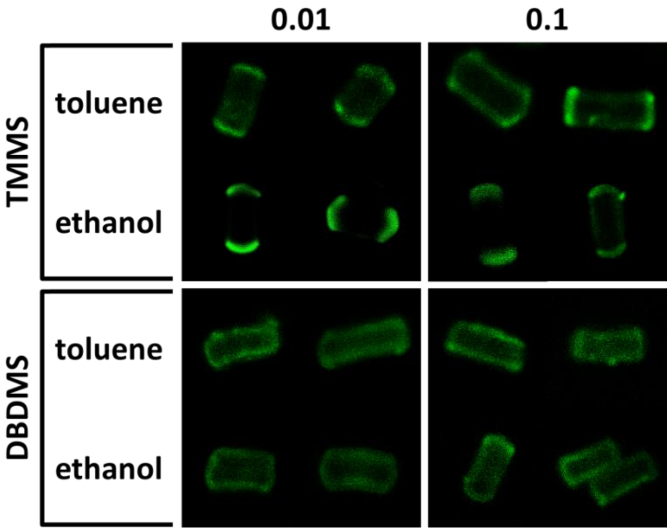

Figure 4.14 CLSM images (after postsynthetic functionalization with APTMS and subsequent coupling with FITC) of one-pot ASNCs functionalized with two different alkylsilanes. The coupling with FITC was made in two different solvents: toluene and ethanol.

The coupling experiments show the presence of the amino groups on the external surface and thus indicate that the passivation is not complete and the pore surface becomes inaccessible. This result is in agreement with the low passivation degree due to the auto-condensation process.

4.3 Multi-shell arrays of silica nanochannels

Hindrance and particle growth are the main effects that influence the functional group distribution during the post-condensation process. As described in Chapter 2.2.5, the growth depends on the reaction pH, ionic strength and dielectric constant.[9] The addition of different chemicals (salts, solvents, etc.) can influence these parameters and modify the final particle morphology.[1] The experiments conducted using aminosilanes (Chapter 4.1) demonstrate that the post-condensation does not influence the overall particle structure and morphology.[2] Starting from these results, we decided to improve this process to obtain multi-shell particles with the functional groups accumulated at the pore entrances.

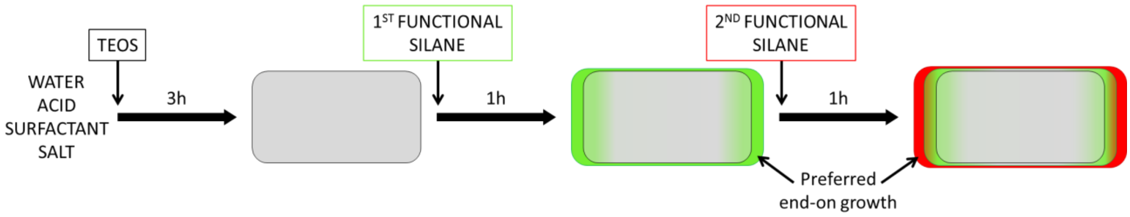

Figure 4.15 Scheme of tandem post-condensation in order to obtain a multi-shell particle. After 1 hour from the first functional silane addition, a second functional moiety is added to the reaction.

As shown previously, CLSM can be used to visualize the functional group distribution in the particle after the dye coupling. The tandem post-condensation cannot be performed using two different aminosilanes, in fact, the subsequent dye coupling process will not discriminate between the first and the second aminosilane. Different strategies were considered to solve this problem.

4.3.1 Dye-coupled aminosilanes

The post-synthetic labeling problem was solved using a pre-coupled aminosilane (so called dye-silane) as functional silane. With this method, the sterical hindrance is increased leading to the formation of particles functionalized selectively at the pore entrances as shown in Figure 4.16.

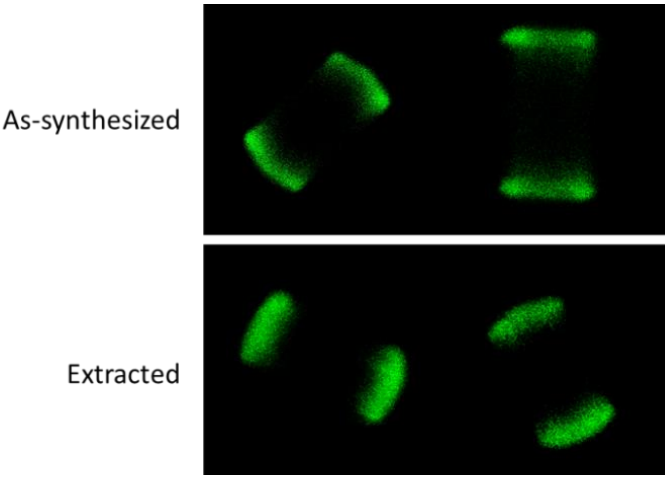

Figure 4.16 CLSM pictures of post-condensed ASNCs with FITC-coupled aminosilane (FITC-silane) with a dye-silane/TEOS ratio = 0.03

The synthesis was performed with three different dye-silane/TEOS ratios (0.01, 0.03 and 0.05) obtaining the same results in terms of morphology and functional group distribution. For this reason the subsequent experiments were performed with a dye-silane/TEOS ratio = 0.03. An excess of aminosilane (APTMS) was used during the coupling process (dye/aminosilane ratio = 0.1) to prevent the free dye physisorption on the particle surface after the addition. APTMS showed a high mobility during the ASNCs post-condensation (Chapter 4.1.3). A labeling reaction with Rhodamine isothiocyanate (RhITC) was performed to evaluate the distribution of the excess aminosilane. Figure 4.17 shows the distribution of the functional groups.[2,6] The FITC-silanes and the RhITC labeled amino groups are localized at the pore entrances.

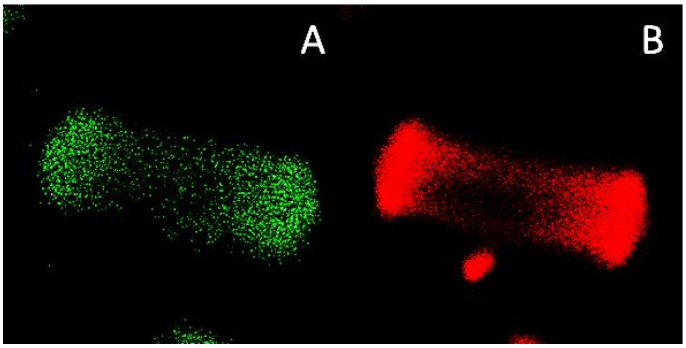

Figure 4.17 CLSM image of post-condensed ASNCs (extracted) with FITC-coupled aminosilane (panel A, excitation at 488 nm and observation of FITC fluorescence) and subsequently labeled with Rhodamine isothiocyanate (panel B, excitation at 543.5 nm and observation of RhITC fluorescence).

This result is in contrast with the previous experiments (Figure 4.18) that showed an uniform aminosilane distribution for APTMS. The first difference between these results is the amount of functional silane used. The NH-silane/TEOS ratio (or dye-silane/TEOS ratio) is approximatively 3-10 times less in the dye-coupled aminosilane experiments. It is important to consider the long coupling time that can contribute to the formation of oligomers composed of aminosilanes and dye-coupled aminosilanes (Figure 4.4, auto-condensation). In this way the effective sterical hindrance is increased and the mobility reduced, leading to a localized distribution. The accessibility of the functionalized ASNCs was evaluated by grafting a bulky aminosilane (postsynthetic functionalization with TMPTA) and the results are shown in Figure 4.18. The homogeneous distribution of the post-grafted aminosilanes indicates that the pore surface of the particles is still accessible for further functionalization (Figure 4.18, panel B). The Förster resonance energy transfer (FRET) effect visible in panel C confirms the presence of both dyes at the channel entrances.

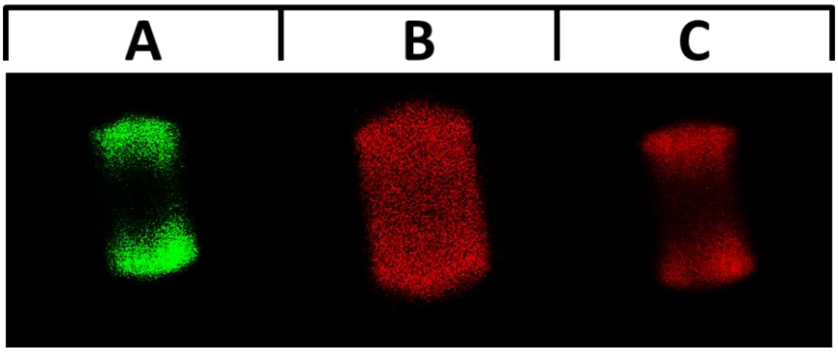

Figure 4.18 CLSM image of post-condensed ASNCs particle (extracted) with FITC-coupled aminosilane (panel A, excitation at 488 nm and observation of FITC fluorescence) and subsequent postsynthetic modification with TMPTA and RhITC-labeling (panel B, excitation at 543.5 nm and observation of RhITC fluorescence). FRET effect between FITC and RhITC (panel C, excitation at 488 nm and observation of RhITC fluorescence).

4.3.2 Tandem post-condensation with dye-silanes

To design multi-shell ASNCs, two different dye-silanes were used: FITC-silane and RhITC-silane. The tandem synthesis scheme reported in Figure 4.15 shows a concept to obtain particles with three different frameworks. The core is represented by the ASNCs body (not functionalized) and the first and second layers are composed of the functional silanes. Figure 4.19 shows the CLSM images obtained after tandem post-condensation. In order to obtain more information, the experiments were performed using FITC-silane and RhITC-silane as first and second dye-silanes (Figure 4.19, top) and RhITC-silane and FITC-silane as first and second dye-silanes (Figure 4.19, bottom).

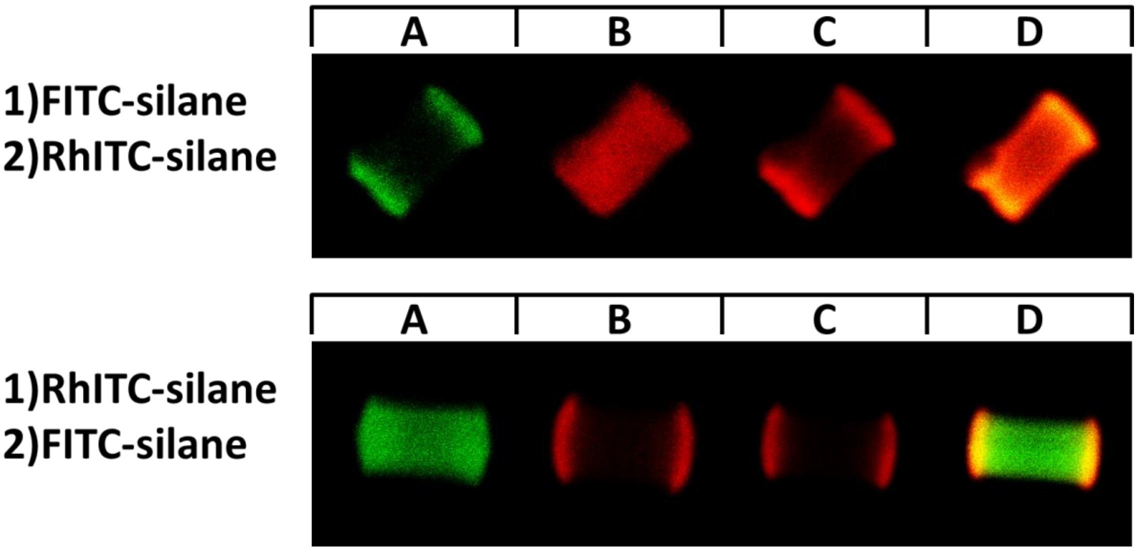

Figure 4.19 CLSM images of ASNCs tandem post-condensation. Top: FITC-silane (1st dye-silane) and RhITC-silane (2nd dye-silane). Bottom: RhITC-silane (1st dye-silane) and FITC-silane (2nd dye-silane). Excitation at 488 nm and observation of FITC fluorescence (panels A), excitation at 543.5 nm and observation of RhITC fluorescence (panels B), excitation at 488 nm and observation of RhITC fluorescence (panels C) and excitation at 488 and 543 nm and observation of both FITC and RhITC fluorescence (panels D).

The results confirm that the scheme reported in Figure 4.15 is not realistic, in fact the second functional silane addition led to a complete internal functionalization (Figure 4.19, top panel B and bottom panel A). Figure 4.20 illustrates the possible mechanism leading to the observed dye distribution.

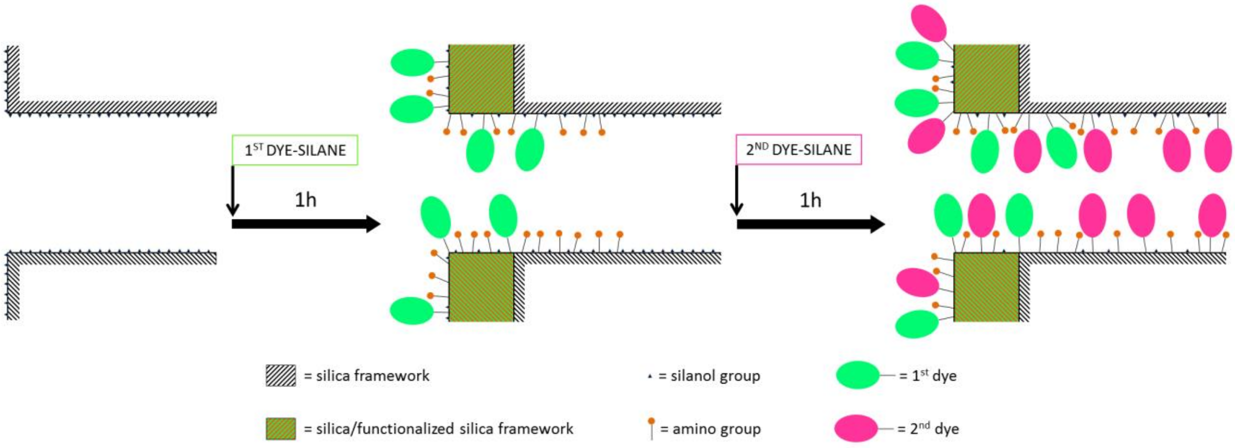

Figure 4.20 Schematic representation of the events during the tandem post-condensation with two dye-silanes.

Before the first addition, the surface is composed of silanols and protonated silanols (pH below the PZC). New surface groups (dye-coupled and amino functions) are introduced when the solution containing mono-substituted functional silanes (dye-trimethoxysilane with an excess of aminosilane) are added. The number of the growth sites (silanols or protonated silanols) located at the pore entrances decreases and these available silanol groups are partially shielded by the bulky introduced molecules. The end-on growth is less favored when the second dye-silane is introduced. The majority of the free silanol groups is located on the pore surface and available for reaction with the second dye-silane.

4.4 Delayed addition of sodium hydroxide

Interesting results were obtained by increasing the solution pH via the addition of sodium hydroxide. As explained by Ozin,[9] as a consequence of increasing the pH, the superficial charges change favoring the side-on growth. Applying this concept to the post-condensation process, a particle diameter expansion was expected. Figure 4.21 shows the results obtained by adding two different quantities of NaOH after three hours of reaction.

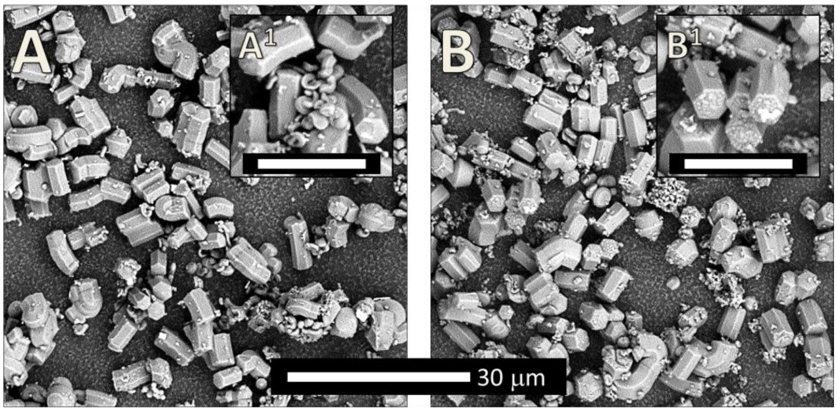

Figure 4.21 SEM pictures of ASNCs synthesized with delayed addition of sodium hydroxide. Different amounts of NaOH were used: 5 g (A and A1) and 10 g (B and B1). The white scale bar in panels A^1 and B^1 represents 10 μm.

As expected for post-condensation, the hexagonal prismatic shape is preserved, but new deformed and spherical silica nanoparticles appear. The base addition does not favor the diameter growth but it causes the precipitation of the TEOS residues. The reaction environment is still acidic after the NaOH addition, but the silica condensation is slowed down. It is clear that the agglomeration and the new seed formation are favored compared to the side-on growth. There is noticeable agglomeration of the spherical nanoparticles on the ASNCs pore entrances (hexagonal face, Figure 4.21, panel B^1) indicating the partial end-on growth.

4.5 Conclusion

The preparation of amino-functionalized ASNCs by post-condensation preserves the well-defined hexagonal prismatic particle morphology and narrow pore size distribution. The distribution of the amino groups in the ASNCs can be controlled by the type of amino-functional alkoxysilane. Molecules that are sterically hindered after hydrolysis in a low pH reaction mixture tend to accumulate at the channel entrances. Dual fluorescent labeling experiments and CLSM imaging revealed that the nanochannels of post-condensed ASNCs are accessible for further postsynthetic functionalization steps. This provides possibilities for the preparation of multifunctional mesoporous particles with defined functional group distributions. Partially passivated ASNCs were obtained by using alkylsilanes during the post-condensation. The particle surface was still available for further functionalization, preferentially on the external surface and at the pore entrances. Preliminary tests with dye-silanes were performed in order to obtain multi-shell ASNCs. It was confirmed that sterical hindrance and the end-on growth lead to particles which are selectively functionalized at the pore entrances. The addition of a second dye-silane does not form a new framework but functionalizes the internal surface. This result is due to the limited end-on growth after the first addition and the availability of the pore surface silanol groups. During the ASNCs synthesis, the delayed addition of NaOH showed that small particles are formed confirming the presence of TEOS (or silica source) residues. The selective functionalization of the channel entrances is expected to provide a starting point for introducing stimuli-responsive molecular gates[10] or for establishing a vertical orientation of ASNCs on a flat surface as well as specific particle-particle interactions, similar to what has been achieved for microporous materials such as zeolite L.[11-13]

4.6 Experimental

4.6.1 Materials

Hexadecyltrimethylammonium bromide (CTAB, for molecular biology, ≥99%), $CaCl_2$ (≥97.0%), concentrated hydrochloric acid (puriss. p.a., ≥32%), (NaOH, ≥98%), tetraethoxysilane (TEOS, 99.999%), 3-aminopropyltrimethoxysilane (APTMS, 99%), [3-(2-aminoethylamino)-propyl]trimethoxysilane (AEAPTMS, 95%), N1-(3-trimethoxysilylpropyl)diethylenetriamine (TMPTA, technical grade), methoxytrimethylsilane TMMS, 99%) and diisobutyldimethoxysilane (DBDMS, technical grade) were obtained from Sigma-Aldrich. 3-Aminopropyldiisopropylethoxysilane (APDIPES, 97%), bis(triethoxysilylpropyl)amine (BTESPA, 95%), and 3-aminopropyltris-(methoxyethoxyethoxy)silane (APTMEES, 95%) were obtained from ABCR. The fluorescent labels fluorescein isothiocyanate (FITC, isomer I, ≥90%), Texas Red sulfonyl chloride (TR, technical grade), rhodamine B isothiocyanate (RhITC, mixed isomers) and the solvents ethanol (purum, ≥99.8%) and toluene (anhydrous, 99.8%) were obtained from Sigma-Aldrich. All chemicals were used as received.

4.6.2 Synthesis of amino-functionalized and passivated ASNCs by post-condensation

CTAB (4.0 g, 11 mmol) and $CaCl_2$ (1.50 g, 13.5 mmol) were dissolved in a mixture of doubly distilled H_2O (76 mL, 4.2 mol) and concentrated hydrochloric acid (≥32%, 60 mL, 0.62 mol) by stirring for 15 min in a polypropylene beaker. The solution was subsequently cooled in an ice bath for 15 min under quiescent conditions, followed by the slow addition of cold TEOS (4 °C, 2.0 mL, 9 mmol) and further stirring for 30 s. The resulting mixture was kept at 0 °C under quiescent conditions for 3 h. After this period, the solution was stirred for 1 min while adding the desired amount of NH-silane or alkylsilane and subsequently kept at 0 °C under quiescent conditions for 1 h. The product was filtered off and dried at 80 °C. In the case of samples prepared by the classical co-condensation route, the NH-silanes were added with TEOS at the start of the synthesis. The amount of functional silane was calculated using two different R-silane/TEOS ratios: 0.1 and 0.3.

For removing the structure-directing agent (SDA), the product was first heated at 150 °C for 10 h and then extracted by stirring a 100 mg amount in a solution of ethanol (20 mL) and ammonium nitrate (80 mg) at 60 °C for 15 min, followed by centrifugation. After repeating this extraction step twice, the product was washed with ethanol (20 mL) and dried at 80 °C overnight.

4.6.3 Fluorescent labeling

The samples were labeled by stirring (16 h at room temperature) the amino-functionalized ASNCs (50 mg) in absolute ethanol (5 mL) containing FITC (2 mg). After centrifugation, the labeled samples were washed with absolute ethanol until the washing solution became colorless. The samples were dried at 80 °C.

4.6.4 Accessibility test

To test the accessibility for pore surface functionalization, extracted FITC-labeled samples (100 mg) were dispersed in absolute ethanol (5 mL) and APTMS (2 µL) was added. After the mixture had been stirred for 10 min at room temperature, the solid was recovered by centrifugation and cured in an oven at 80 °C for 6 h. TR (1 mg) was added to the dried powder (50 mg) with subsequent stirring in absolute ethanol for 16 h at room temperature. After centrifugation, the sample was washed repeatedly with absolute ethanol until the washing solution became colorless.

4.6.5 Postsynthetic amino functionalization of ASNCs

Postsynthetic amino functionalization was performed to verify the passivation degree of ASNCs post-condensed with alkylsilanes (Figure 4.14) and to test the accessibility of ASNCs post-condensed with a dye-silane (Figure 4.18). Amino groups were grafted to the mesoporous silica materials as follows: modified ASNCs (200 mg) were dispersed in toluene (10 mL), and APTMS (20 mmol, for passivated ASNCs) or TMPTA (20 mmol, for dye-coupled ASNCs) was added. After the mixture had been stirred for 10 min, the functionalized mesoporous silica was recovered by filtration and cured in an oven at 80 °C overnight.

4.6.6 Dye-aminosilane coupling

Dye-silanes were prepared by stirring 10 mL of an ethanolic APTMS solution (0.086 mM, 16 h at room temperature) and the isothiocyanate dye (dye/aminosilane molar ratio = 0.1). This solution was degassed, flushed with nitrogen a few times and kept under inert conditions during stirring.

4.6.7 Synthesis of dye-functionalized ASNCs by post-condensation and tandem post-condensation

During the ASNCs synthesis after the TEOS addition (4 °C, 2.0 mL, 9 mmol) and subsequent quiescent conditions (0 °C, 3 h), the suspension was stirred for 1 min while adding the desired amount of solution from dye-aminosilane coupling (0.01, 0.03 and 0.05 dye-silane/TEOS ratios). The resulting suspension was kept at 0 °C under quiescent conditions for 1 h. After this time the addition procedure was repeated (stirring 1 min and adding the desired compound, dye-silane/TEOS ratio = 0.03) using a different dye-coupled aminosilane (for a tandem post-condensation) or isothiocyanate dye (as control). The product was filtered off and dried at 80 °C. Template extraction or postsynthetic treatments were performed as described previously.

4.6.8 Delayed addition of NaOH

During the ASNCs synthesis after the TEOS addition (4 °C, 2.0 mL, 9 mmol) and subsequent quiescent conditions (0 °C, 3 h), the suspension was stirred for 3 min while adding the desired amount of NaOH (5 or 10 g). The solution was kept at 0 °C under quiescent conditions for 1 h and the product was filtered off and dried at 80 °C.

4.6.9 Physical measurements

Nitrogen sorption isotherms were measured at 77 K with a Quantachrome Autosorb iQ MP. Pore size distributions and pore diameters d_{DFT} were calculated by non-local density functional theory (NLDFT, silica with cylindrical pores, ASiQwin, version 3.01).[7] Surface areas S_{BET} were determined by multipoint BET.[8] Total pore volumes V_{tot} were derived from the amount of adsorbed nitrogen at a relative pressure of $p/p_0 = 0.95$. Adsorption isotherms were used for all calculations. Scanning electron microscopy (SEM) images were obtained with a FEI Phenom Pro. CLSM was performed with an Olympus BX60 microscope equipped with a FluoView FV300 confocal unit and excitation at 488 or 543.5 nm. Powder X-ray diffraction (XRD) patterns were recorded on a STOE STADI P diffractometer with $CuK\alpha_1$ radiation.

4.7 References

1. N. Zucchetto and D. Brühwiler, RSC Adv., 2015, 5, 74638-74644.
2. N. Zucchetto and D. Brühwiler, Dalton Trans., 2016, 45, 14363-14369.
3. N. Gartmann, C. Schütze, H. Ritter and D. Brühwiler, J. Phys. Chem. Lett., 2010, 1, 379-382.
4. N. Gartmann and D. Brühwiler, Materials, 2011, 4, 1096-1103.
5. N. Lang and A. Tuel, Chem. Mater., 2004, 16, 1961-1966.
6. N. Gartmann and D. Brühwiler, Angew. Chem., Int. Ed., 2009, 48, 6354-6356.
7. J. Landers, G. Y. Gor and A. V. Neimark, Colloids Surf., A, 2013, 437, 3-32.
8. S. Brunauer, P. H. Emmett and E. Teller, J. Am. Chem. Soc., 1938, 60, 309-319.
9. H. Yang, N. Coombs and G. A. Ozin, Nature, 1997, 386, 692-695.
10. E. Aznar, M. Oroval, L. Pascual, J. R. Murguia, R. Martinez-Máñez and F. Sancenón, Chem. Rev., 2016, 116, 561-718.
11. A. Zabala Ruiz, H. Li and G. Calzaferri, Angew. Chem., Int. Ed., 2006, 45, 5282-5287.
12. J. S. Lee, H. Lim, K. Ha, H. Cheong and K. B. Yoon, Angew. Chem., Int. Ed., 2006, 45, 5288-5292.
13. Z. Popović, M. Busby, S. Huber, G. Calzaferri and L. De Cola, Angew. Chem., Int. Ed., 2007, 46, 8898-8902.

5. SYNTHESIS AND CHARACTERIZATION OF ORDERED MESOPOROUS SILICA-TITANIA PARTICLES

Particles with composite frameworks are of interest for application fields such as catalysis[1] or environmental remediation.[2-4] In particular the photodegradation of pollutants from air and water sources is currently a hot topic. Titanium dioxide is a well-known photocatalyst in the field of environmental remediation. Combining the advantages of the mesoporous silica materials (convenient synthesis and functionalization, high surface area, etc.) with the catalytic properties of titanium dioxide (TiO_2) leads to ordered mesoporous silica-titania composite particles.

5.1 Synthesis of ordered mesoporous silica-titania particles

Mesoporous materials with photoactive properties have been studied extensively in the last years.[1,5-8] Mesoporous silica particles such as MCM-41 and SBA-15 are the perfect starting point to achieve photoactive materials due to their textural properties and convenient surface functionalization. The addition of titanium atoms to the silica framework, in the form of titanium dioxide, can be achieved in three different ways. Co-condensation[9-10] and impregnation[5-8] are well-known techniques to synthesize and functionalize mesoporous silica particles. Post-condensation, developed in this work, is the third method to obtain the silica-titania composites. Modified ASNCs, containing titanium atoms (Ti-ASNCs), were synthesized with these methods starting from the silicon and titanium alkoxides (tetraethoxysilane (TEOS) and titanium tetraisopropoxide (TTIP)) and using different titanium-silicon molar ratios (Ti/Si ratio).

5.1.1 Morphology and textural properties

The characteristic shape of ASNCs is due to the regular growth under particular synthetic conditions.[11] The impregnation method is a postsynthetic treatment consisting of the formation and grafting of crystalline structures (derived from the metal alkoxide used) on the substrate surface after the solvent evaporation. This method can modify the textural properties (pore size, pore volume and surface area) without altering the particle shape.[12-13] Co-condensation and post-condensation, on the other hand, influence strongly the particle morphology in particular when the molar ratio between functionality and silane increases.[14]

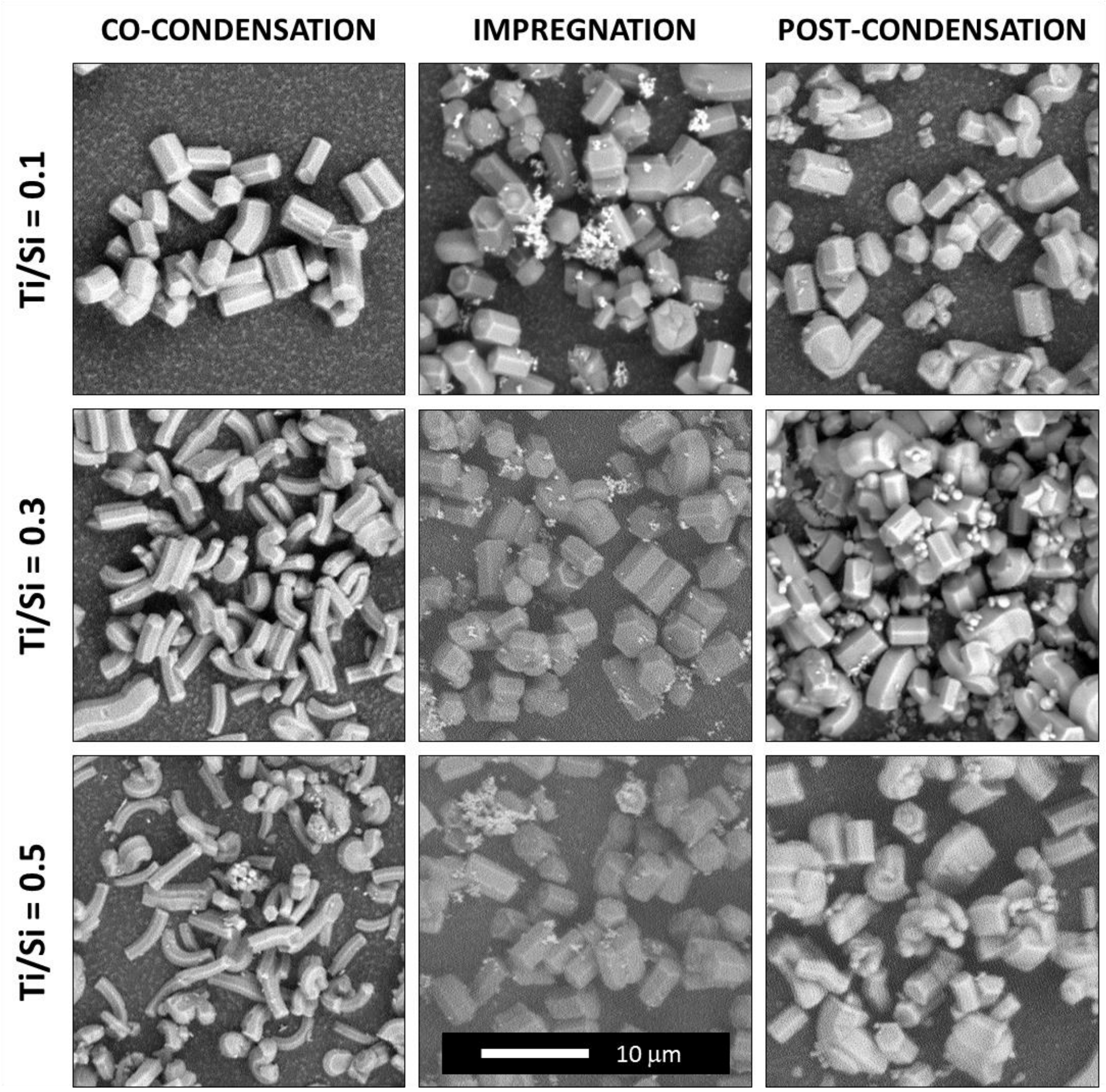

Figure 5.1 SEM pictures of Ti-ASNCs particles synthesized with three different methods (co-condensation, impregnation and post-condensation) and with three different titanium/silicon ratios (0.1, 0.3 and 0.5).

The SEM images of co-condensed, impregnated and post-condensed Ti-ASNCs are reported in Figure 5.1. As expected, the impregnation process does not modify the morphology and size of the ASNCs. However, small spherical TiO_2 particles were obtained a byproduct. SEM images of post-condensed Ti-ASNCs show a mixture of well-shaped and deformed hexagonal particles and also byproducts with an irregular shape. High Ti/Si ratios lead to increased deformations and the production of secondary particles.[14] Contrarily from the results obtained with aminosilanes (irregular spherical particles, Figure 4.2) the co-condensation of TEOS and TTIP leads to the formation of Ti-ASNCs with the characteristic prismatic shape. The particle growth with the addition of TTIP is comparable with the original ASNCs and consequently the morphology is not influenced. In fact, the particle length increases when the Ti/Si molar ratio is higher, in agreement with previous results (Figure 3.10).

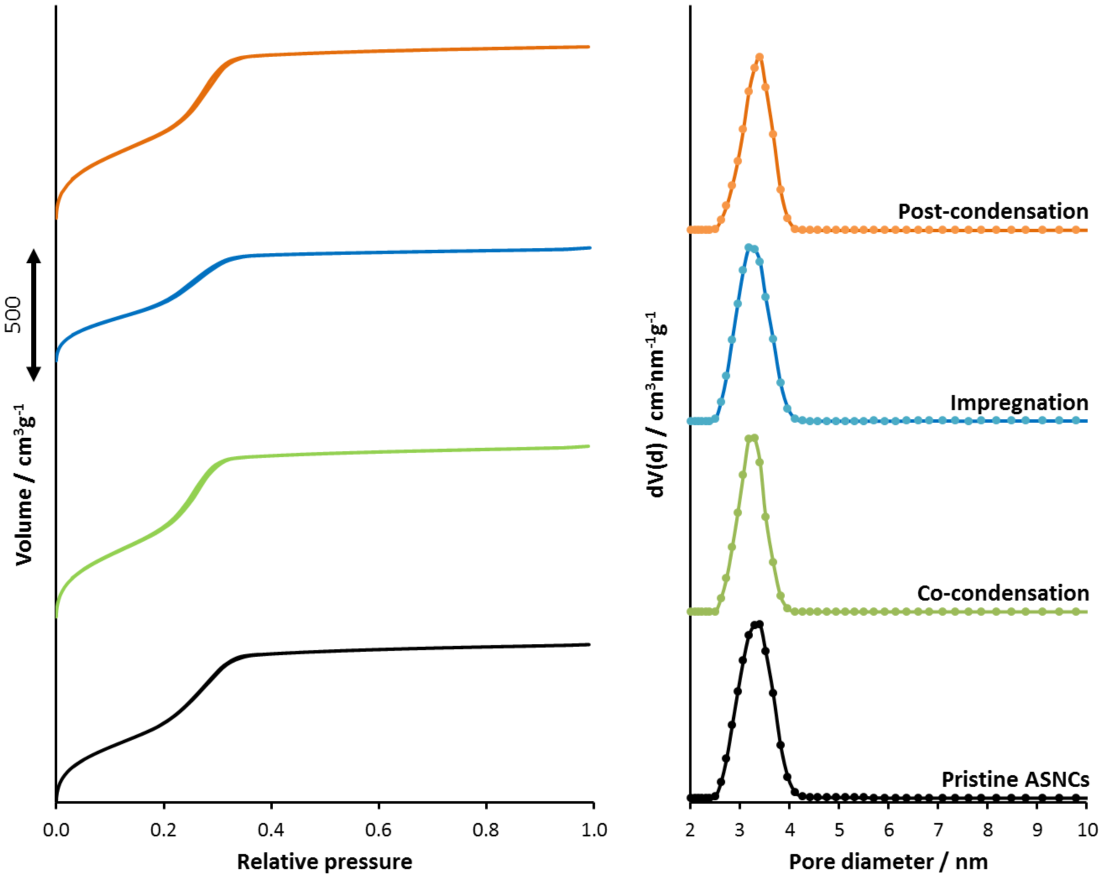

Figure 5.2 Argon sorption isotherms (left) and corresponding pore size distributions (right) of pristine ASNCs and Ti-ASNCs synthesized with three different methods: co-condensation, impregnation and post-condensation (Titanium/silicon ratio = 0.5). The isotherms and normalized pore size distributions are offset for clarity. All samples were calcined before the measurements.

The argon sorption isotherms of pristine ASNCs and Ti-ASNCs synthesized with the different processes and different Ti/Si ratios are of type IV (Figure 5.2). The structural data of co-condensed and post-condensed samples, reported in Table 5.1, are comparable in terms of pore volume, pore size and surface area. However, the ASNCs samples impregnated with the titanium alkoxide show a decrease of the pore volume and surface area.[5] During this process the TiO_2 is partially deposited and grafted on the internal surface confirming that the small secondary particles (Figure 5.1) are only a part of the TiO_2 formed during the reaction.

Table 5.1 Structural data of pristine ASNCs and Ti-ASNCs.

Samples	V_{tot} / cm^{3}g^{-1}	d_{DFT} / nm	S_{BET} / m^{2}g^{-1}	a_0 / nm
Pristine ASNCs	0.703	3.4	810	3.9
TiO_2-synthesized	0.077	2.8 - 50	29	-
Co-condensed 0.1	0.764	3.2	930	3.8
Co-condensed 0.3	0.761	3.3	919	3.8
Co-condensed 0.5	0.759	3.3	917	3.8
Impregnated 0.1	0.587	3.2	710	3.9
Impregnated 0.3	0.434	3.3	514	4.0
Impregnated 0.5	0.500	3.3	595	3.9
Post-condensed 0.1	0.737	3.3	868	3.9
Post-condensed 0.3	0.734	3.3	877	3.9
Post-condensed 0.5	0.766	3.4	911	3.8

Pure TiO_2 (TiO_2-synthesized) was synthesized using conditions for the preparation of ASNCs (TTIP instead of TEOS), in order to obtain more information about the particle morphology and the textural properties. The standard reaction parameters led to the formation of a stable sol. The solution was stirred until complete precipitation of the white TiO_2 powder. The sol stability is influenced by two factors. The first is the decreasing rate of condesation due to the low solution pH (4.4 M HCl solution) and the TTIP concentration (65 mM).[15-17] The second factor can be attributed to the formation of nanocrystals that are stable as dispersion.[17] These synthesis modifications affect strongly the morphology of the sample, creating large particles with an undefined shape. The isotherm and the relative pore size distibution of the TiO_2-synthesized is reported in Figure 5.3 and the structural parameters in Table 5.1. The type II isotherm, typical of macroporous and non-porous materials, can be interpreted as a curve of systems with low porosity. In fact, the pore volume and the surface area are lower than for the pristine ASNCs (Table 5.1) but the DFT graph (Figure 5.3) shows a broad pore size distribution that starts approximatively at 2.8 nm and continues above the mesoporous range (< 50 nm).

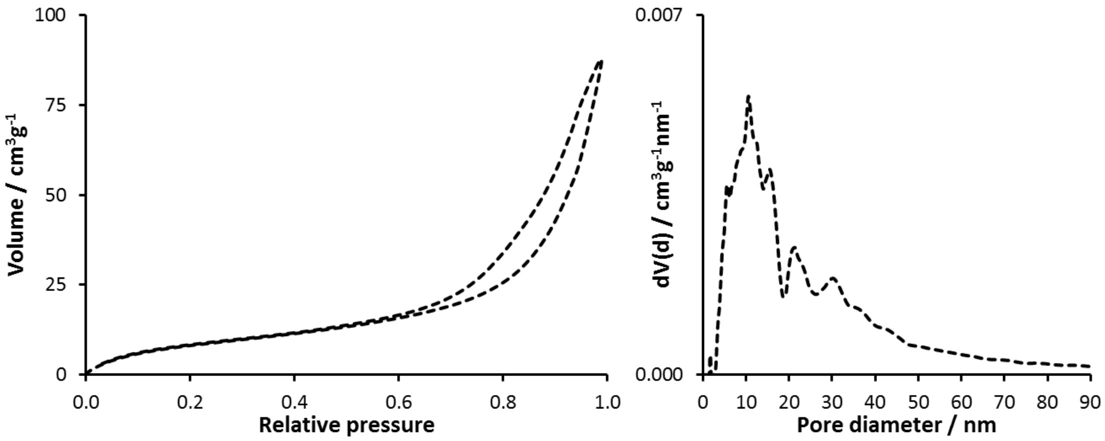

Figure 5.3 Argon sorption isotherm (left) and corresponding pore size distribution (right) of TiO_2 synthesized with the ASNCs reaction conditions.

X-ray diffraction was performed in the small and wide angle ranges to identify the ordered mesoporosity and crystallinity of the samples. Patterns of pristine ASNCs, TiO_2-synthesized and TiO_2-commercial are reported in Figure 5.4. In the small angle range (from 2 to 10°) only ASNCs particles show the typical 100, 110 and 200 peaks related to the hexagonal space group *P6mm*. In the wide angle range (from 10 to 70°), the patterns of TiO_2 samples show peaks related to anatase and rutile for the TiO_2-synthesized and anatase, rutile and brookite for the TiO_2-commercial. The typical broad peak of amorphous phases was found for ASNCs.

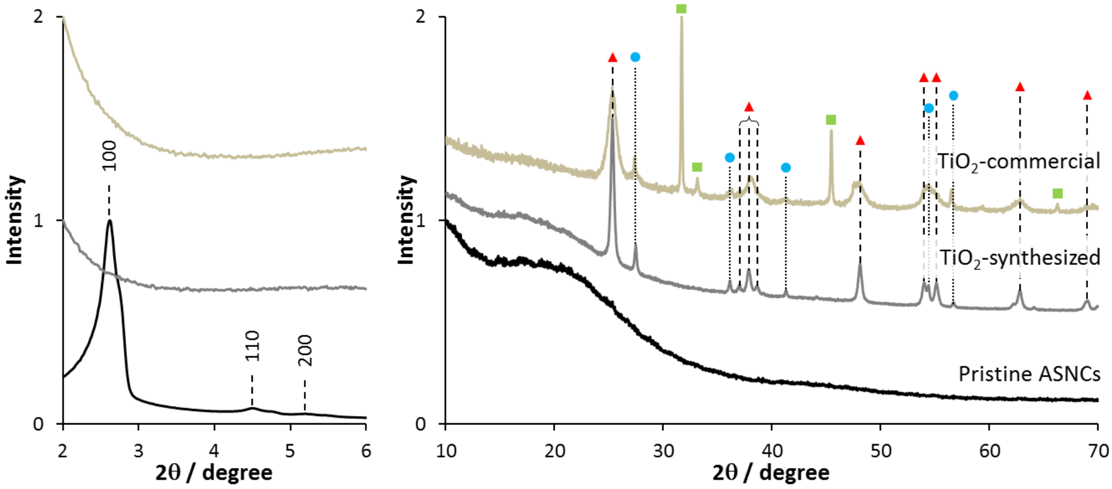

Figure 5.4 Left: Small Angle XRD patterns of pristine ASNCs, TiO_2-synthesized and TiO_2-commercial. Right: correspondent Wide Angle XRD patterns. The three TiO_2 crystalline phases are marked with red triangles (anatase), blue circles (rutile) and green squares (brookite). The patterns are normalized and offset for clarity.

All methods preserve the mesoporous order of ASNCs, showing the same peak found for the pristine ASNCs. For co-condensed Ti-ASNCs this result confirms further that the titanium alkoxide addition does not affect the ordered growth of the particles.

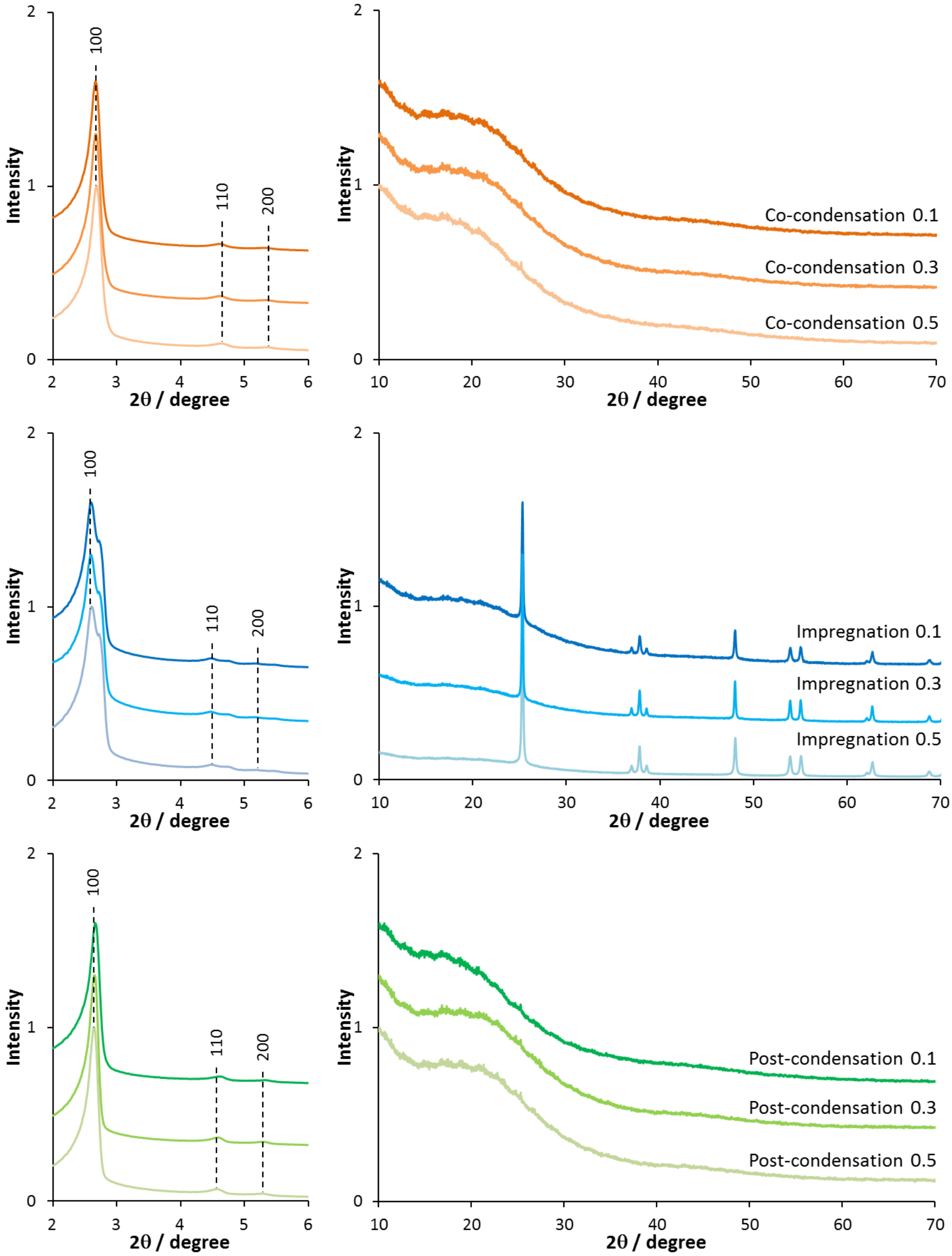

Figure 5.5 Left: Small Angle XRD patterns of Ti-ASNCs synthesized with three different methods: co-condensation, impregnation and post-condensation. Right: correspondent Wide Angle XRD patterns. The patterns are normalized and offset for clarity.

It should be noted that the multiple peaks (visible as shoulders of the indexed peaks) in the pristine ASNCs and in the impregnated Ti-ASNCs samples are attributed to the mixture of particles used to perform the impregnation process. The differences between the three functionalization processes are visible in the wide angle XRD. The patterns of Ti-ASNCs prepared with co-condensation and post-condensation methods show only the peak related to the amorphous framework. However, anatase reflections appear in the impregnated sample patterns. The absence of crystalline phases in the first two samples can be attributed to different factors. During the co-condensation the hydrolyzed titanium alkoxides react with the hydrolyzed silicon alkoxides forming a mixed homogeneous and amorphous framework. The delayed addition of the titania source, when the particle shape is reached (post-condensation), combines the effects of co-condensation and pure TiO_2 synthesis. The hydrolyzed TEOS residues react with the newly added alkoxides forming the amorphous framework. The slow condensation rate of the titanium species, depending on the solution pH and the Ti/Si ratio,[15-17] hinders the formation of crystalline structures on the particle surface. Differently from the TiO_2 synthesis, the reaction temperature was low (0 °C) and the particles were filtered leading to a removal of the nanocrystals. Furthermore, the amount of TiO_2 deposited and the heat treatment temperature (calcination at 550 °C) were not sufficient to induce crystallization.[17]

5.1.2 Framework composition

XRD showed the presence of amorphous species (co-condensate and post-condensate ASNCs) and crystalline TiO_2 (impregnated ASNCs), but this technique is not sufficient to confirm the formation of a new silica-titania framework. In order to obtain more information about the framework composition of Ti-ASNCs, wavelength dispersive X-ray fluorescence (WDXRF) measurements were performed. The samples were scanned at the typical 2θ angles of silicon (108.0° - 110.0°) and titanium (85.5° - 87.0°), using the same amount of powders and pristine ASNCs as control. In agreement with the experiments, the count intensities are comparable in the silicon scan range and they increase in the titanium scan range, when the Ti/Si ratio increases from 0.1 to 0.5 (Figure 5.6).

The impregnated Ti-ASNCs shows the maximum values, in terms of counts, confirming that the quantity of titanium, in this case TiO_2, is higher in the samples synthesized with the impregnation method. As expected, the titanium counts decrese for co-condensed and post-condensed particles. These results support the possible washing-out of TiO_2 colloids or nanocrystals due to the sol stability.

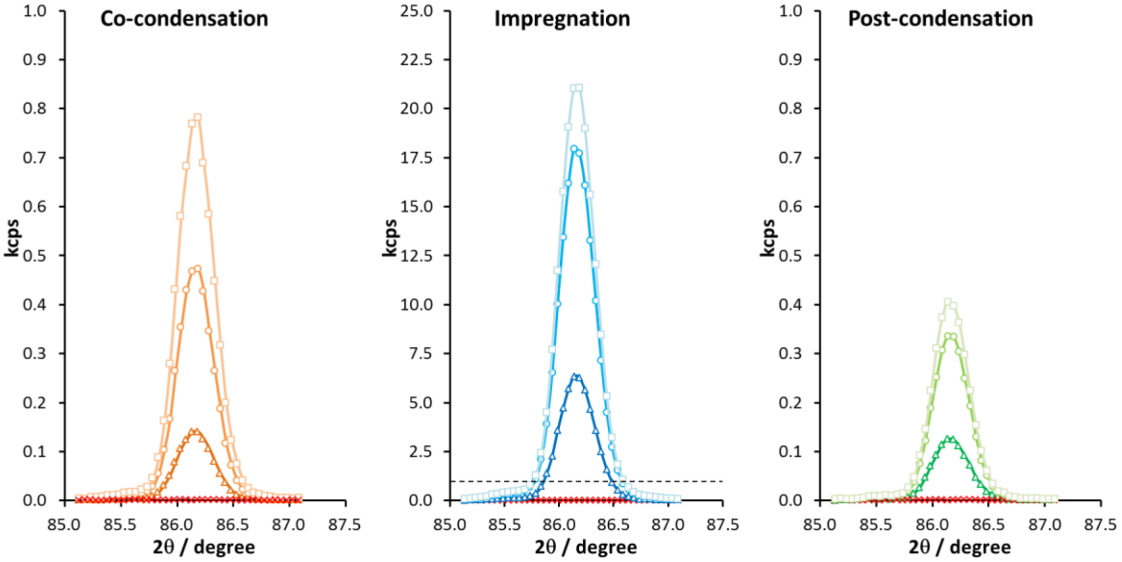

Figure 5.6 WDXRF scans of silica-titania particles synthesized with different methods and measured at the typical titanium angle. The Ti/Si ratio is 0.1 (triangles), 0.3 (circles) and 0.5 (squares). The scan of pristine ASNCs, as control, is reported in red. A dotted line, indicating 1 kcps, is shown in the impregnated Ti-ASNCs graph, to compare the scan intensities of the different synthetic methods.

Figure 5.7 shows the diffuse reflectance UV-visible spectra of samples with different content of titanium. Ti-ASNCs synthesized with co-condensation and post-conndensation show a band characteristic of mixed silica-titania frameworks.[18] A slight red shift and increasing absorbance were observed when the Ti/Si ratio increased from 0.1 to 0.5. In the spectra of impregnated samples, the broad absorption band shifts to longer wavelength and becomes similar to the sample TiO_2-synthesized. These changes indicate that the titanium atoms are not completely surrounded by silicon atoms (Ti-O-Si bonds) but exist as isolated TiO_2 domains.[15]

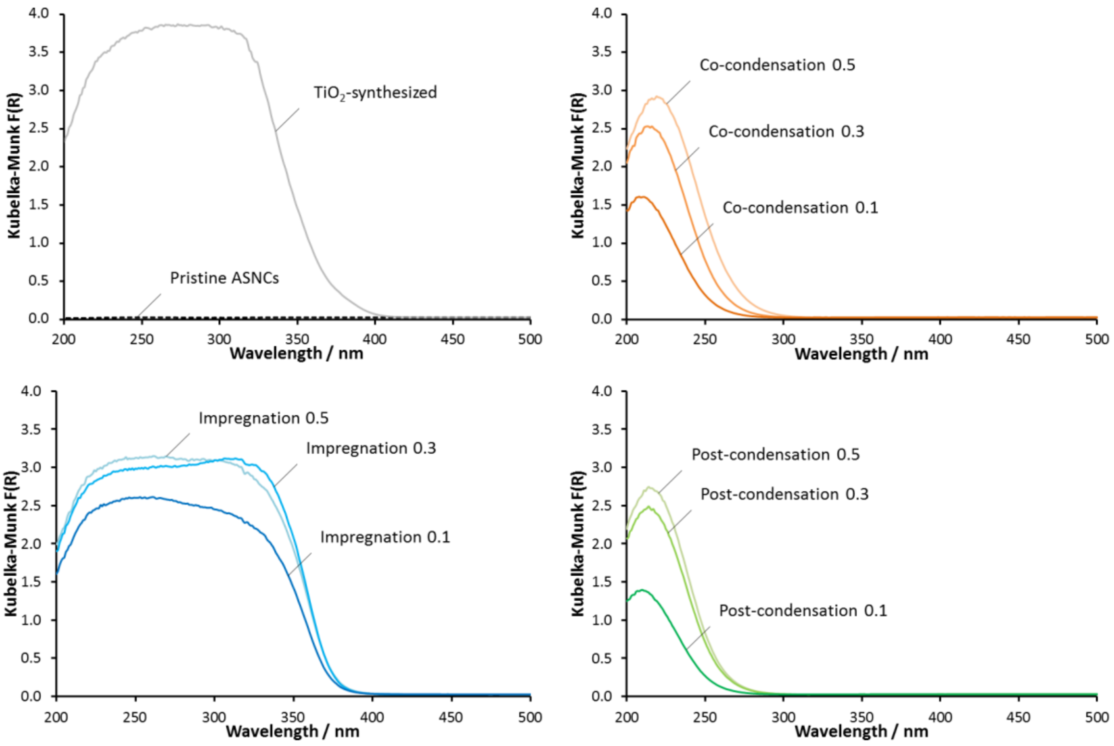

Figure 5.7 Diffuse reflectance UV-vis spectra of ASNCs, TiO_2-synthesized and silica-titania particles synthesized with different methods and with different Ti/Si ratios.

5.1.3 Photodegradation of methylene blue

The photocatalytic activity of the Ti-ASNCs samples was tested by measuring the degradation of methylene blue (MB) in aqueous solution. The experiments were conducted in two steps: the first in the dark (from 0 to 60 min) and the second with UV radiation (from 60 to 120 min, Figure 5.8). The blank solution of MB without catalyst (panel A, filled circles) showed no activity when exposed to UV radiation. TiO_2-commercial and TiO_2-synthesized exhibited different behaviors. When the UV lamp was switched on, the commercial titania started to degrade the dye and reached the plateau (maximum degradation) after 60 min (120th min, from 100% of dye to 7.5%). At contrary, the TiO_2-synthesized showed no activity, similar to the MB blank solution. Panels B, C and D of Figure 5.8 show the photodegradation results of Ti-ASNCs co-condensed, impregnated and post-condensed, respectively. The common characteristic of these silica-titania composites is the large adsorption capacity. After the first step in dark conditions, the Ti-ASNCs particles, as well as the pristine ASNCs (crosses and dotted line), adsorb the dye thereby decreasing the effective amount in solution before the photodegradation.[5] The values in percentage of the dye adsorbed and the sample surface areas are reported in Table 5.2. In an aqueous dispersion, the surface of silica and titania samples is covered by negative charges, in agreement with the respective isoelectric points (silica approximatively pH 2.2 and titania in a range of pH 5.0-6.8).[19] Methylene blue is a positively charged molecule leading to the electrostatic interactions between the Ti-ASNCs surfaces and the dye.

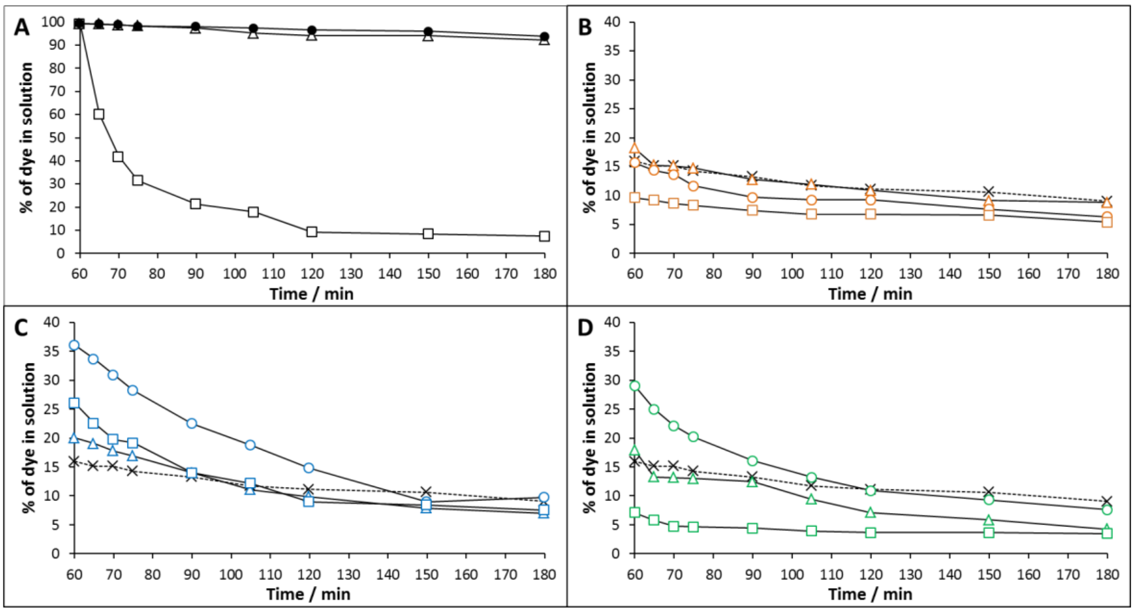

Figure 5.8 Photocatalytic degradation of MB in presence of particles with different compositions. The particles where added at the time t = 0 min and the UV lamp was switched on after 60 min of stirring. 100% represents the maximum absorbance of the starting dye solution (10 ppm). panel A: methylene blue as control (dye solution, filled circles), TiO_2-synthesized (empty triangles) and TiO_2-commercial (empty squares). panel B: co-condensed Ti-ASNCs. panel C: impregnated Ti-ASNCs. panel D: post-condensed Ti-ASNCs. Pristine ASNCs are reported to compare the slope of degradation (panels A, B and C, crosses and dotted line). The Ti-ASNCs samples were prepared with different Ti/Si ratios (0.1 (triangles), 0.3 (circles) and 0.5 (squares)).

Co-condensed Ti-ASNCs samples adsorb a high quantity of dye (82-90%) and are not efficient as photocatalyst, giving results comparable with the pristine ASNCs (panel B). Impregnated samples have the lowest surface areas (Table 5.2). As a consequence, the quantity of adsorbed dye is lower than for the other powders (64-80%). Furthermore the graph shows an interesting photodegradation activity, in particular for the sample prepared with a Ti/Si ratio of 0.3. The post-condensation of TTIP is different compared to the previous post-condensation experiments. Generally, the particle growth and the hindrance of the functionality are the crucial parts of the process. However, the titanium alkoxide builds the framework similar to TEOS and the hindrance does not affect the location of the TiO_2 domains. In contrast to the co-condensed samples the distribution of the functional (TiO_2)

domains is not homogeneous. These heterogeneous distributions of silica and titania are the possible explanation of the wide range of adsorbed dye (71-93%).

Table 5.2 Percentage of dye adsorbed related to the surface area.

Samples	Surface area* / m^2	Dye adsorbed
Pristine ASNCs	16.2	84%
TiO_2-synthesized	0.6	1%
Co-condensed 0.1	18.6	82%
Co-condensed 0.3	18.4	84%
Co-condensed 0.5	18.3	90%
Impregnated 0.1	14.2	80%
Impregnated 0.3	10.3	64%
Impregnated 0.5	11.9	74%
Post-condensed 0.1	17.4	82%
Post-condensed 0.3	17.5	71%
Post-condensed 0.5	18.2	93%

** The surface area was obtained by dividing the BET surface area (Table 5.1) by the amount of powder used (50 mg).*

As a consequence, the dye degradation at high Ti/Si ratio (0.5) is not efficient. When the titanium amount is less (Ti/Si ratios of 0.1 and 0.3), the results became comparable with the impregnated samples.

5.2 Conclusion

ASNCs containing titanium atoms (Ti-ASNCs) were synthesized with co-condensation, impregnation and post-condensation methods. The particle morphology was influenced by the method and the Ti/Si ratio. The particle length of co-condensed ASNCs increased with increasing amount of titania in agreement with the end-on growth process. Impregnated samples preserved their shape but spherical byproducts appeared. Deformed ASNCs and irregularly shaped byproducts were obtained using the post-condensation method. Titanium dioxide synthesized with the ASNCs reaction parameters led to shapeless agglomerates.

Argon sorption measurements of Ti-ASNCs showed a high surface area, large pore volume and a pore size distribution centered between 3.2 to 3.4 nm. As expected, the impregnation method caused a slight decrease of the surface area and pore volume due to the formation of titania domains inside the nanochannels. TiO_2-synthesized can be considered a non-porous material. Small angle XRD analyses confirmed the ordered hexagonal mesoporous domains (*P6mm*) for all Ti-ASNCs samples. Crystalline TiO_2 phases were detected for impregnated particles (anatase) and for TiO_2-synthesized (anatase and rutile). Co-condensed and post-condensed Ti-ASNCs showed only the broad peak related to amorphous titania. XRF and diffuse reflectance UV-vis experiments were performed to obtain more information about the silica-titania framework. The results confirmed the presence of TiO_2 domains. The dispersion of the Ti-ASNCs in an aqueous dye solution revealed the high affinity between the silica-titania particles and the positively charged dye. The photoactivity test showed a significant dye degradation for the impregnated samples and for the post-condensed sample prepared with Ti/Si = 0.3.

5.3 Experimental

5.3.1 Materials

Hexadecyltrimethylammonium bromide (CTAB, for molecular biology, ≥99%), $CaCl_2$ (≥97.0%), concentrated hydrochloric acid (puriss. p.a., ≥32%), (NaOH, ≥98%), tetraethoxysilane (TEOS, 99.999%), methylene blue (puriss.), titanium(IV) isopropoxide (TTIP, 97%) and ethanol (purum, ≥99.8%) were obtained from Sigma-Aldrich. All chemicals were used as received.

5.3.2 Synthesis of co-condensed Ti-ASNCs

CTAB (4.0 g, 11 mmol) and $CaCl_2$ (1.50 g, 13.5 mmol) were dissolved in a mixture of doubly distilled H_2O (76 mL, 4.2 mol) and concentrated hydrochloric acid (≥32%, 60 mL, 0.62 mol) by stirring for 15 min in a polypropylene beaker. The solution was subsequently cooled in an ice bath for 15 min under quiescent conditions, followed by the slow addition of cold TEOS (4 °C, 2.0 mL, 9 mmol) and cold TTIP (4 °C, Ti/Si molar ratio = 0.1, 0.3 and 0.5) and further stirring for 30 s. The resulting mixture was kept at 0 °C under quiescent conditions for 4 h. For all samples, the structure-directing agent was removed by first heating at 300 °C for 2 h and subsequent calcination in air at 550 °C for 12 h. Heating rates of 2 °C min^{-1} were applied.

5.3.3 Synthesis of post-condensed Ti-ASNCs

CTAB (4.0 g, 11 mmol) and $CaCl_2$ (1.50 g, 13.5 mmol) were dissolved in a mixture of doubly distilled H_2O (76 mL, 4.2 mol) and concentrated hydrochloric acid (≥32%, 60 mL, 0.62 mol) by stirring for 15 min in a polypropylene beaker. The solution was subsequently cooled in an ice bath for 15 min under quiescent conditions, followed by the slow addition of cold TEOS (4 °C, 2.0 mL, 9 mmol) and further stirring for 30 s. The resulting mixture was kept at 0 °C under quiescent conditions for 3 h. After this period, the solution was stirred for 1 min while adding the desired amount of TTIP (4 °C, Ti/Si molar ratio = 0.1, 0.3 and 0.5) and subsequently kept at 0 °C under quiescent conditions for 1 h. The product was filtered off and dried at 80 °C. For all samples, the structure-directing agent was removed by first heating at 300 °C for 2 h and subsequent calcination in air at 550 °C for 12 h. Heating rates of 2 °C min^{-1} were applied.

5.3.4 Synthesis of impregnated Ti-ASNCs

An amount of TTIP (Ti/Si molar ratio = 0.1, 0.3 and 0.5, the ASNCs were approximated as pure SiO_2 in the calculation of the molecular weight) was dissolved in 20 mL of ethanol and ASNCs (300 mg) were dispersed in this solution. The mixture was agitated at room temperature until the complete evaporation of the solvent. The samples were calcined by first heating at 300 °C for 2 h and subsequent calcination in air at 550 °C for 12 h. Heating rates of 2 °C min^{-1} were applied.

5.3.5 Synthesis of TiO_2 under the ASNCs synthesis conditions

CTAB (4.0 g, 11 mmol) and $CaCl_2$ (1.50 g, 13.5 mmol) were dissolved in a mixture of doubly distilled H_2O (76 mL, 4.2 mol) and concentrated hydrochloric acid (≥32%, 60 mL, 0.62 mol) by stirring for 30 min in a polypropylene beaker. TTIP (2.65 mL, 9 mmol) was slowly added to the solution under stirring. The mixture was agitated at room temperature until the complete evaporation of the solvents (more than 7 days). The samples were collected and calcined by first heating at 300 °C for 2 h and subsequent calcination in air at 550 °C for 12 h. Heating rates of 2 °C min^{-1} were applied.

5.3.6 Photodegradation of methylene blue

Ti-ASNCs particles (50 mg) were mixed with a methylene blue aqueous solution (300 mL, 0.03 M) in a glass photo-reactor. The solution was stirred (300 rpm) and the UV lamp assembled and dipped in the solution. The apparatus was covered with aluminum foil to prevent the UV-light dispersion for the operator safety. After 60 min the first sample was collected (the adsorbed dye percentage was calculated with these samples) and the lamp was switched on. The solution samples (approx. 3 mL) were collected at 5, 10, 15, 30, 45, 60, 90 and 120 min. After centrifugation and transfer into cuvettes, the absorbance was measured. The spectra were collected in the range from 550 to 700 nm and the maximum absorbance (665 nm) was used for the calculations.

5.3.7 Physical measurements

Argon sorption isotherms were measured at 87.3 K with a Quantachrome Autosorb iQ MP equipped with a CryoCooler. Pore size distributions and average pore diameters d_{DFT} were determined from the adsorption isotherms by a non-local density functional theory (NLDFT) model developed for silica exhibiting cylindrical pore geometry (Software ASiQwin v3.01, Quantachrome Instruments).[20] Scanning electron microscopy (SEM) images were obtained with an FEI Phenom Pro. Powder X-ray diffraction (XRD) patterns were recorded on a STOE STADI P diffractometer with CuKα_1 radiation. Wavelength dispersive X-ray fluorescence (WDXRF) scans were collected with a Thermo Advant XP, Sequential XRF. UV-vis diffuse reflectance spectra were obtained with a PerkinElmer Lambda 650 spectrometer equipped with an integrating sphere (150 mm diameter, with gloss trap). UV-vis solution spectra were collected with a PerkinElmer Lambda 950 spectrometer.

5.4 References

1. X. Qisn, K. Fuku, Y. Kuwahara, T. Kamegawa, K. Mori and H. Yamashita, Chem. Sus. Chem., 2014, 7, 1528-1536.
2. D. M. Tobaldi, R. C. Pullar, C. Piccirillo, P. M. L. Castro, M. M. Pintado, M. P. Seabra and J. A. Labrincha, Handbook of Functional Nanomaterials, 2014, 4, 69-91.
3. C. M. The and A. M. Rahman, Journal of Alloys and Compounds, 2011, 509, 1648-1660.
4. Z. Luan, E. M. Maes, P. A. W. van der Heide, D. Zhao, R. S. Czernuszewicz and L. Kevan, Chem. Mater., 1999, 11, 3680-3686.
5. A. A. Belhekar, S. V. Awate and R. Anand, Cat. Comm., 2002, 3, 453-458.
6. M. Signoretto, E. Ghedini, V. Trevisan, C. L. Bianchi, M. Ongaro and G. Cruciani, Appl. Catal. B, 2010, 95, 130-136.
7. W. Wang and M. Song, Microporous Mesoporous Mater., 2006, 96, 255-261.
8. S. Perathoner, P. Lanzafame, R. Passalacqua, G. Centi, R. Schlögl and D. S. Su, Microporous Mesoporous Mater., 2006, 90, 347-361.
9. K. De Witte, A. M. Busuioc, V. Meynen, M. Mertens, N. Bilba, G. Van Tendeloo, P. Cool and E. F. Vansant, Microporous Mesoporous Mater., 2008, 110, 100-110.
10. W. Dong, Y. Sun, C. W. Lee, W. Hua, X. Lu, Y. Shi, S. Zhang, J. Chen and D. Zhao, J. Am. Chem. Soc., 2007, 129, 13894-13904.
11. N. Zucchetto and D. Brühwiler, RSC Adv., 2015, 5, 74638-74644.
12. H. Ritter and D. Brühwiler, J. Phys. Chem. C, 2009, 113, 10667-106744.
13. N. Gartmann and D. Brühwiler, Angew. Chem. Int. Ed., 2009, 48, 6354-6356.
14. N. Zucchetto and D. Brühwiler, Dalton Trans., 2016, 45, 14363-14369.
15. H. Zhu, Z. Pan, B. Chen, B. Lee, S. M. Mahurin, S. H. Overbury and S. Dai, J. Phys. Chem. B, 2004, 108, 20038-20044.
16. M. Burgos and >M. Langlet, J. Sol-Gel Sci. Technol., 1999, 16, 267-276.
17. S. A. Ibrahim and S. Sreekantan, Adv. Mater. Res., 2011, 173, 184-189.
18. L. Marchese, T. Maschmeyer, E. Gianotti, S. Coluccia and J. M. Thomas, J. Phys. Chem. B, 1997, 101, 8836-8838.
19. C. Su, B.-Y. Hong and C.-M. Tseng, Catal. Today, 2004, 96, 119-126.
20. J. Landers, G. Y. Gor and A. V. Neimark, Colloids Surf. A, 2013, 437, 3-32.

6. MESOPOROUS SILICA MONOLAYERS

The assembly of ordered mesoporous particles on a substrate via covalent linkers is of great interest for various applications. A well-aligned monolayer of particles can be used as efficient catalyst support, as molecular sieves and as host for drug delivery and sensing. Homogeneous monolayers of zeolite crystals were realized by physical adsorption or by introducing covalent bonds between particles and the substrate.[1-9] Different techniques were used to fabricate silica particle monolayers. Dip coating and spin coating methods, electrophoretic deposition, capillarity immersion force and Langmuir-Blodgett techniques are methods to achieve this result.[9] As mentioned previously, ASNCs can be considered as the mesoporous analogue to hexagonal zeolites such as zeolite L. The great variety of molecular linkers and the possibility to selectively functionalize the various surfaces (external and pore entrances) has focused our attention towards the particle-substrate covalent bond method.

6.1 Preliminary grafting tests

The ester functional group, characteristic of poly(methyl methacrylate) (PMMA), is a perfect starting point for the grafting process.[4-6] PMMA is soluble in many organic solvents, therefore in order to prevent the dissolution, mild reaction conditions are necessary. Procedures to graft zeolites on glass typically use a functional silane as linker[1-3,7-9] and toluene as a solvent.

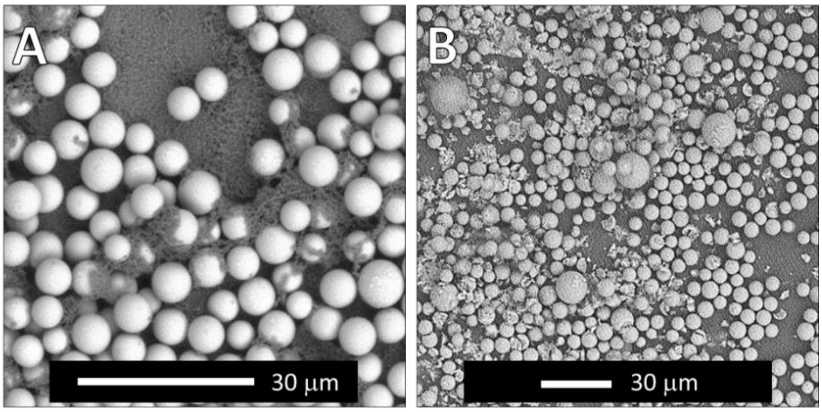

Figure 6.1 SEM pictures of Kromasil grafting experiments with GLYMO (panel A) and with APTMS (panel B) performed in ethanol.

Experiments performed with 3-aminopropyltrimethoxysilane (APTMS) and 3-glycidyloxypropyl trimethoxysilane (GLYMO) in ethanol and Kromasil as model silica particles led to the formation of a discontinuous monolayer with the presence of byproducts attributed to the auto-condensation of the silanes as shown in Figure 6.1. Another problem of this technique is the deformation of the polymeric substrate after hours in ethanol. In order to obtain a particle monolayer, three different methods were evaluated using Kromasil and ASNCs particles as mesoporous silica samples.

6.2 Single side treatment

A custom-made setup was used to treat only one side of the PMMA plates (Figure 6.2). The circle shaped substrate was fixed by an O-ring to the cap of a 50 mL falcon tube and sealed with the silica particle dispersion. When the tube is turned, only one face of the substrate is in contact with the dispersion.

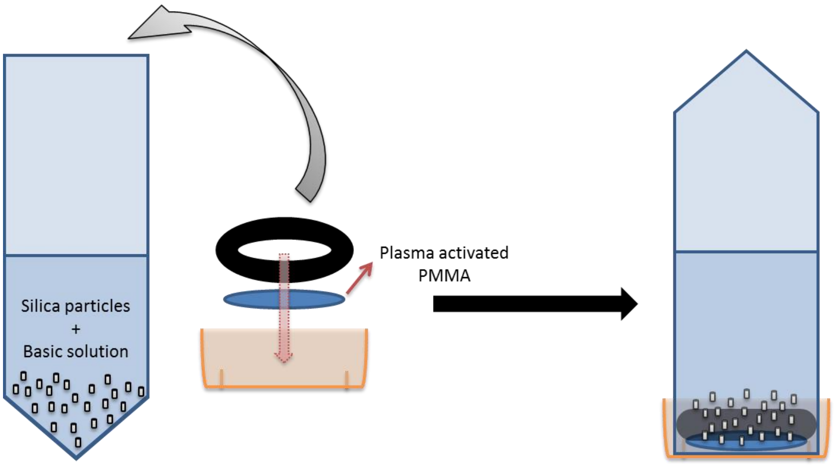

Figure 6.2 Scheme of the setup for the single side PMMA treatment.

The parameters considered for these experiments were: particle functionalization, solvent, time, plasma treatment and sonication. The Kromasil and ASNCs particles were amino functionalized with TMPTA and dispersed in a basic aqueous solution. The idea was to promote the coupling between the ester and the amino functions for creating a stable peptide bond.[4-6] Cold plasma treatment helped to activate the polymeric surface with the formation of reactive OH groups[10] and the sonication procedure to homogenously disperse the silica particles on the substrate surface. The washing procedure was standardized to verify the efficiency of the grafting technique. The treated plates were immersed in ethanol and sonicated for 15 seconds in order to remove the physisorbed particles. The limit of this method was the time of contact between the basic solution and the PMMA. Experiments performed with prolonged times (overnight) led to cracks on the PMMA surface.

6.2.1 Deposition

The first single side treatment was performed using an aqueous basic solution and the custom-made setup described previously.

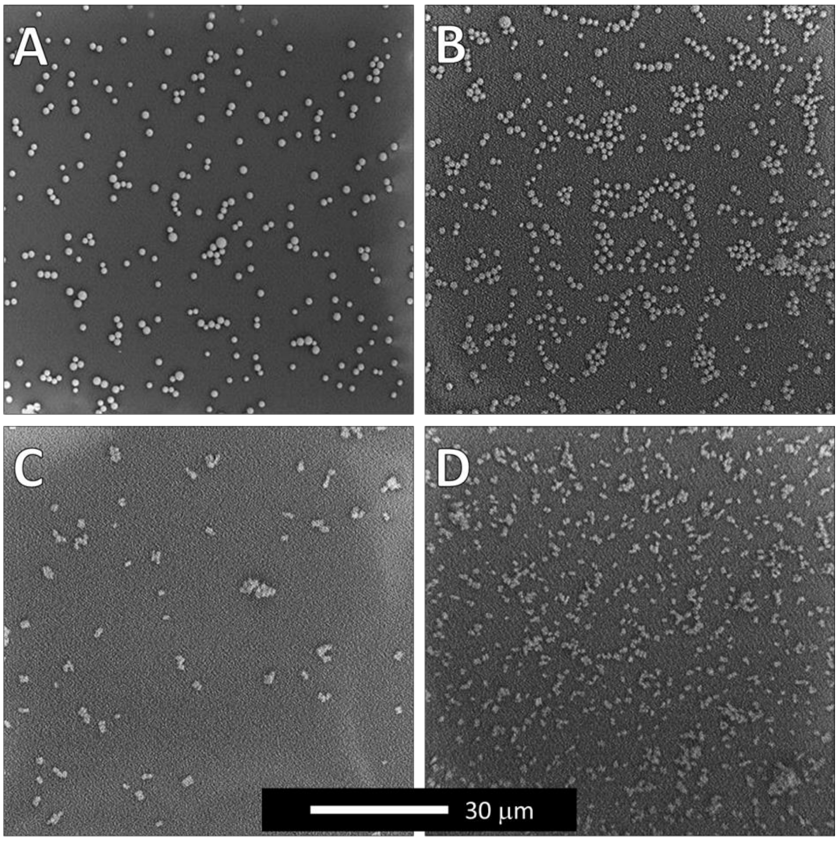

Figure 6.3 SEM pictures of amino functionalized samples deposited on plasma activated PMMA. Kromasil and ASNCs deposited with sonication (panel A and C, respectively) and without sonication (panel B and D, respectively) in basic aqueous solution.

The particle dispersion is influenced by sonication as shown in Figure 6.3. The fast particle movement does not support the formation of an uniform monolayer (panels A and C), instead the quiescent conditions support the formation of a bond between silica and substrate (panels B and D).

6.2.2 Solvent evaporation

The deposition method limit is the prolonged time of substrate immersion. Slow solvent evaporation leads to a multilayer on the polymer surface that can be washed off in a second step to obtain a particle layer.

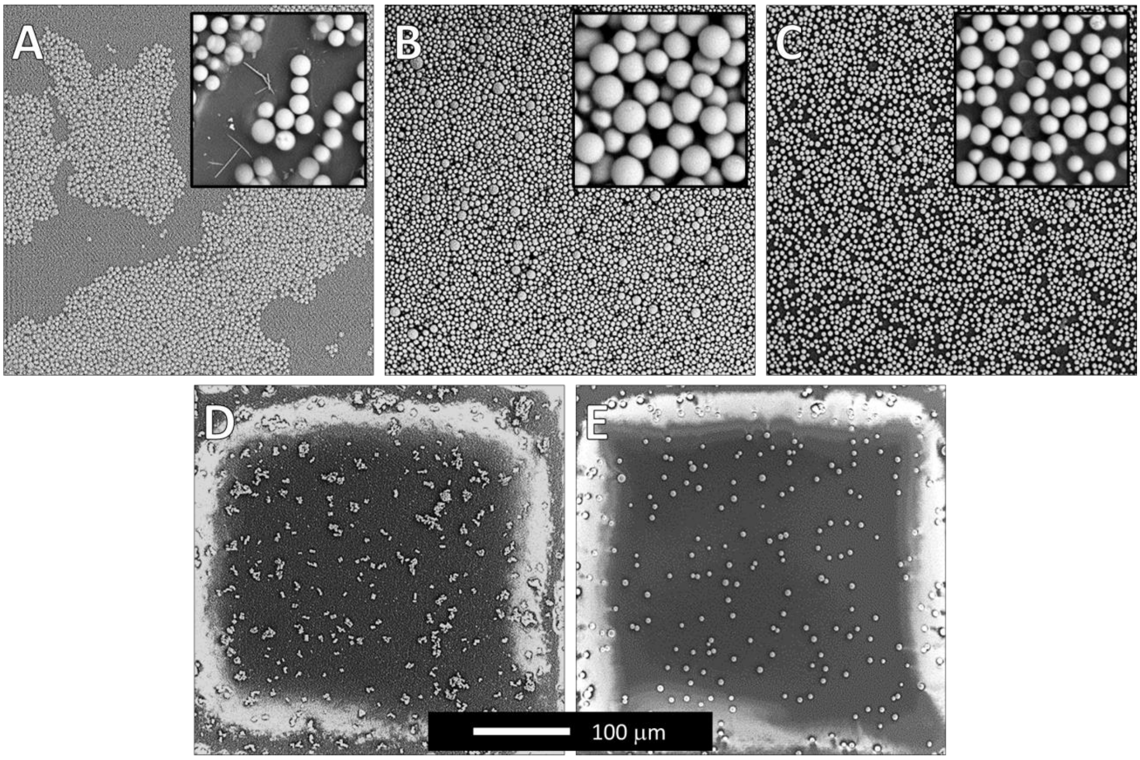

Figure 6.4 SEM pictures of amino functionalized samples deposited after solvent evaporation on plasma activated PMMA. Kromasil deposited after evaporation of a NaOH solution overnight (panel A), Kromasil deposited after isopropanol evaporation overnight without and with partial sonication (panels B and C, respectively), ASNCs deposited after isopropanol evaporation overnight (panel D) and Kromasil deposited after isopropanol evaporation for 2 hours (panel E).

The dispersion in basic aqueous medium leads to a non-uniform deposition. This result is attributed to the poor interactions between water and the substrate. Before the covalent bond formation, the water creates separated monolayer areas. Furthermore after washing there is still the presence of NaOH crystals as shown in Figure 6.4, panel A. The time of evaporation and the particles/substrate contact is a critical point when the solvent used was isopropanol. Comparing the panels B-C and E in Figure 6.4 reveals that the evaporation achieved in 2 hours is not sufficient to bind the functionalized particles onto the PMMA surface. Experiments conducted with drying temperature higher than room temperature (35 °C and 45 °C) led to a deformation of the substrate creating visible cracks. A homogeneous monolayer was obtained with Kromasil particles after an overnight evaporation of isopropanol. The short sonication (1 hour) before the quiet period of drying improves the particle distribution solving the partial agglomeration problem reported in panel B (Figure 6.4). Differently from Kromasil, experiments conducted with ASNCs did not show high density monolayers (panel D).

6.2.3 Drop method

The last strategy developed to graft the particles on the PMMA surface was the partial surface dissolution of the polymer by a drop of solvent. Kromasil and ASNCs were dispersed in different solvents and deposited on the polymer surface until complete evaporation.

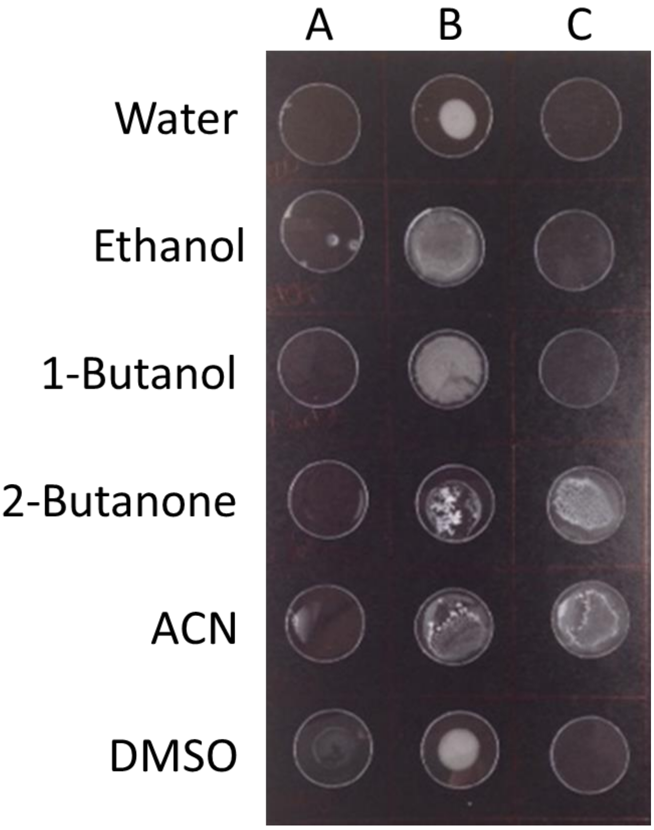

Figure 6.5 Solvent screening. The columns represent: the solvent effect on the PMMA surface (A), the dispersion of the particles (B) and the grafting result after washing (C).

The solvent screening reported in Figure 6.5 shows that the PMMA surface is not affected by superficial dissolution caused by the pure solvent (Column A). The dispersion is optimal when an alcohol is used (Column B) but only with acetonitrile and 2-butanone it was possible to obtain a particle layer (Column C).

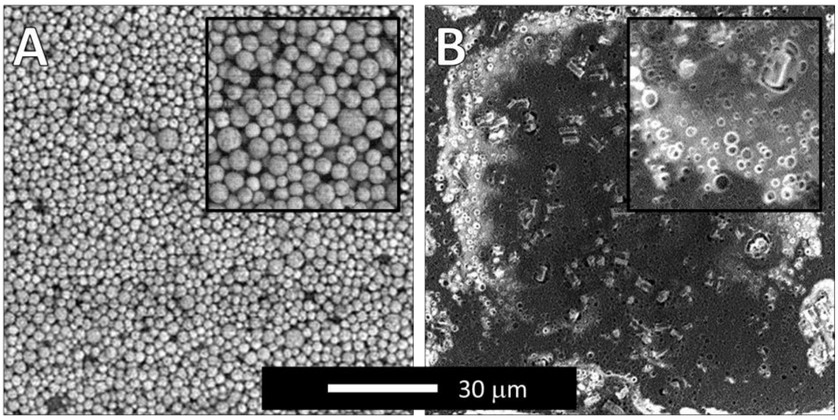

Figure 6.6 SEM pictures of Kromasil and ASNCs layers after drop deposition with 2-butanone (panel A and B, respectively).

The results obtained with 2-butanone are reported in Figure 6.6. The coating obtained with Kromasil shows good particle dispersion but not a monolayer. Increasing the time of sonication during the washing step did not change the result. The ketone rapidly dissolves the polymer surface then locks (freezes) the particle layers (panel A). A different result was obtained with ASNCs particles (panel B). In fact the solvent dissolves the surface creating holes (panel B enlargement) but it does not trap the particles.

6.3 Conclusion

The formation of a mesoporous silica monolayer is challenging due to the particle properties and the nature of the substrate. Preliminary tests with functional silanes as linker showed the formation of secondary particles and non-uniform layers. Furthermore, the prolonged immersion of the substrate (PMMA) in ethanol caused the deformation of the PMMA discs. A custom-made apparatus was used in order to prevent the substrate deformation and obtain a single side monolayer. Three different approaches were tested with the single side method: deposition, solvent evaporation and solvent drop. Deposition of functionalized particles was performed in basic aqueous conditions to favor the formation of covalent bonds between the amino functionalized silica and the substrate methacrylate groups. It was observed that the sonication decreases the formation of a dense particle monolayer. The solvent evaporation performed with isopropanol resulted in a homogeneous particle monolayer when Kromasil was used. At contrary, the same method applied with ASNCs did not give good results due to the agglomeration of the silica particles. Dispersing mesoporous particles in 2-butanone and dropping the mixture on the substrate led to layers of particles. During this process the PMMA surface was dissolved and the mesoporous particles were fused into the polymeric matrix.

6.4 Experimental

6.4.1 Materials

Sodium hydroxide (NaOH, ≥98%), N1-(3-trimethoxysilylpropyl)diethylenetriamine (TMPTA, technical grade), (3-glycidyloxypropyl)trimethoxysilane (GLYMO, ≥98%) and the solvents ethanol (puriss.), isopropanol (anhydrous, 99.5%), 1-butanol (anhydrous, 99.8%), 2-butanone (ACS reagent, ≥99.0%), acetonitrile (ACN, anhydrous, 99.8%) and dimethyl sulfoxide (DMSO, for molecular biology) were obtained from Sigma-Aldrich. The poly(methyl methacrylate) film (PLEXIGLAS® Film, Clear, 0.375 mm) was obtained from Evonik. All chemicals were used as received.

6.4.2 GLYMO-functionalized particles

Kromasil (100 mg) was dispersed in ethanol (10 mL) and sonicated for 5 min. GLYMO (100 μL) or TMPTA (100 μL) was added and the dispersion was stirred for 15 min. The PMMA disc was dipped in the dispersion and sonicated for 15 min. The substrate was removed from the container, put in ethanol (10 mL) and sonicated for 10-15 s to remove the physisorbed particles. The disc was washed twice with ethanol (5 mL) and dried at room temperature.

6.4.3 Deposition

Amino functionalized silica (10 mg) was dispersed in a NaOH solution (0.1 M, 5 mL) and sonicated for 5 min. The PMMA surface was activated by cold plasma treatment (2 min, 50 W) and subsequently the substrate was fixed at the bottom of a closed and tight container to guarantee the deposition only on the activated side. The silica dispersion was added and the container was sonicated for 1 h. Subsequently the substrate was removed from the container, put in ethanol (10 mL) and sonicated for 10-15 s to remove the physisorbed particles. The disc was washed twice with ethanol (5 mL) and dried at room temperature.

6.4.4 Solvent evaporation

Amino functionalized silica (10 mg) was dispersed in isopropanol (1 mL) or in a NaOH solution (0.1 M, 1 mL) and sonicated for 5 min. The PMMA surface was activated by cold plasma treatment (2 min, 50 W) and subsequently the substrate was fixed at the bottom of an open and tight container to guarantee the deposition only on the activated side. The silica dispersion was added and the container was left open overnight. A dry particle coating was formed on the PMMA disc. The substrate was removed from the container, put in ethanol (10 mL) and sonicated for 10-15 s to remove the physisorbed particles. The disc was washed twice with ethanol (5 mL) and dried at room temperature.

6.4.5 Drop method

Amino functionalized silica (10 mg) was dispersed in 2-butanone (1 mL) and sonicated for 5 min. The PMMA surface was activated by cold plasma treatment (2 min, 50 W) and subsequently a drop of dispersion (20 μL) was deposited on the substrate. After complete solvent evaporation a dry particle coating was formed on the PMMA disc. The substrate was washed with ethanol (10 mL) and sonicated for 10-15 s to remove the physisorbed particles. The disc was washed twice with ethanol (5 mL) and dried at room temperature.

6.4.6 Characterization

Scanning electron microscopy (SEM) images were obtained with an FEI Phenom Pro.

6.5 References

1. A. Zabala Ruiz, H. Li and G. Calzaferri, Angew. Chem., Int. Ed., 2006, 45, 5282-5287.
2. J. S. Lee, H. Lim, K. Ha, H. Cheong and K. B. Yoon, Angew. Chem., Int. Ed., 2006, 45, 5288-5292.
3. Z. Popović, M. Busby, S. Huber, G. Calzaferri and L. De Cola, Angew. Chem., Int. Ed., 2007, 46, 8898-8902.
4. A. C. Henry, T. J. Tutt, M. Galloway, Y. Y. Davison, C. S. Mcwhorter, S. A. Soper and R. L. McCarley, Anal. Chem., 2000, 72, 5331-5337.
5. K. Kim, S. W. Park and S. S. Yang, BioChip J., 2010, 4, 148-154.
6. L. Brown, T. Koerner, J. H. Horton and R. D. Oleschuk, Lab Chip, 2006, 6, 66-73.
7. K. Ha, Y.-J. Lee, H. J. Lee and K. B. Yoon, Adv. Mater., 2006, 12, 1114-1117.
8. J. S. Lee, K. Ha, Y.-J. Lee and K. B. Yoon, Adv. Mater., 2005, 17, 837-841.
9. Y. Wang, H. Li, B. Liu, Q. Gan, Q. Dong, G. Calzaferri and Z. Sun, J. Solid Chem., 2008, 181, 2469-2472.
10. C. Lantano, N. Zucchetto, A. Montenero, C. Corradini, A. Lorenzi and I. Alfieri, J. Food Eng., 2013, 119, 580-587.

7. PSEUDOMORPHIC TRANSFORMATION OF SBA-15 AND SBA-16

The pseudomorphic transformation of mesoporous silica particles in the presence of a SDA is governed by the processes of dissolution and precipitation. The rate of dissolution/precipitation thereby depends on various parameters, including pH, temperature, and solvent.[1,2] The particle morphology remains intact upon transformation, whereas the pore structure can undergo a rearrangement. Figure 7.1 compares SEM images of SBA-15 and SBA-16 before and after pseudomorphic transformation. The agglomerated submicrometer-sized primary SBA-15 particles are retained upon transformation, whereas the transformed SBA-16 sample features the typical micrometer-sized cubic particles of the parent SBA-16.

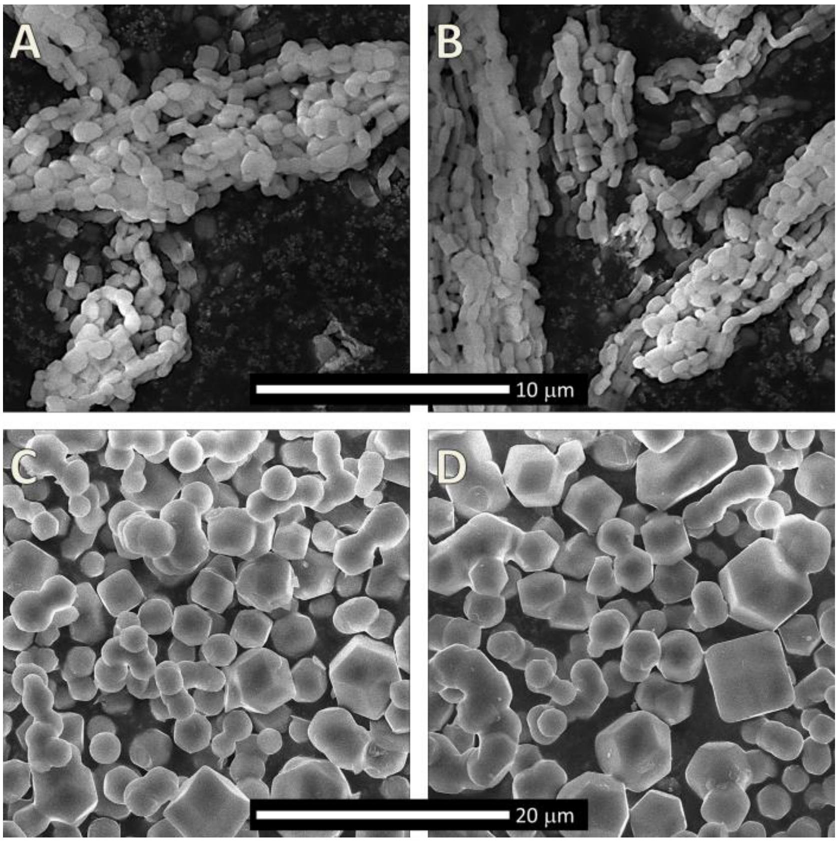

Figure 7.1 SEM images of parent SBA-15 (A), SBA-15 T3 (B), parent SBA-16 (C), and SBA-16 T3 (D). Note the unaltered particle morphology after transformation.

The dissolution and reprecipitation of the silicate species at high pH generates a modified pore structure with a reduced pore diameter, the value of which is determined by the SDA.[3] Starting with SBA-15 or SBA-16 parent materials and adjusting the silica/NaOH ratio, we have investigated three degrees of pseudomorphic transformation, namely a low (T1), intermediate (T2), and high degree (T3) of transformation. Argon sorption and SAXS were used to analyze the structural changes upon transformation. Key properties of the samples under investigation are summarized in Tables 7.1 and 7.2.

Table 7.1. Argon sorption and SAXS data of SBA-15 and transformed materials. The data of a mechanical mixture of SBA-15 and MCM-41 are shown for comparison.

Sample	**d_{DFT} / nm**	**V_{tot} / cm^3 g^{-1}**	**a_0 (*) / nm**	**a_0 (**) / nm**	**m_{silica} / m_{NaOH}**
SBA-15	7.1	0.68	10.3	–	–
SBA-15 T1	6.6, 4.0	0.66	10.1	–	15
SBA-15 T2	6.1, 4.1	0.46	9.8	–	12
SBA-15 T3	4.0	0.63	9.7	4.3	6
SBA-15/MCM-41	7.1, 3.7	0.61	10.3	4.3	–

**large a_0*
***small a_0*

A prerequisite for a pseudomorphic transformation in the presence of a SDA, is the introduction of the SDA into the pores of the parent material. The sorption isotherms shown in Figure 7.2 were measured before the hydrothermal treatment of the samples, i.e., after stirring of the parent materials in an alkaline aqueous solution of CTAB for 30 min.

Table 7.2. Argon sorption and SAXS data of SBA-16 and transformed materials. The data of a mechanical mixture of SBA-16 and MCM-41 are shown for comparison.

Sample	**d_{DFT} / nm**	**V_{tot} / cm^3 g^{-1}**	**a_0 (*) / nm**	**a_0 (**) / nm**	**m_{silica} / m_{NaOH}**
SBA-16	6.2	0.70	13.4	–	–
SBA-16 T1	6.4, 4.6	0.44	13.2	–	13
SBA-16 T2	5.5, 3.8	0.50	13.0	–	11
SBA-16 T3	4.0	0.48	13.0	5.2	9
SBA-16/MCM-41	6.2, 3.8	0.26	13.4	4.4	–

**large a_0*
***small a_0*

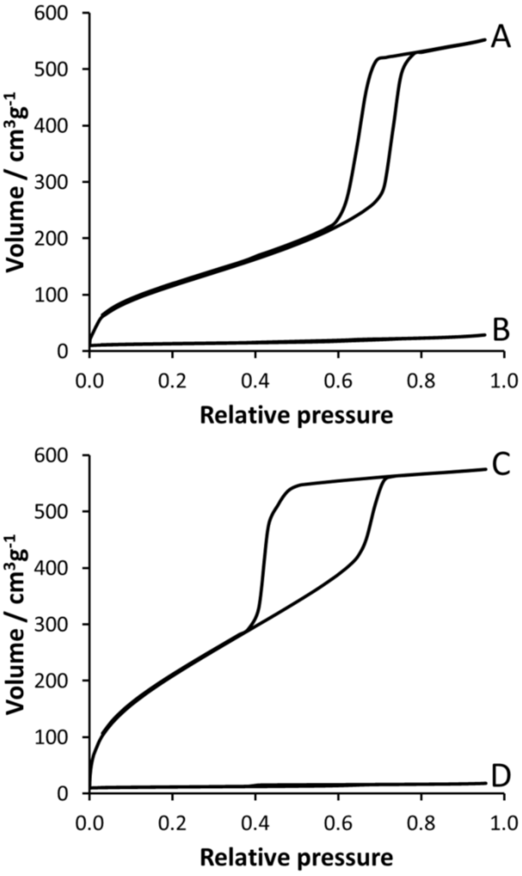

Figure 7.2 Top: Argon sorption isotherms of SBA-15 before (A) and after (B) uptake of SDA. Bottom: Argon sorption isotherms of SBA-16 before (C) and after (D) uptake of SDA.

Comparison with the respective untreated parent materials reveals a significantly reduced argon sorption capacity due to the presence of the SDA in the pores.

7.1 Transformation of SBA-15

Particles with two well-defined mesopore domains can be prepared by a partial pseudomorphic transformation of SBA-15.[4]

7.1.1 Argon sorption measurements

Argon sorption isotherms of the SBA-15 parent material and of the pseudomorphically transformed materials with various degrees of transformation are shown in Figure 7.3. As expected, the parent SBA-15 shows a H1 hysteresis[5] and a relatively narrow pore size distribution centered at 7.1 nm. A tail extending to 3.5 nm is indicative of the small intrawall mesopores that are created by the hydrophilic poly(ethylene oxide) segments of the non-ionic block copolymer SDA during hydrothermal treatment.[6,7] After transformation in the presence of CTAB, a second pore condensation step appears in the adsorption isotherm at lower relative pressure ($p/p_0 = 0.38$). This additional pore condensation step is caused by the newly formed domains with an average pore size of 4 nm.

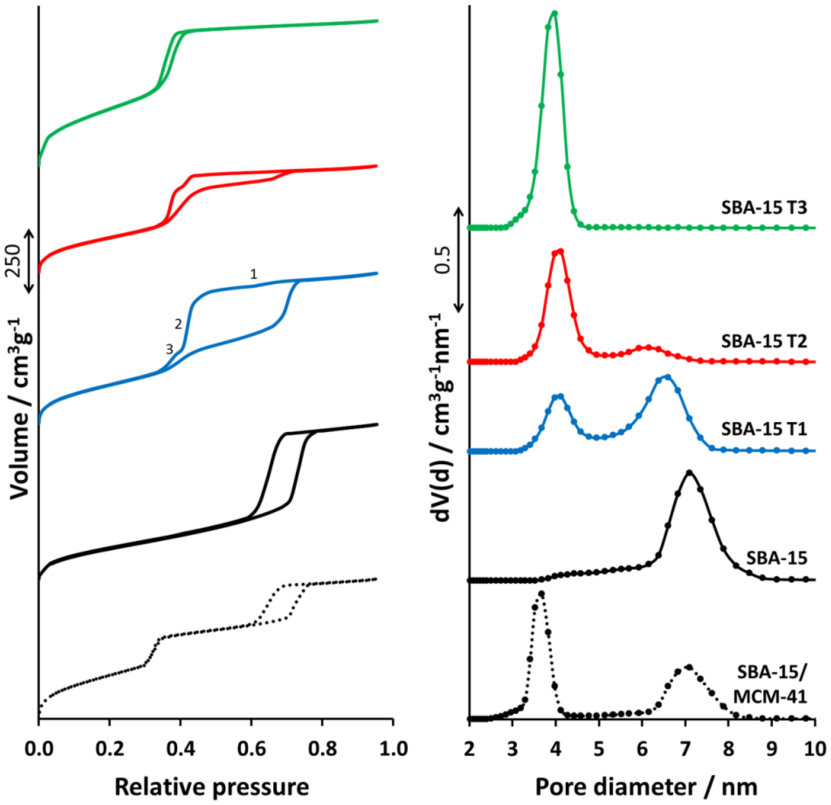

Figure 7.3 Argon sorption isotherms (left) and corresponding pore size distributions (right) of a mechanical mixture of SBA-15 and MCM-41, parent SBA-15, and the transformed materials SBA-15 with various degrees of transformation (T1 to T3). The isotherms and pore size distributions are offset for clarity.

The desorption isotherms of the partially transformed SBA-15 are complex and, in agreement with previously reported results from nitrogen sorption,[4] consist of three segments, as is best seen in the desorption isotherm of SBA-15 T1 (Figure 7.3). Starting from high relative pressure, the first step in the desorption isotherm corresponds to evaporation from unobstructed SBA-15 pores (step 1), followed by a step at $p/p_0 = 0.41$ (step 2) and a subsequent smaller step (step 3) leading to the closure of the hysteresis loop at $p/p_0 = 0.36$. If we assume a structure where the large pores (6.6 nm) are interconnected with the small pores (4.0 nm), steps 2 and 3 can be assigned to cavitation followed by evaporation of argon from the small pores (or necks). Cavitation implies the spontaneous nucleation and growth of gas bubbles in the metastable condensed fluid present in the large pores (or cavities), while the fluid in the small pores (or necks) remains in a stable state. For argon at 87.3 K in cylindrical pores, a critical neck size of approximately 5 nm has been proposed.[8] Below this critical neck size, desorption is generally assumed to occur by cavitation.[9] Due to the comparatively small neck size in SBA-15 T1, it is very likely that cavitation is the cause for the unusual desorption isotherms of the partially transformed materials. The type of evaporation mechanism can be determined by measuring the sorption isotherms with different adsorptives, e.g., nitrogen and argon.[10] If evaporation occurs by cavitation, the relative pressure of evaporation does not correlate with the neck size. The pore size distribution calculated from the desorption isotherm should therefore yield different pore size values for nitrogen and argon. If the pore size distributions calculated from these desorption isotherms are similar, evaporation follows a pore blocking mechanism and the neck size can be directly determined from the desorption isotherm.

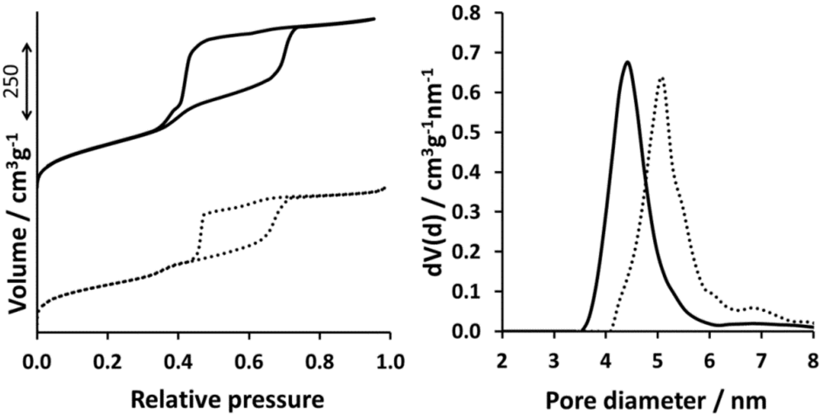

Figure 7.4 Argon sorption (87.3 K, solid) and nitrogen sorption (77 K, dashed) isotherms of SBA-15 T1. The pore size distributions calculated from the respective desorption isotherms are shown on the right.

Figure 7.4 compares the argon and nitrogen sorption isotherms of SBA-15 T1 and the pore size distributions calculated from the respective desorption isotherm, yielding an “artificial” average pore size of 4.4 nm (argon) and 5.1 nm (nitrogen). Calculations of the pore sizes based on the adsorption isotherms yield identical results independent of whether argon or nitrogen is used as an adsorptive. This confirms that step 2 in the desorption isotherm of SBA-15 T1 is caused by cavitation. The adsorption and desorption isotherms of SBA-15 T2 feature the same steps as observed for SBA-15 T1, with the major adsorption/desorption processes now being associated with the small pores. SBA-15 T3 shows a type IV(a) isotherm,[5] which leads us to the conclusion that regarding the pore size of the material, transformation to a pore system with a smaller pore size is complete. A comparison of the argon sorption isotherms of the transformed materials with the isotherms of a mechanical mixture of SBA-15 and MCM-41 supports the assumption of interconnected large mesopore and small mesopore domains in the case of the partially transformed samples, although we cannot exclude that some of the small pores in the partially transformed samples SBA-15 T1 and SBA-15 T2 are present as isolated domains that are not interconnected with the large pore domains. It is interesting to note that the pore size of the original SBA-15 domain decreases with increasing degree of transformation until it disappears from the pore size distribution at a high degree of transformation (SBA-15 T3).

7.1.2 Small angle X-ray scattering

SAXS provides additional information on the newly introduced pore structures. The SAXS patterns of the parent and transformed SBA-15 samples are shown in Figure 7.5. The repeat distances a_0 of the small and large mesopore domains are given in Table 7.1. All samples feature the typical (100), (110), and (200) peaks, representative of the hexagonal space group *P6mm*.[3]

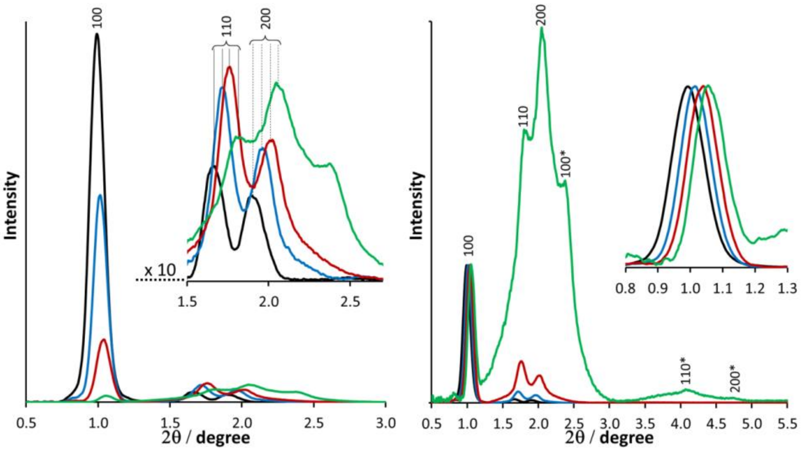

Figure 7.5 Left: SAXS patterns of parent SBA-15 (black), SBA-15 T1 (blue), SBA-15 T2 (red), and SBA-15 T3 (green). Right: SAXS patterns of the same samples normalized to the (100) peak. The inset shows the shift of the (100) peak with increasing degree of transformation.

With increasing degree of transformation, the intensity of the (100) peak decreases. This can be attributed to a degradation of the mesoscopic pore ordering of the parent SBA-15. Small pore domains form close to the external particle surface, whereas the pore diameter of the parent SBA-15 domains is slightly reduced. Normalizing the patterns to the (100) peak of the SBA-15 domains reveals the development of the small pore domains (Figure 7.5, right). While these newly formed domains are not clearly distinguishable in the SAXS patterns of SBA-15 T1 and SBA-15 T2, sample SBA-15 T3 shows a pattern that can be assigned to two different phases, namely the hexagonal SBA-15 phase ((100), (110), and (200)) and a newly formed hexagonal phase ((100*), (110*), and (200*)) with shorter repeat distance a_0. This new hexagonal phase is related to a classical MCM-41 type pore structure. A comparison of the SBA-15 T3 pattern with the pattern of a mechanical mixture of SBA-15 and MCM-41 illustrates the matching peaks (Figure 7.6).

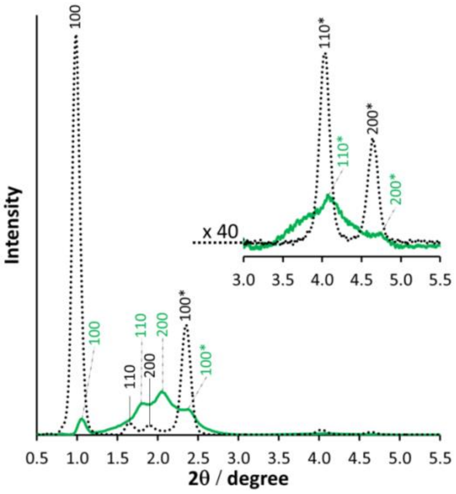

Figure 7.6 SAXS patterns of a mechanical mixture of SBA-15 and MCM-41 (dotted line) and SBA-15 T3 (green line).

Based on the analysis of the argon sorption isotherms, we initially assumed that the sample SBA-15 T3 was fully transformed, as the respective pore size distribution no longer showed contributions of the parent SBA-15 (Figure 7.3). However, the SAXS pattern of SBA-15 T3 still provides evidence for the presence of a structure with a SBA-15 type pore spacing (Figure 7.6). Taking the pore size distribution into consideration, we can conclude that some of the original SBA-15 pores (7.1 nm) have been transformed into smaller pores (4.0 nm) while retaining their original pore spacing. From these results and previous studies on the accessibility of the large pore domains in partially transformed SBA-15 samples,[4] the pseudomorphic transformation of SBA-15 can be described by a process that replaces the SBA-15 pore system close to the external particle surface with MCM-41 type domains, leading to the formation of bottlenecks. A higher degree of transformation can be achieved by decreasing the silica/NaOH ratio. This not only promotes the formation of the small pore domains, but also reduces the pore size of the SBA-15 domains while retaining the original pore spacing. A schematic representation of the transformed pore structures is given in Figure 7.7.

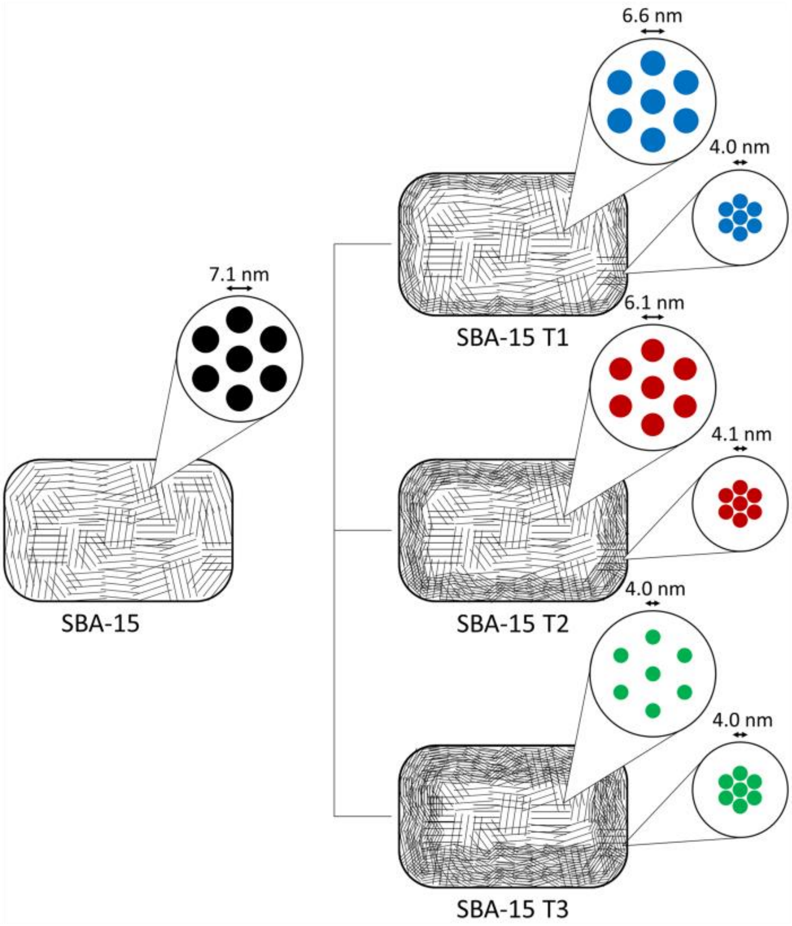

Figure 7.7 Schematic representation of the pore structure domains obtained after various degrees of transformation.

The pore wall thickness of an ordered mesoporous material can be obtained by subtracting the pore diameter from the repeat distance. Application of this concept to SBA-15 T3 yields a pore wall thickness of 0.3 nm, which is substantially smaller than values obtained for typical MCM-41 materials.[11] However, it should be kept in mind that the small repeat distance is calculated from the SAXS peaks of the MCM-41 type domains, whereas the pore size distribution contains an additional contribution from the domains with SBA-15 type pore spacing, which could feature a slightly larger pore size.

7.2 Transformation of SBA-16

The structure of SBA-16 is characterized by a three-dimensional network of cage-like pores, which are arranged in a body-centered-cubic array and connected through small mesopores.[12,13]

7.2.1 Argon sorption measurements

The argon sorption isotherm of SBA-16 (Figure 7.8) features a large hysteresis loop, typical for materials with ink-bottle pores.[10] The desorption branch of the hysteresis loop is steeper than the adsorption branch, leading essentially to a H2(a) hysteresis.[5] Close inspection of the desorption isotherm reveals two segments, with the lower pressure segment being steeper, thus indicating a forced closure of the hysteresis loop. This forced closure occurs at a relative pressure of $p/p_0 = 0.40$ and thus at a higher relative pressure than the lower closure point observed in the case of cylindrical pores ($p/p_0 = 0.36$). This is in agreement with previous reports on adsorption hysteresis in ink-bottle type pores, where it was found that the pressure of cavitation in spherical pores is slightly higher than the lower closure point of the hysteresis loop in materials with cylindrical pores.[8]

The pore size distribution of SBA-16 shows a narrow peak at 6.2 nm and a broad contribution extending from 1.8 to 5.3 nm. The latter can be attributed to the non-uniformity of the micro- and mesopores that are often observed in materials prepared with $EO_xPO_yEO_x$ block copolymer templates.[13] After partial pseudomorphic transformation (SBA-16 T1) a H2(b) hysteresis is observed. The H2(b) loop is typically associated with pore blocking and a wide distribution of neck sizes.[5] Contrary to the desorption isotherm of the parent SBA-16, the desorption isotherm of SBA-16 T1 decreases gradually with a slight step (3*, Figure 7.8) before closing at $p/p_0 = 0.40$. Transformation apparently leads to an enlargement of the pore necks and a broadening of the neck size distribution. The pore size distribution of SBA-16 T1 confirms the elimination of pores with a diameter below 3.8 nm. At a higher transformation degree (SBA-16 T2), two adsorption steps can be distinguished. These steps correspond to the two steps observed in the adsorption isotherm of the SBA-16/MCM-41 mixture (steps 1 and 2, Figure 7.8), indicating the partial transformation of the SBA-16 pore structure and the introduction of small pore domains. The respective pore size distribution shows maxima at 3.8 and 5.5 nm.

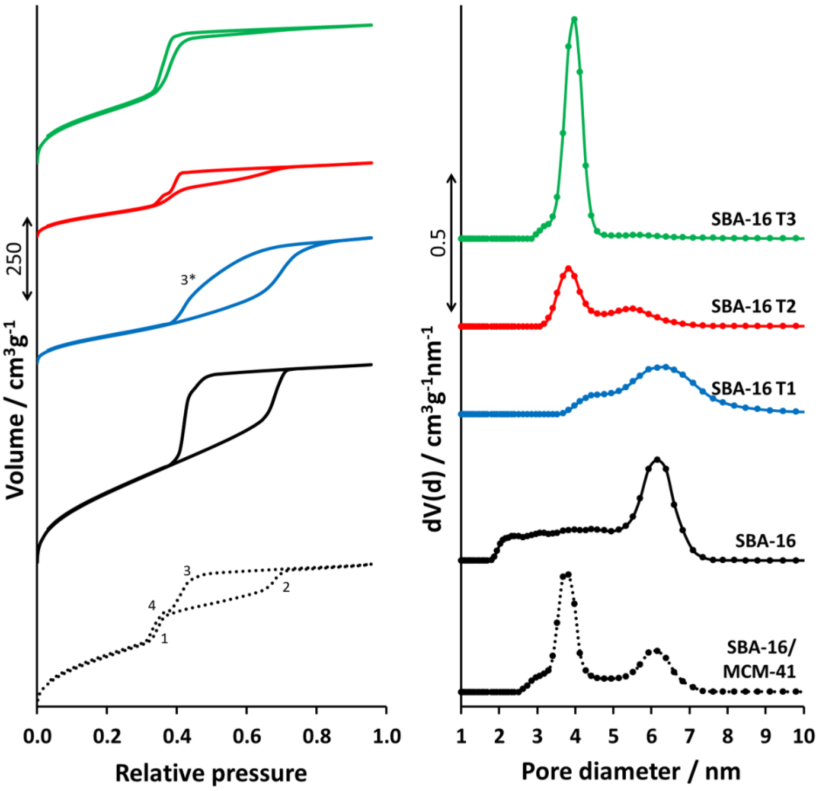

Figure 7.8 Argon sorption isotherms (left) and corresponding pore size distributions (right) of a mechanical mixture of SBA-16 and MCM-41, parent SBA-16, and the transformed materials SBA-16 with various degrees of transformation (T1 to T3). The isotherms and pore size distributions are offset for clarity.

The desorption isotherm of SBA-16 T2 features a step at $p/p_0 = 0.38$, which we assign to cavitation. Note that compared to the parent SBA-16 the cavitation step has shifted to lower relative pressure. A possible interpretation is the transformation of the original pore structure with spherical cavities into a structure with pores approaching a cylindrical shape. The pore size distribution and isotherms of SBA-16 T3 contain only minor contributions of the parent pore size and thus point to an almost complete transformation. The question remains whether the newly introduced pore structure corresponds to an actual MCM-41 type phase with a hexagonal pore arrangement.

7.2.2 Small angle X-ray scattering

SAXS patterns of the samples are shown in Figure 7.9. Similar to the transformation of SBA-15, a decrease of the main peak (110) is observed upon increasing the degree of transformation, accompanied by a slight shift to larger angles.

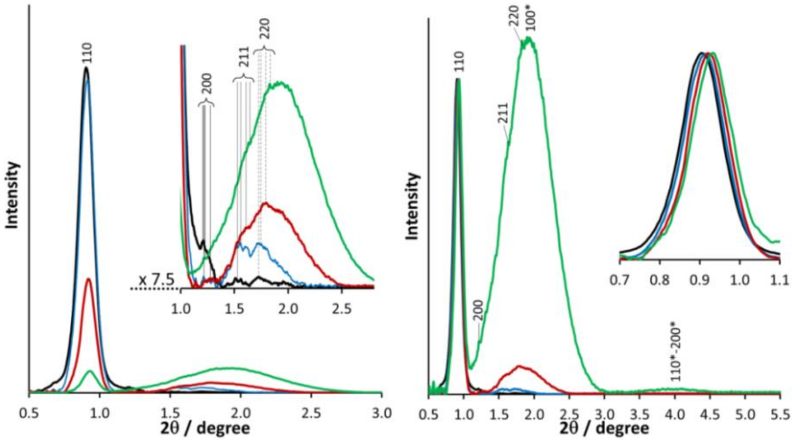

Figure 7.9 Left: SAXS patterns of parent SBA-16 (black), SBA-16 T1 (blue), SBA-16 T2 (red), and SBA-16 T3 (green). Right: SAXS patterns of the same samples normalized to the (110) peak. The inset shows the shift of the (110) peak with increasing degree of transformation.

Interestingly, an increasing intensity is observed in the 2θ range between 1.2 and 3.0°, suggesting the formation of a new framework. Comparison with the SAXS pattern of a mechanical mixture of SBA-16 and MCM-41 (Figure 7.10) points to the presence of a hexagonal phase ((100*), (110*), (200*)) and of a cubic phase ((110), (200), (211), (220)).

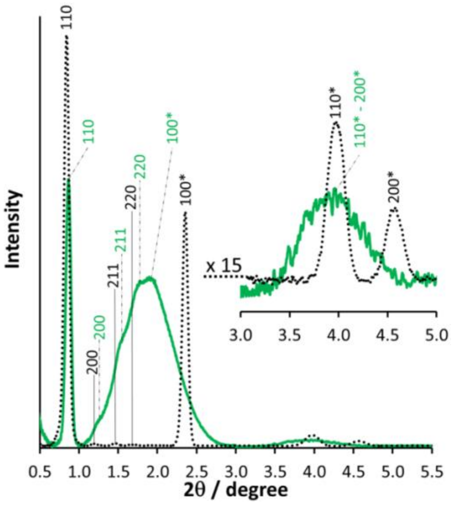

Figure 7.10 SAXS patterns of a mechanical mixture of SBA-16 and MCM-41 (dotted line) and SBA-16 T3 (green line).

Comparing the SAXS pattern of a mechanical mixture of SBA-16 and MCM-41 with the pattern of SBA-16 T3 provides evidence for the conservation of the cubic structure (Figure 7.10), despite the observation that the pore size distribution of SBA-16 T3 (Figure 7.8) shows only a minor contribution of the parent pore size. Similar results were obtained when decreasing the silica/NaOH ratio to 7. The pore structure of the transformed SBA-16 can thus be described by means of a hybrid structure consisting of domains with one-dimensional pores and domains with a three-dimensional pore system originating from the parent SBA-16, but with reduced pore size. It is likely that the cavities of SBA-16 have been transformed into a cubic network of cylindrical channels. The SAXS peaks that can be assigned to the hexagonal domains formed upon transformation are comparatively broad and therefore indicative of poor long-range ordering. A schematic representation of the transformed pore structures is given in Figure 7.11.

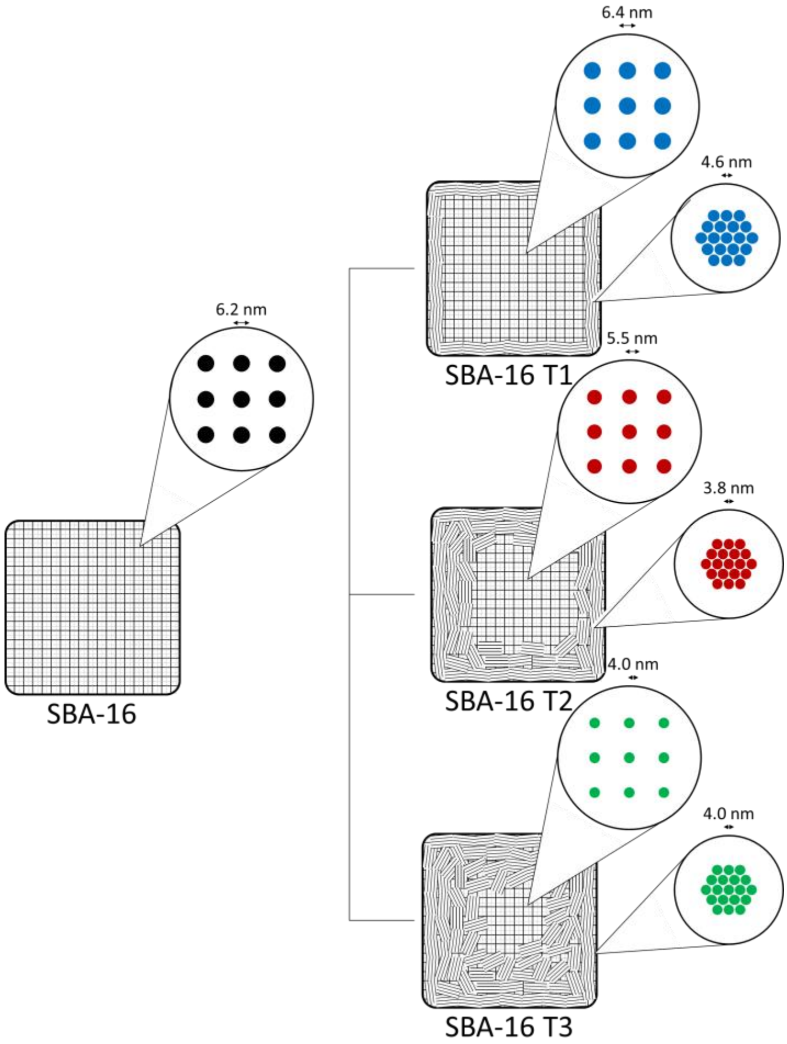

Figure 7.11 Schematic representation of the pore structure domains obtained after various degrees of transformation.

7.3 Conclusion

The pseudomorphic transformation of ordered mesoporous silica yields materials with hybrid pore structures. The analysis of the transformed samples by SAXS shows that structural features of the starting material are retained upon transformation, even at high transformation degree where a seemingly complete conversion of large to small pores is obtained. The pore structure of the starting material therefore determines to a certain extent the pore structure of the transformed material. The characteristically large pore spacing of SBA-15 is still found in the transformed material, although the pore size has been significantly reduced. Similarly, a cubic phase is observed in the SAXS patterns of materials obtained by pseudomorphic transformation of SBA-16. Pseudomorphic transformation can be used on any porous silica, as long as an efficient uptake of the SDA is possible. We have shown that even in the case of SBA-16 with its relatively narrow pore necks, the pores can be filled with hexadecyltrimethylammonium ions. Due to the particle shape being unaltered after transformation, the pathway of pseudomorphic transformation implies less compromise between pore structure and particle shape, in particular when compared to classical mesoporous silica syntheses. The ability to design complex pore structures, such as cylindrical pores with bottlenecks, is essential for advancing the understanding of gas sorption isotherms. Adsorption-desorption hysteresis can provide valuable information on pore connectivity, bottlenecks, and cavities. The well-defined structural features of a pseudomorphically transformed material are an ideal basis for studying evaporation mechanisms such as cavitation and pore blocking.

7.4 Experimental

7.4.1 Materials

Pluronic P123, Pluronic F127, tetraethyl orthosilicate (TEOS, ≥ 99 %), sodium hydroxide (97 %), aqueous ammonia (25 %), and hydrochloric acid (32 %) were obtained from Sigma-Aldrich. Pluronic P123 and F127 are triblock poly(ethylene oxide)–poly(propylene oxide)-poly(ethylene oxide) ($EO_xPO_yEO_x$) copolymers, with $x = 20$ and $y = 70$ for P123, and $x = 106$ and $y = 70$ for F127. Hexadecyltrimethylammonium bromide (CTAB, 99+ %) was obtained from Acros. All chemicals were used as received. Previously published procedures were followed to prepare the parent materials SBA-15,[14] MCM-41,[15] and SBA-16.[16] Details on the syntheses are given below.

7.4.2 Synthesis of SBA-15

An amount of 2.2 g of P123 was dissolved in 80 mL of 1.55 M hydrochloric acid. Once a clear solution was obtained, 5 mL of TEOS was slowly added. The mixture was stirred for 20 h at 35°C, transferred to a Teflon-lined autoclave, and placed in a preheated oven at 100 °C for 24 h. The autoclave was allowed to cool to room temperature before the product was recovered by filtration and washing with at least 1 L of H_2O. The material was allowed to dry at room temperature overnight and then calcined in air at 550 °C for 12 h. A heating rate of 2 °C min^{-1} was applied.

7.4.3 Synthesis of MCM-41

An amount of 2.2 g of CTAB was dissolved in a solution of 52 mL of H_2O and 25 mL of aqueous ammonia (25 %). After dropwise addition of 10 mL of TEOS, the mixture was stirred at room temperature for 3 h. It was then transferred to a Teflon-lined autoclave and put in an oven at 110 °C for 48 h. The autoclave was allowed to cool to room temperature before the product was recovered by filtration and washing with at least 250 mL of H_2O. The material was allowed to dry at room temperature overnight. The SDA was removed by heating at 300 °C for 2 h and subsequent calcination at 550 °C for 12 h. A heating rate of 2 °C min^{-1} was applied.

7.4.4 Synthesis of SBA-16

An amount of 0.47 g of F127 and 55 mg of CTAB was dissolved in 65 mL of 0.4 M hydrochloric acid. Once a clear solution was obtained, 1.66 mL of TEOS was added under strong stirring. The mixture was stirred for 30 minutes at room temperature, transferred to a Teflon-lined autoclave, and placed in a preheated oven at 95 °C for 120 h. The autoclave was allowed to cool to room temperature before the product was recovered by filtration and washing with 5 mL of H_2O. The material was allowed to dry at room temperature overnight and then calcined in air at 550 °C for 12 h. A heating rate of 2 °C min^{-1} was applied.

7.4.5 Pseudomorphic transformation

An amount of 300 mg of the parent silica (SBA-15 or SBA-16) was mixed with 182 mg of CTAB and a varying amount of NaOH. The ratio of the mass of silica (m_{silica}) and NaOH (m_{NaOH}) for each synthesis is given in Table 1 (SBA-15) and Table 2 (SBA-16). To this mixture, 2 mL of H_2O was added and stirred for 30 min in a Teflon liner, which was then placed in an autoclave (100 mL volume) and heated in an oven at 100 °C for 6 h. After allowing the autoclave to cool to room temperature, the product was filtered, washed with 250 mL of H_2O, and calcined in air at 550 °C for 12 h. A heating rate of 2 °C min^{-1} was applied.

7.4.6 Physical measurements

Argon sorption isotherms (54 measurement points for adsorption, 40 points for desorption) were measured at 87.3 K with a Quantachrome Autosorb iQ MP equipped with a CryoCooler. Pore size distributions and average pore diameters d_{DFT} were determined from the adsorption isotherms by a non-local density functional theory (NLDFT) model developed for silica exhibiting cylindrical pore geometry (Software ASiQwin v3.01, Quantachrome Instruments).[17] For the parent SBA-16, a kernel for spherical cavities was used. Total pore volumes V_{tot} were derived from the amount of adsorbed argon at a relative pressure of $p/p_0 = 0.95$. Scanning electron microscopy (SEM) images were collected with a FEI Quanta FEG 250. SAXS patterns were recorded on a Bruker NanoStar in transmission mode with $CuK\alpha_1$ radiation.

7.5 References

1. X. Li, D. Wu, J. Wang, W. Zhu, Y. Luo, C. Han and W. Ma, S. He, Microporous Mesoporous Mater., 2016, 226, 309-315.

2. W. C. Yoo and A. Stein, Chem. Mater., 2011, 23, 1761-1767.
3. M. J. Reber and D. Brühwiler, Part. Part. Syst. Charact., 2015, 32, 243-250.
4. M. J. Reber and D. Brühwiler, Dalton Trans., 2015, 44, 17960-17967.
5. M. Thommes, K. Kaneko, A. V. Neimark, J. P. Olivier, F. Rodriguez-Reinoso, J. Rouquerol and K. W. Sing, Pure Appl. Chem., 2015, 87, 1051-1069.
6. R. Ryoo, C. H. Ko, M. Kruk, V. Antochshuk and M. Jaroniec, J. Phys. Chem. B, 2000, 104, 11465-11471.
7. A. Galarneau, H. Cambon, F. Di Renzo, R. Ryoo, M. Choi and F. Fajula, New J. Chem., 2003, 27, 73-79.
8. P. I. Ravikovitch and A. V. Neimark, Langmuir, 2002, 18, 9830-9837.
9. C. J. Rasmussen, A. Vishnyakov, M. Thommes, B. M. Smarsly, F. Kleitz and A. V. Neimark, Langmuir, 2010, 26, 10147-10157.
10. M. Thommes, B. Smarsly, M. Groenewolt, P. I. Ravikovitch and A. V. Neimark, Langmuir, 2006, 22, 756-764.
11. M. Kruk, M. Jaroniec, Y. Sakamoto, O. Terasaki, R. Ryoo and C. H. Ko, J. Phys. Chem. B, 2000, 104, 292-301.
12. Y. Sakamoto, M. Kaneda, O. Terasaki, D. Y. Zhao, J. M. Kim, G. Stucky, H. J. Shin and R. Ryoo, Nature, 2000, 408, 449-453.
13. K. Miyasaka, H. Hano, Y. Kubota, Y. Lin, R. Ryoo, M. Takata, S. Kitagawa, A. V. Neimark and O. Terasaki, Chem. Eur. J., 2012, 18, 10300-10311.
14. D. Zhao, Q. Huo, J. Feng, B. F. Chmelka and G. D. Stucky, J. Am. Chem. Soc., 1998, 120, 6024-6036.
15. D. Brühwiler and H. Frei, J. Phys. Chem. B, 2003, 107, 8547-8556.
16. M. Mesa, L. Sierra, J. Patarin and J.-L. Guth, Solid State Sci., 2005, 7, 990-997.
17. J. Landers, G. Y. Gor and A. V. Neimark, Colloids Surf. A, 2013, 437, 3-32.

8. OUTLOOK

New versatile and efficient technologies can be developed using mesoporous materials. Porous silica particles can be considered as a fundamental support for applications in catalysis, sensors, drug delivery, environmental remediation, etc. The convenient surface functionalization combined with the possibility to trigger specific reactions with external stimuli is an essential feature of these materials. Light is a common stimulus and the possibility to focus it in a small fiber opens intriguing prospects. The incorporation of functionalized nanoporous silicates with well-defined pore systems into the cladding of an optical fiber is the basis for the development of a nanoporous hybrid optical fiber platform. Figure 8.1 shows three application examples: drug release (light in, drugs out), optical sensing of NH_3 (analyte in, light out), and light-harvesting (light in, concentrated light out).

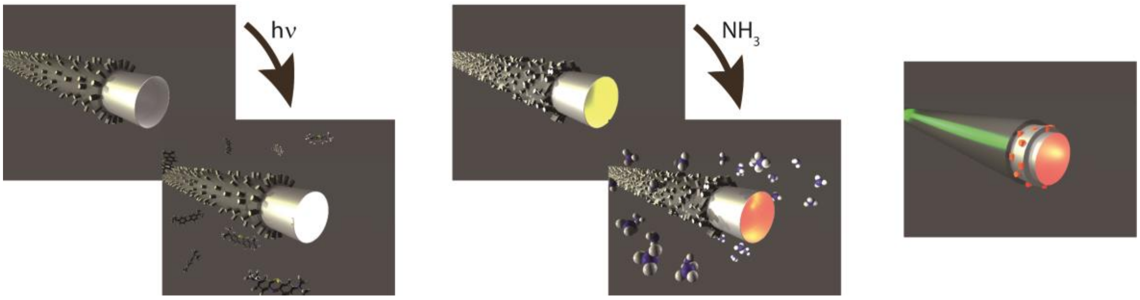

Figure 8.1. Illustration of the nanoporous hybrid optical fiber platform and its applications as drug release system, optical sensor for ammonia and light-harvesting device.

The customization of mesoporous silica particles discussed in this thesis plays a key role in the implementation of these ideas. The aspect ratio and the selective functionalization of ASNCs are important factors for the particle grafting in order to maximize the accessibility to the pore volume.

8.1 Drug delivery

Vertical alignment of ASNCs is required for drug delivery. The particular channel disposition (perpendicular to the substrate) and the surface functionalization favor the drug release mediated by a light stimulus. The strategies for the controlled delivery are illustrated in Figure 8.2.

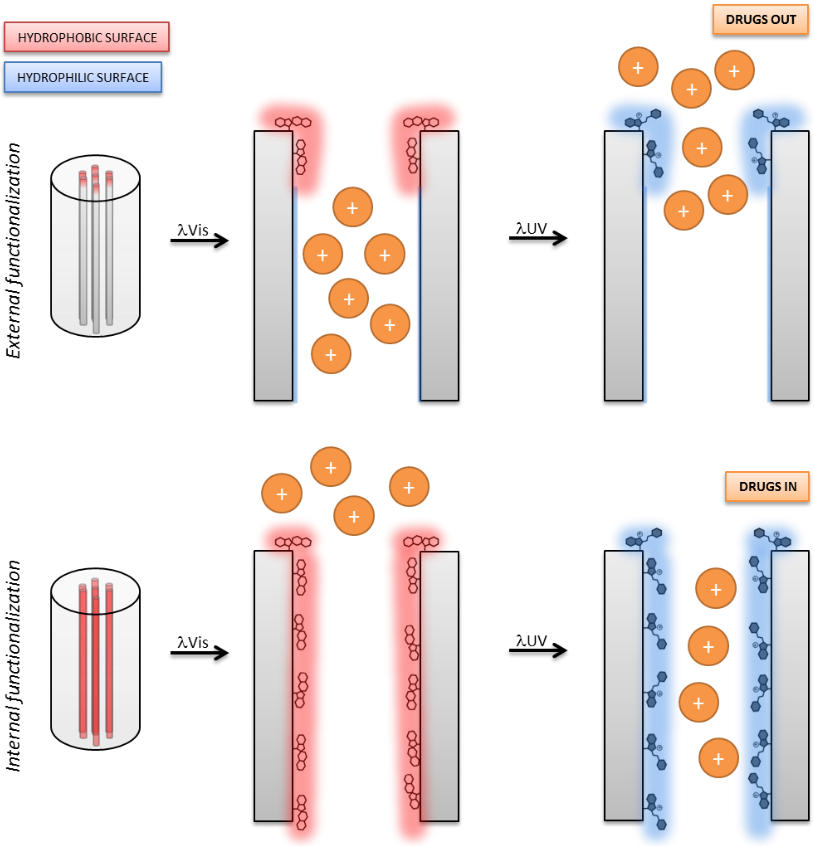

Figure 8.2. Drug release strategies. Top: the release is triggered by UV-light. Bottom: the uptake is activated by UV-light.

Specific molecules, such as spiropyrans, change their polarity upon irradiation with UV light. With ASNCs it is possible to create gates located selectively at the pore entrances (Figure 8.2, top) or functionalize the pore surface (Figure 8.2, bottom) to obtain various mechanisms for triggering the release.

8.2 Optical sensing

The detection of specific chemicals, such as ammonia, is generally performed by monitoring changes in absorption or fluorescence. The large surface area of ASNCs and the homogeneous distribution of functional moieties can lead to sensors with light sensitivity. An optical sensing platform is achievable by combining functionalized mesoporous silica with optical fibers. In collaboration with EMPA, our group has conducted experiments with optical gas sensors based on FRET dye pairs in a modified silicate coating (Figure 8.3). The active dye species are covalently grafted to the pore surface of the mesoporous silicate to overcome the problem of leaching. The advantage of using a FRET sensor is that with a single excitation wavelength, dual or multiple emissions are obtained. This provides flexibility in terms of optical sensor design.

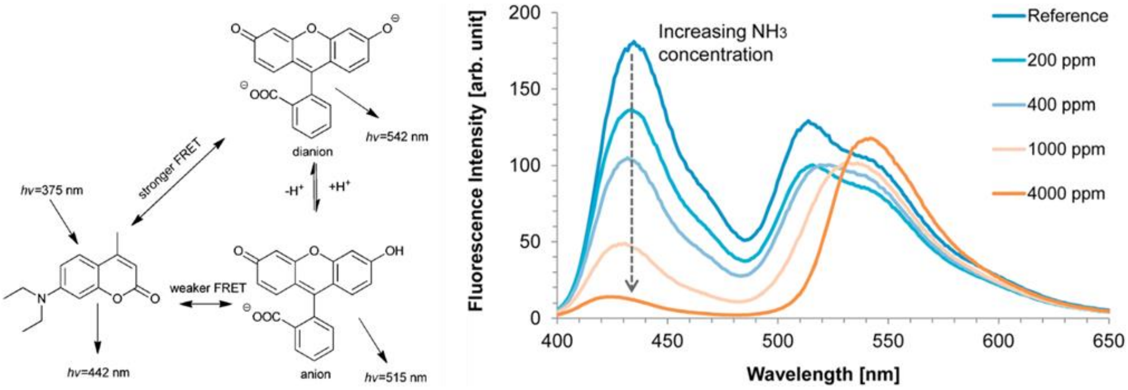

Figure 8.3 FRET between fluorescein and coumarin (left) and fluorescence spectra observed in a coumarin-fluorescein xerogel (right).[1]

8.3 Light harvesting

An alternative method for generating electricity from sunlight involves the use of an artificial harvesting system in combination with suitable solar cells. The idea is to build a luminescent solar concentrator (LSC) to concentrate and direct part of the solar spectrum onto efficient photovoltaic cells using a polymer-based waveguide (Figure 8.4).

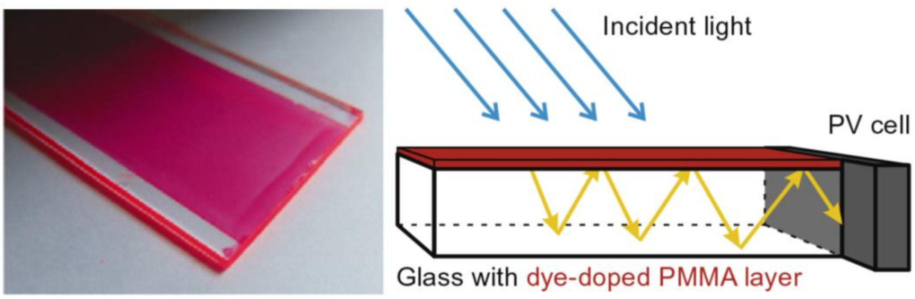

Figure 8.4 Photographic image and schematic representation of a LSC based on a thin dye-doped polymer film. Re-emitted light is guided toward the edges by total internal reflection (yellow arrows).[2]

The use of light-harvesting host-guest materials in LSCs is particularly attractive to prevent the main problems of this technology: self-absorption and long-term stability. Mesoporous silica is a versatile host material for the supramolecular organization of a large variety of guests. The inclusion of light-absorbing species and their arrangement in the channels can be used to achieve an efficient energy transfer and enhanced stability. Applying the LSC technology on the optical fiber support is expected to provide a perfect system for the light transport. An application example based on a cylindrical rod is reported in Figure 8.5.

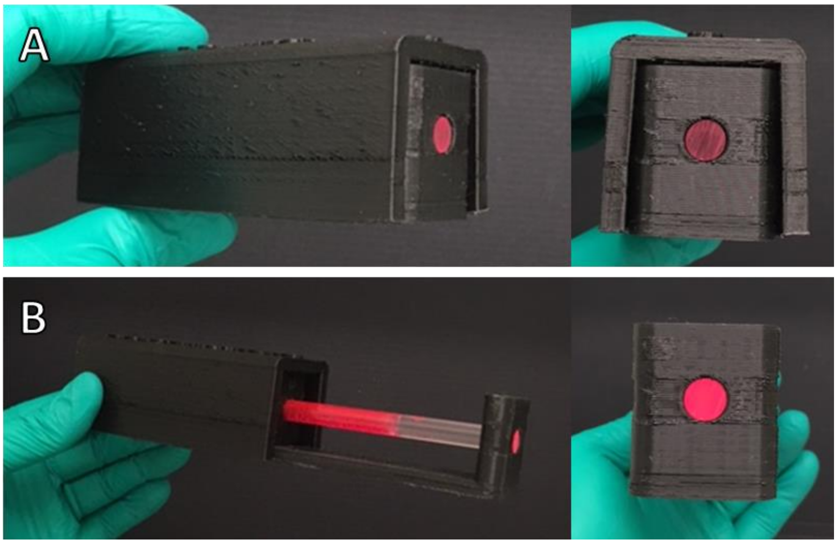

Figure 8.5 LSC technology applied on a PMMA rod (half coated). When the black box is closed, the circular rod face shows the darker color of the coated dye (panel A). When the black box is open, the rod is exposed to light and the circular rod face becomes brighter (panel B).

8.3 References

1. S. Widmer, M. J. Reber, P. Müller, C. E. Housecroft, E. C. Constable, R. M. Rossi, D. Brühwiler, L. J. Scherera and L. F. Boesel, Analyst, 2015,140, 5324-5334.
2. T. Dienel, C. Bauer, I. Dolamic and D. Brühwiler, Solar Energy, 2010, 84, 1366-1369.

9. CURRICULUM VITAE

PERSONAL DATA

First Name: Nicola

Surname: Zucchetto

Nationality: Italian

Date and place of birth: 15th December 1985, Brescia, Italy

Address: Salerstrasse 21, 8050 Zürich

Mobile: +41 789669135

E-mail: zucchetto.nicola@gmail.com

EDUCATION

Period: February 2014 - Ongoing

Institute: University of Zurich - Zurich University of Applied Sciences, Switzerland

Level classification: Ph.D. Studies in Chemistry

Ph.D. Thesis: *Customized Arrays of Silica Nanochannels*

Supervisor: PD Dr. Dominik Brühwiler

Period: December 2009 - October 2011

Institute: University of Parma, Italy

Level classification: Second Level Degree in Chemistry

Master Thesis: *Release and microbial inhibition of antibacterial coatings*

Supervisors: Prof. Angelo Montenero and Prof. Claudio Corradini

Period: October 2005 - December 2009

Institute: University of Parma, Italy

Level classification: First Level Degree in Chemical Sciences and Technology

Bachelor Thesis: *Cu(I) complexes with N_2S donor ligands and triphenylphosphine*

Supervisor: Dr. Luciano Marchiò

WORKING EXPERIENCE

Period: May 2012 - January 2014

Company: CIPACK (Interdepartmental Center for Packaging), University of Parma

Main activities and responsibilities: Research fellow in the group of Prof. Angelo Montenero. Marketing and company contact responsible, national and international company projects organizer and researcher on plastics and cellulosic materials for packaging applications.

Period: Nov.2011 - April 2012

Company: CO.RI.VE. (Glass Research Consortium), University of Parma and Bormioli Rocco S.P.A.

Main activities and responsibilities: Research assistant. Researcher on vitrification of hazardous waste from incinerator filters having possible applications as inert material.

Period: October 2004 - June 2005

Company: VALPRES, Brescia, Italy

Main activities and responsibilities: Worker. Responsible of the assembly, testing and performance quality of valves and actuators for domestic and industrial uses.

LIST OF PUBLICATIONS

- *Indigo in the nanochannels of zeolite L: Towards a new type of colorant*, P. Woodtli, P. Müller, S. Giger, L. Sägesser, M. J. Reber, N. Zucchetto, A. Ecker and D. Brühwiler, accepted.

- *The structure of mesoporous silica obtained by pseudomorphic transformation of SBA-15 and SBA-16*, N. Zucchetto, M. J. Reber, L. Pestalozzi, R. Schmid, A. Neels and D. Brühwiler, Microporous and Mesoporous Materials, 2017, in press.

- *Functionalization of arrays of silica nanochannels by post-condensation*, N.Zucchetto and D. Brühwiler, Dalton Transactions, 2016, 45, 14363-14369.

- *Tuning the aspect ratio of arrays of silica nanochannels*, N. Zucchetto and D. Brühwiler, RSC Advances, 2015, 5, 74638-74644.

- *Natamycin based sol-gel antimicrobial coatings on polylactic acid films for food packaging*, C. Lantano, N. Zucchetto, A. Montenero, C. Corradini, A. Lorenzi, I. Alfieri and A. Cavazza. Food Chemistry, 2014, 165, 342-347.

- *Antimicrobial films containing lysozyme for active packaging by sol-gel technique,* C. Lantano, N. Zucchetto, A. Montenero, C. Corradini, A. Lorenzi and I. Alfieri. Journal of Food Engineering, 2013, 119, 580-587.

CONFERENCE CONTRIBUTIONS

Oral presentations:

- *Functionalization of arrays of silica nanochannels by post-condensation*, N. Zucchetto and D. Brühwiler, IfC-B seminar, University of Zurich, December 2016.

- *Tuning the aspect ratio of arrays of silica nanochannels*, N. Zucchetto and D. Brühwiler, IfC-B seminar, University of Zurich, December 2015.

- *Active packaging: controlled release of antimicrobial coating*, N. Zucchetto and A. Montenero, Cellulosic materials and packaging: from research to new business applications, Bologna, June 2013.

- *Study, fabrication and characterization of coatings for innovative packaging,* N. Zucchetto and A. Montenero, XI National Congress AIMAT, Gaeta, 16-19 September 2012.

- *Research and antimicrobial materials for packaging applications*, N. Zucchetto and A. Montenero, 2nd NewGenPak, Project Workshop on Fundamentals of Composite Materials, Bologna, 19-22 February 2013.

- *Innovative Systems for Packaging*, N. Zucchetto and A. Montenero, Plastic and Food: the current legislation, a challenge for the industry?, Parma, June 2013.

Poster presentations:

- *Pseudomorphic transformation of mesoporous silica particles*, N. Zucchetto, M. J. Reber and D. Brühwiler, SCS fall meeting, Bern, August 2017.

- *The structure of mesoporous silica obtained by pseudomorphic transformation of SBA-15 and SBA-16*, N. Zucchetto, M. J. Reber and D. Brühwiler, 14th Doktorandentag, Zurich, June 2017.

- *Tailor-made arrays of silica nanochannels,* N. Zucchetto and D. Brühwiler, 5th International Conference on Multifunctional, Hybrid and Nanomaterials, Lisbon, March 2017.

- *Functionalization of arrays of silica nanochannels by post-condensation*, N. Zucchetto and D. Brühwiler, SCS fall meeting, Zurich, September 2016.

- *Customized mesoporous silica particles*, N. Zucchetto, M. J. Reber, J. Fahrni and D. Brühwiler, ISGS summer school, Berlin, July 2016.

- *Tuning the aspect ratio of the arrays of silica nanochannels*, N. Zucchetto and D. Brühwiler, SCS fall meeting, Lousanne, September 2015.

10. ACKNOWLEDGEMENTS

First, I would like to thank my supervisor Dominik Brühwiler. He gave me the possibility to start this fantastic experience and he was always available for helps, answers and suggestions. I was really lucky to have him as role model during these years.

Thanks to Prof. Dr. Greta Patzke not only for the availability to be the head of my promotion committee, but also for the opportunity to exploit the lab facilities in her group.

Thanks to Prof. Dr. David Tilley for his full support as a member of my promotion committee.

During these PhD years I met many interesting and awesome persons. In particular, my colleagues and friends at the ZHAW. A huge thank you to Mike for welcoming me (although at the beginning I could not understand a word), for his help and for the funny moments in the lab (and not only). Thanks also to Jonas, Lukas, Louis and Sam for being great colleagues and friends. Finally, I am really grateful to all the professors and collaborators at ZHAW (special mention to Gabriele and Tobi) and to all my bachelor students (Michael, Patrick, Armin, Lias, Marco, Olivier and Jeoffrey).

I would like to thank the Patzke group at the University of Zurich (Fabio and Michael) for helping me with the XRD analyses.

Thanks to the CMSZH Graduate School for the financial support, the retreats, the BBQ and the interesting courses.

For the financial support I am grateful to the Swiss National Science Foundation (Projects 200021_149715 and 200021_172805).

I would like to thank all the Italian friends that I met here in Zurich for enjoying so many unforgettable moments and experiences together.

Grazie a tutti i miei amici che mi hanno sempre supportato (e sopportato) durante questi anni. In particolare il mio testimone Gio (rosso).

Grazie infinite anche ai miei genitori, i miei fratelli e a tutta la mia famiglia per esserci sempre. Un pensiero speciale ai miei nonni.

Grazie a mia moglie Anastasia per avermi aiutato a portare a compimento questa avventura e per accompagnarmi sempre nella realizzazione dei miei sogni.

P.S. Thanks to everybody who I may have forgotten (very probable).

Zürcher Hochschule
für Angewandte Wissenschaften

zh
aw

**Life Sciences und
Facility Management**

ICBT Institut für
Chemie und Biotechnologie

**Universität
Zürich**^UZH

CMSZH
CHEMICAL MOLECULAR SCIENCES ZURICH
GRADUATE SCHOOL